

Dekanat der Fakultät für Maschinenwesen und Betriebswissenschaften

DISSERTATION

Vertiefte Studie der Mikroströmung in tribologischen Systemen mit porösen Kontakten am Beispiel selbstschmierender Gleitlager

ausgeführt zum Zwecke der Erlangung des akademischen Grades einer
DoktorIn der technischen Wissenschaften
eingereicht an der TU Wien, Fakultät für Maschinenwesen und Betriebswissenschaften von

Ioana-Adina NEACȘU

Matrikelnummer: 1026262

Scheugasse 6/13+14, 1100 Wien

unter der Anleitung von

Priv.-Doz. Dipl.-Ing. Dr.techn. Bernhard Scheichl

E322 - Institut für Strömungsmechanik und Wärmeübertragung

begutachtet von

em. Univ.-Prof. Dipl.-Ing. Dr.techn. Alfred Kluwick

E322 - Institut für Strömungsmechanik und Wärmeübertragung, TU Wien

BA-Hochhaus, Getreidemarkt 9, 1060 Wien

Prof. Pwt Evans, BSc, PhD, DSc, CEng, FIMechE

Tribology and Contact Mechanics Group

Cardiff School of Engineering, Cardiff University, Cardiff, CF24 3AA

Diese Arbeit wurde von der Europäischen Kommission im Rahmen des MINILUBES-Projekt (FP7 Marie Curie ITN Netzwerk 216011-2) sowie von der "Österreichischen Forschungsförderungsgesellschaft" (FFG) im Rahmen des COMET K2 (Stipendium Nr. 824187 und 849109) unterstützt. Sie wurde beim "Österreichischen Exzellenzzentrum für Tribologie" durchgeführt.

Ich nehme zur Kenntnis, dass ich zur Drucklegung meiner Arbeit unter der Bezeichnung

Dissertation

nur mit Bewilligung der Prüfungskommission berechtigt bin.

Eidesstattliche Erklärung

Ich erkläre an Eides statt, dass die vorliegende Arbeit nach den anerkannten Grundsätzen für wissenschaftliche Abhandlungen von mir selbstständig erstellt wurde. Alle verwendeten Hilfsmittel, insbesondere die zugrunde gelegte Literatur, sind in dieser Arbeit genannt und aufgelistet. Die aus den Quellen wörtlich entnommenen Stellen, sind als solche kenntlich gemacht. Das Thema dieser Arbeit wurde von mir bisher weder im In- noch Ausland einer Beurteilerin/einem Beurteiler zur Begutachtung in irgendeiner Form als Prüfungsarbeit vorgelegt. Diese Arbeit stimmt mit der von den Begutachterinnen/Begutachtern beurteilten Arbeit überein.

Wien,

Unterschrift



TECHNISCHE
UNIVERSITÄT
WIEN
Vienna University of Technology



FAKULTÄT FÜR MASCHINENWESEN
UND BETRIEBSWISSENSCHAFTEN
DER TECHNISCHEN UNIVERSITÄT WIEN

Dekanat der Fakultät für Maschinenwesen und Betriebswissenschaften

DISSERTATION

Advanced description of the micro-flow in tribo-systems involving porous media on the example of self-lubricated bearings

carried out for the purpose of obtaining the degree of
Doctor technicae (Dr. techn.), submitted at TU Wien,
Faculty of Mechanical and Industrial Engineering, by

Ioana–Adina NEACȘU

Matriculation number: 1026262
Scheugasse 6/13+14, 1100 Vienna

under the supervision of

Priv.-Doz. Dipl.-Ing. Dr.techn. Bernhard Scheichl

E322 - Institute of Fluid Mechanics and Heat Transfer

reviewed by

em. Univ.-Prof. Dipl.-Ing. Dr.techn. Alfred Kluwick

E322 - Institute of Fluid Mechanics and Heat Transfer, TU Wien

BA-Hochhaus, Getreidemarkt 9, 1060 Vienna

Prof. Pwt Evans, BSc, PhD, DSc, CEng, FIMechE

Tribology and Contact Mechanics Group

Cardiff School of Engineering, Cardiff University, Cardiff, CF24 3AA

This work was supported by European Commission within the MINILUBES project (FP7 Marie Curie ITN network 216011-2) and by the "Austrian Research Promotion Agency" (FFG) within the framework of the COMET K2 (Grant no. 824187 and no. 849109) and it was carried out at the "Excellence Center for Tribology".

I confirm, that going to press of this thesis needs the confirmation of the examination committee.

Affidavit

I declare in lieu of oath, that I wrote this thesis and performed the associated research myself, using only literature cited in this volume. If text passages from sources are used literally, they are marked as such. I confirm that this work is original and has not been submitted elsewhere for any examination, nor is it currently under consideration for a thesis elsewhere.

Vienna,

Signature

Kurzfassung

In dieser Arbeit wird ein neuartiger und vollständiger Ansatz präsentiert, der unter anderem, die Beschreibung von Kavitation in hydrodynamisch laufenden Sintergleitlagern ermöglicht. Das massenerhaltende Modell koppelt die Reynoldsgleichung für den Schmierfilm mit dem Gesetz von Darcy für den Materialtransport durch den porösen Werkstoff. Das resultierende Gleichungssystem wird mittels finiter Differenzen diskretisiert und unter Ausnutzung einer künstlichen Druck-Dichte Beziehung iterativ gelöst.

Weiters wird eine umfangreiche numerische Analyse durchgeführt, in der die Hauptparameter über einen großen Wertebereich variiert werden. Es wird beobachtet, dass die Fluidsättigung im Punkt der Neubildung des Schmierfilms eine Diskontinuität aufweist, die unabhängig von der Normallast auftritt. Um die Anwendbarkeitsgrenzen des Ansatzes auszuloten, werden auch Extremfälle von sehr niedrigen und hohen Lagerlasten sowie kurzen/langen und hochporösen/(beinahe) massiven Lagern untersucht. Konvergierte Lösungen ergeben sich für relative Exzentrizitäten von bis zu 0,9, wobei um diesen Wert interessanterweise für den Fall eines sehr permeablen Lagersitzes die Reibzahl ansteigt, entgegen der sonstigen Tendenz zu deren Abnahme. Schließlich werden die aus den Simulationen erhaltenen Ergebnisse mit experimentellen Messungen an industriell gefertigten Lagern verglichen.

Dazu war die Implementierung eines präzisen Interpolationsschemas notwendig, mit dem aus der im Realsystem aufgebrachten Last schon im Vorhinein die relative Exzentrizität ermittelt werden kann. Die numerisch berechneten Werte für die Reibzahl spiegeln den Trend der experimentell bestimmten qualitativ sehr gut wieder, wobei erstere jedoch vorwiegend unter den gemessenen liegen.

Abstract

A new and comprehensive approach for describing, amongst others, cavitation in porous journal bearings operating under the regime of hydrodynamic lubrication is presented. The mass-conservative model couples the Reynolds equation for the fluid film with the Darcy's law for flow through porous media. The resulting system of equations is discretized using finite differences and solved iteratively by introducing an advantageous artificial pressure-density relation.

An extensive numerical analysis where the governing parameters are varied along a wide range of values is carried out. It is found that at the point of film reformation the fluid saturation will exhibit a discontinuity, which does not depend on the applied load. In order to determine the limits of applicability of this approach, specific investigations aim at evaluating the extreme cases of relatively low and high bearing loads and very long/short as well as highly porous/(almost) massive bearings. Converged solutions are obtained for values of the eccentricity ratio of up to 0.9 and interestingly, for the case of very permeable seat the friction coefficient is seen to increase around this value, in contrast with the otherwise seen decreasing trend.

Finally, the results obtained by simulations are compared with measurements performed on real-life bearings. This was achieved by an accurate interpolation scheme, which was able to predict the eccentricity ratio corresponding to the experimentally imposed load. The numerically calculated values of the friction coefficient are found to reproduce the experimentally obtained ones satisfactorily well in terms of overall trends, yet the former lie predominantly below the measured ones.

Acknowledgements

I would like to express my gratitude to my supervisor, Dr. Bernhard Scheichl, without whom this work would not be possible. Prof. Evans, Prof. Kluwick, I would like to thank you both for accepting to review my thesis and take part to my thesis defence.

Dr. Georg Vorlaufer and Dr. Stefan Eder helped me out many times throughout the years, and for that I am very grateful. Dr. Wolfgang Pahl, thank you for providing such valuable information on the experimental part of my work.

I had wonderful support from my friends whom I met in AC2T: Hakan Gocerler (you are next!), Lazlo Katona, Nicholas Shore, Peter Somkuti, Laura Lopez de la Torre. The MINILUBES project was a great opportunity, and even though I was part of it only for a short while, I will always have good friends: Lucia Pizarova, Ana-Catarina Mendonca, Francesco Pagano, Parvin Zare.

My dear Romanian friends, who always listened to me and gave me honest and hearty advice: Andreea Ștefan, Daniela Maleș, Bogdan Andrei Ștefan, Agnes Lackner.

Mama, tata, and my beautiful sister Diana, va multumesc!

And finally, my companion, Davide: Grazie, Multumesc, Thank you, Gracias, Danke, Obrigada! I don't know enough languages to thank you in! Who would have thought that a Smashing Pumpkins ticket would get you your own paragraph in the acknowledgements of my thesis!

This is dedicated to my daughter, Ozana-Rebecca, with all my love.

Contents

1	Introduction	1
2	Theory of lubrication including cavitation	3
2.1	Tribology and lubrication	3
2.1.1	Journal bearings	7
2.1.2	Reynolds equation in the lubrication gap	9
2.1.3	Frictional behaviour of journal bearings	11
2.2	Self lubricating bearings	13
2.2.1	Particularities of porous journal bearings	14
2.2.2	Highly loaded porous bearings	15
2.3	Discontinuities in the fluid film	18
2.3.1	Review of cavitation boundary conditions	19
2.3.2	Numerical algorithms for implementing cavitation	22
2.4	Thermo-physical properties of adopted lubricants	25
3	Analysis of self-lubricated systems with a porous reservoir	27
3.1	Motivation	27
3.2	Adopted cavitation model	28
3.3	Geometry of the investigated system	29
3.4	Dimensional analysis	31
3.5	Governing equations and boundary conditions	32
3.6	The case of highly permeable seat $K \gg 1$	35
4	Numerical study	37
4.1	Discretisation and iterative scheme	37
4.2	Parameter study: general case	46
4.2.1	Set-up of the input parameters	46
4.2.2	Typical pressure and saturation distribution	47
4.2.3	Influence of K and ε	51
4.3	Extended parametric study	55

4.4	Anisotropic permeability distribution	58
4.5	The case of highly permeable seat: $K \gg 1$	62
5	Experimental validation of the model	67
5.1	General motivation and purpose	67
5.2	Experimental set-up and method of data evaluation	68
5.3	Results and Discussion: Simulations versus Experiments	72
5.3.1	Comparison with full simulations	73
5.4	Comparison with established theoretical/empirical results	78
6	Conclusions	81
A	Notational conventions	85
	Nomenclature	87
	Bibliography	91

Introduction

Porous journal bearings are a type of bearings used for load support in mechanical applications where external supply of oil is not possible or difficult. Their porous seat acts as a oil reservoir which stores lubricant in between operating cycles. Their particular maintenance-free operation mechanism has drawn attention in the field since they were first used in 1925 [1], and thus, a lot of experimental but also theoretical work was dedicated to the subject [2]. Among many interesting aspects of the functioning of such bearings constitutes the phenomenon of cavitation, a discontinuity in the lubricant film that otherwise separates the shaft and the bearing. Many steps have been taken in computational theory to develop a reliable method for the prediction of cavitation (see extended review by [3]), but each came with a shortcoming. The difficulty in tackling this problem lies in the fact that cavitation is regarded as a free-boundary problem, meaning that its inception and termination occur at initially unknown locations. Moreover, from a computational point of view, cavitation is usually accompanied by steep pressure gradients, which make it difficult to handle.

Reynolds theory for flow in thin films represents a milestone in the field, and the equation with the same name is the most widely used when studying bearing flow. However, cavitation was recognized as a limitation of his theory, and therefore, the subsequent work was based on attaching appropriate boundary conditions in order to account for cavitation. Jakobson, Floberg and Olsson [4, 5] were the first to devise a mass conservative theory that came to be known as the JFO model. In their model they imposed a vanishing pressure gradient at inception (previously formulated by Swift–Stieber), but the condition at film reformation arises from an adequate mass balance at the interfaces full fluid film–cavitated region, when assuming that a fraction of the liquid is transported within the cavitated area. This however leads to a discontinuity in the pressure, which numerically poses a lot of difficulties. Elrod [6] succeeded to overcome this difficulty by applying the JFO model into a modified Reynolds equation valid for

both continuous and ruptured film. It then became known as the universal cavitation algorithm, and was applied in many studies [7–9], even if his initial method showed some stability problems. These individual contributions bring us to the current state of research in this field. Important steps were taken, but the need to gain a deeper understanding of the flow behaviour in such systems is still apparent. We will therefore aim in this work to describe in, while simple, a precise self-consistent manner the physical mechanisms involved in cavitation formation in porous bearings.

In details, we will investigate the case of a porous bearing encapsulated in a solid case, which undergoes a type of cavitation akin to vaporous cavitation. The employed model assumes that the occurred discontinuity is a region in the lubrication gap where a two-phase homogeneous mixture of vapour and oil develops after a sudden pressure drop occurred. Here, the lubricant pressure remains constant at the lubricant specific cavitation pressure, but the ratio oil–vapour varies. On the other hand, the porous seat is considered free of cavitation. We use two distinct equations to describe this coupled system: the Reynolds equation, and a 3–dimensional Darcy’s law which governs the flow through the porous medium. These are then discretized and an advanced iterative numerical scheme is used to solve the coupled system. The vast amount of the influencing parameters are reduced to a set of non-dimensional groups which describe exclusively the system, and favour compact parametric studies.

A preliminary analysis focused solely on the study of the gap pressure and the saturation of the lubricant in the cavitation region shows that a spontaneous recondensation (saturation jump) seems inevitable. We try to elucidate whether this is true for all configurations, or under certain limits this phenomenon ceases to occur. The core results are provided by an extended parameter study where the limitations of the theory, and possibly those of the numerical scheme, are investigated. It turns out that existence of solutions is tightly related to the loading conditions and particular geometrical configuration, including bearing permeability. Additionally, based on the five independent system parameters we studied a distinguished limit, namely the case of a very thin bearing seat, but in the same time of a very large permeability. The obtained results are compared with the ones found in literature, albeit available only for the case of an infinitely long bearing. In agreement with literature, we find that below a certain critical value of the chosen design parameter (Sommerfeld number) hydrodynamic lubrication can not be sustained. Interestingly, this limit appears to differ in the two approaches, which lead us to believe that cavitation plays an essential role.

As a side result, we used the performed parameter study to replicate experimental measurements. Based on the already calculated data points, we were able to predict the specific eccentricity ratio which would return the load value imposed beforehand in experiments, for a bearing operating in steady state and when all the other parameters are known. This bridged the gap between theory and experiments, without the need of further simplifications (e.g. infinitely long or narrow bearing).

Theory of lubrication including cavitation

We start by introducing the meaning and the context in which lubrication is encountered. Here the fundamental theory of lubrication will be presented, along with its application in journal bearings, and the specific conditions required by a porous journal bearing. Secondly, as a major part of the subsequent analysis, we will review the essential studies found in literature concerning the tackling of cavitation, a phenomenon affecting the lubrication of journal bearings, but which has not yet been fully understood.

2.1 Tribology and lubrication

Tribology is a relatively new branch of science, as it was coined only in the 1960's by Tabor [10], yet its effects are known since early civilizations. According to its definition, "tribology is the science and technology of interacting surfaces in relative motion and of related practices". Direct contact between solid moving surfaces induces a high friction, and ultimately wear of the parts. The goals of tribology are to minimize the effects of wear and material loss, such that the energy consumption is lower, while the efficiency is increased. Introducing a thin layer of either gas, liquid or solid, in between the two moving parts keeps the surfaces separated and direct contact is avoided. This is essentially the concept of lubrication, and the introduced third medium is referred to as the lubricant. The role of the latter is to assure smooth movement of the surfaces, carry the applied load, but also contribute to a better heat dissipation, help reduce noise and prevent corrosion.

Failure of the film lubrication can occur in time as a result of the poor quality of the lubricant itself, which under high temperature may degrade, so that the initial load

carrying capacity is greatly diminished. The lubricant performance is highly dependent on its chemical composition and physical properties, so understanding the lubricant behaviour is crucial to the study of the fluid flow.

Before continuing our explanation on the lubricant flow, we mention that, for the sake of consistency, tildes are reserved for denoting dimensional quantities.

Viscosity, a property that describes the fluid resistance to flow, or better said to shearing is the essential quantity characterizing the flow. Shear and viscosity are explained by means of the configuration depicted in Fig. 2.1a), where a layer of liquid fills the gap between a stationary plate and a moving one (fluid velocity is \tilde{u}). The fluid particles will move parallel to the two plates, and the resulting velocity profile is a linear one, varying between 0 and \tilde{u} . Assuming that the fluid film is composed of an infinite number of thin layers of liquid, the friction between them is the resistance force to motion. The required force to move the upper plate is therefore:

$$F \propto \tilde{A} \tilde{u} / \tilde{h}, \quad (2.1)$$

where \tilde{A} is the wetted area and \tilde{h} the film thickness. The proportionality constant in Eq. 2.1 is different for every fluid, and it is called the dynamic viscosity, $\tilde{\eta}$, so that Eq. 2.1 can be rewritten as

$$\tilde{F} = \tilde{\eta} \tilde{A} \tilde{u} / \tilde{h}. \quad (2.2)$$

Rearranging one obtains that the dynamic viscosity is the ratio between the shear stress and the shear velocity:

$$\tilde{\eta} = \underbrace{F/\tilde{A}}_{\text{shear stress}} / \underbrace{\tilde{u}/\tilde{h}}_{\text{shear rate}} \quad (2.3)$$

and $\tilde{\eta}$ is measured in Pa·s. Apart from the dynamic viscosity, one can encounter in engineering applications the kinematic viscosity $\tilde{\nu}$, which is nothing else but the ratio of the dynamic viscosity to the fluid density $\tilde{\nu} = \tilde{\eta} / \tilde{\rho}$.

The differential form of Eq. 2.3 was proposed by Newton and it has the form:

$$\tilde{\tau} = \tilde{\eta} \frac{\partial \tilde{u}}{\partial \tilde{y}}. \quad (2.4)$$

This equation is valid for a multitude of mineral oils and shear rates of up to $10^5 - 10^6 \text{ s}^{-1}$ [11]. Fluids respecting the generalisation of this relation within the tensor calculus of continuum mechanics for a shear-rate-independent $\tilde{\eta}$ are referred to as Newtonian fluids, while those exhibiting strong deviations are termed non-Newtonian fluids. A representation of a typical dependency of the viscosity on the shear-rate is given in Fig. 2.1b), where viscosity is seen to drop abruptly with the shear rate, a characteristic of non-Newtonian behaviour. Examples of non-Newtonian are synovial fluid, water-oil emulsions or polymer-thickened oils.

Viscosity changes with temperature, and in the case of compressible fluids, also with the applied pressure. High shearing can induce large temperature variations, such that

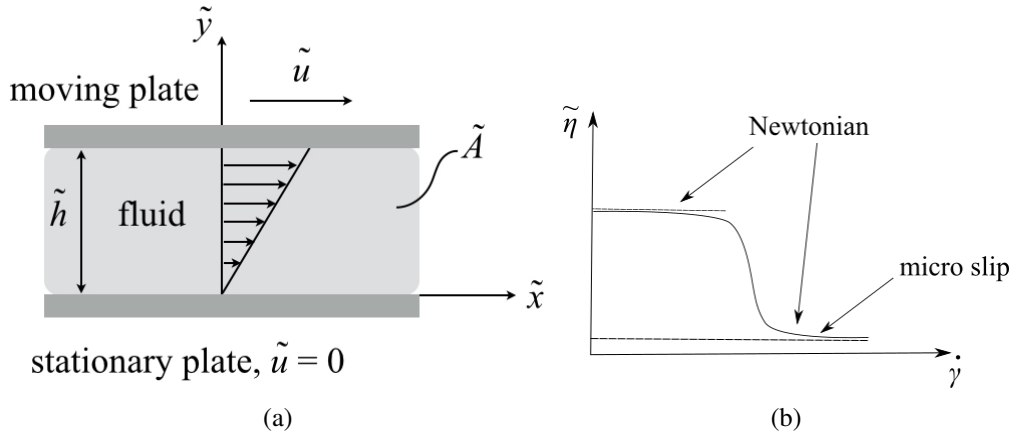


Figure 2.1: (a) Newtonian-fluid flow between two plates, (b) viscosity shear-rate dependence

the viscosity is reduced. This is why in engineering applications it is common to use the viscosity index of the lubricant (VI), which is a measure of the change in viscosity with temperature:

$$VI = 100 \frac{\tilde{\nu}_1 - \tilde{\nu}_0}{\tilde{\nu}_1 - \tilde{\nu}_2} \quad (2.5)$$

where $\tilde{\nu}_0$ denotes the oil's kinematic viscosity at 40°C and $\tilde{\nu}_{1,2}$ are the values of viscosity at 40°C for reference oils of VI = 0 and VI = 100 respectively, having the same viscosity at 100°C as the oil whose VI is to be determined. The lower the VI, the greater is the change in viscosity with temperature. Equations for viscosity-temperature dependency are available, although some arise from empirical methods. Among several available (see Crouch [12]), we mention Ubbelohde-Walther's equation for strictly Newtonian liquid, as a satisfactory accurate method:

$$\lg \lg(\tilde{\nu} + f) = a - b \lg \tilde{T}. \quad (2.6)$$

Here $\tilde{\nu}$ is measured in [mm²/s], f is a correction factor, \tilde{T} [K] the temperature, and a and b lubricant-specific constants fixed by empirical correlations. With this type of relation one can estimate the viscosity of a lubricant at a specific temperature, when two viscosity measurements are already provided.

There is no standard recipe for assuring a perfect lubrication process as the applications and operating conditions in which lubrication is required vary greatly. Lubrication engineering therefore focuses on studying the effectiveness of lubrication films and how they can be improved. Most of the times, the lubricant involved is a fluid (oil, grease,

gas), in which case, the lubrication problem reduces to the analysis of very thin films. While the characteristic scale of fluid films are much smaller than the other dimensions involved in the system (commonly the surface gap is in the range 1–100 μm), some local scales may also play a role. We refer here to the surface microscopic asperities that, under certain conditions (i.e. high applied loads) will have a height comparable to the one of the film thickness. The various types of operating conditions present in moving machinery have an enormous impact on the effectiveness of the lubrication. If, for example, the employed lubricant is too thin to carry the applied load, film failure will occur, leading to extreme friction and wear of the surfaces. On the other hand, the chemical composition of the lubricant can exhibit different behaviour when used on one material surface or another. These physical and chemical interactions are of high interest in tribology, and through the years, various scientists have developed a way to quantify the frictional behaviour between lubricated sliding contacts. Ultimately, four lubrication regimes have been identified in literature:

- boundary lubrication, when there is little (or no) lubricant present and a lot of contact between the surfaces,
- mixed lubrication, when the load is partially supported by the asperities, partially by the lubricant itself,
- hydrodynamic lubrication when the surfaces are completely separated and the load is carried entirely by the lubricant and
- elastohydrodynamic lubrication when the fluid film is very thin, but the load is very high, such that elastic deformations of the surfaces can occur.

These regimes are identified by plotting the friction over the film parameters like speed \tilde{u} , load \tilde{w} , viscosity $\tilde{\eta}$, or the most commonly known Stribeck number defined as $St = \tilde{u}\tilde{\eta}/\tilde{w}$. This type of representation is known as the Stribeck curve [13, 14], and it originates from a series of experiments conducted by the author on liquid lubricated surfaces in relative motion. He found that there exists a certain combination of operating conditions that lead to a minimum friction coefficient. Such a behaviour is reproduced in Fig. 2.2 and deserves a critical review as follows.

The zone of minimum friction identified on both curves may be interpreted as the transition from the fully hydrodynamic regime and the regimes where asperities come in contact. Ideally, a lubricated contact should exhibit a rapid transition to full hydrodynamic regime (such that the surface wear is minimum), but a slow increase in the friction coefficient along the hydrodynamic branch. The transition between the different lubrication regimes is greatly influenced by the viscosity, and the effects of an increasing viscosity are represented via the dashed line in Fig. 2.2. If the viscosity increases, the two surfaces are pushed apart earlier as a lower speed is required for flow, and the slope

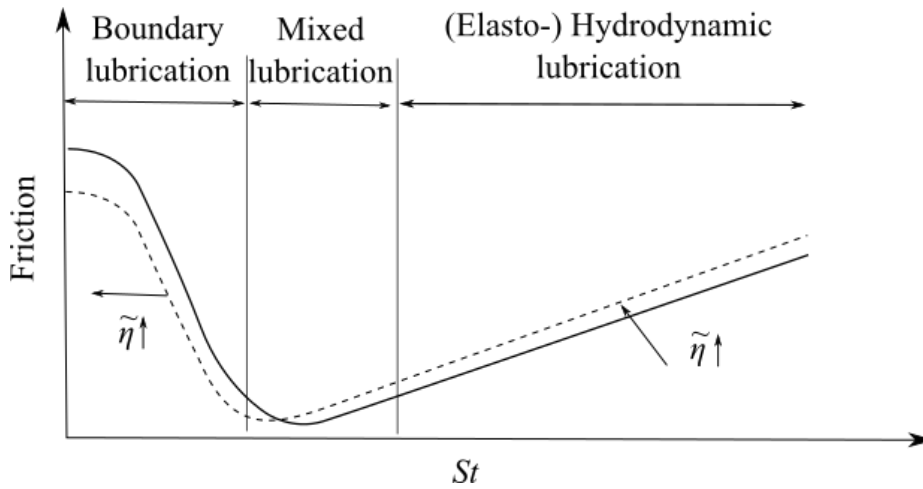


Figure 2.2: Change in friction as a function of the Stribeck number $St = \tilde{w}\tilde{\eta}/\tilde{w}$ and the effect of increasing viscosity

of the hydrodynamic branch increases. The three regimes depicted here may not always appear in the sequence shown. If the applied load is high enough to produce local elastic deformations, elastic-hydrodynamic lubrication occurs and the Stribeck curve is altered.

2.1.1 Journal bearings

One of the most widely known application for lubrication are bearings. Journal bearings are mechanical systems used in a variety of applications like automotive and household device, and which are composed of a rotating shaft mounted inside a stationary bush (hollow cylinder). The very small interstice in between the two main parts is then filled with oil or grease so that a pressure builds up in the lubricant film and can support the applied load. The film pressure is maintained either through an external pump (hydrostatic), or by the rotation of the loaded shaft which pressurizes the fluid in between two surfaces (hydrodynamic). Figure 2.3 a) shows a schematic representation of a hydrodynamic bearing (cross-section through the $\tilde{x} - \tilde{y}$ plane) where the scale of the lubrication gap was purposely exaggerated. The geometric quantities describing the bearing are its inner radius \tilde{r}_b (diameter $\tilde{d} = 2\tilde{r}_b$) and wall thickness $\tilde{\lambda}$, its width \tilde{l} . If a load \tilde{w} is applied, the rotating shaft will be displaced from its original position by an eccentricity \tilde{e} . At high enough shaft rotational speeds $\tilde{\omega}$, a convergent lubricant gap will form, providing the hydrodynamic pressure for balancing \tilde{w} . The line of centres does not coincide with the line of the applied load, but it is displaced by an angle ψ , known as the attitude angle.

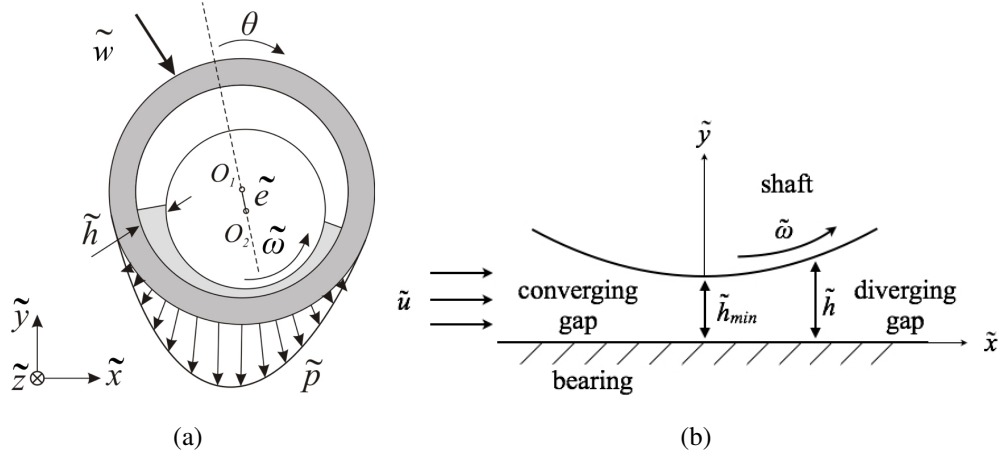


Figure 2.3: Journal bearing: (a) characteristic geometric quantities, (b) detail of the lubrication gap

An intuitive measure of the load is obtained when the geometrical distance \tilde{e} is divided by the radial clearance $\tilde{c} = \tilde{r}_b - \tilde{r}_s$, where \tilde{r}_s represents the shaft radius, yielding $\varepsilon = \tilde{e}/\tilde{c}$, the eccentricity ratio. The non-dimensional ε can take any value between $[0,1]$, and its two limiting cases are when the bearing and shaft are concentric $\varepsilon = 0$, expressing an unloaded bearing, and when they are in direct contact $\varepsilon = 1$.

A good lubrication process relies on the proper understanding of the flow occurring at the film gap and in order to understand the quantities involved, we represent a detailed section of the journal lubrication gap in Fig. 2.3 b). As the displaced lubricant moves through the gap with the velocity \tilde{u} it first passes through a convergent gap bounded by a minimum film height \tilde{h}_{min} , and afterwards flowing in a divergent gap. This pressurization of the fluid in the convergent gap between the surfaces is termed the wedge effect, and the resulting lubricant pressure profile is the crucial quantity that need to be determined. The problem would appear more complex if a fundamental simplification of the scales involved would not be applied: the slender-gap approximation, which states that the characteristic scale of the gap (described by the clearance \tilde{c}) is much smaller than the characteristic scale of the bearing (represented by either \tilde{r}_b, \tilde{r}_s). If we introduce the aspect ratio $\epsilon = \tilde{c}/\tilde{r}_b$ then the slender-gap approximation is:

$$\epsilon \ll 1. \quad (2.7)$$

This implies that the pressure does not vary across the film, i.e. in \tilde{y} -direction, and moreover that the curvature effects can be neglected. Under this assumption, if the circumferential position in the gap is given by $\theta = \tilde{x}/\tilde{r}_b$ ($\theta \in [0, 2\pi]$), the film thickness \tilde{h} at any point can be approximated by:

$$\tilde{h} \sim \tilde{c}(1 + \varepsilon \cos\theta), \quad (2.8)$$

a θ -symmetric distribution, with the minimum value occurring at $\theta = \pi$. The discontinuous layer of lubricant depicted in the divergent area of the bearing in Fig. 2.3 a) is a topic discussed in Sect. 2.3. In what follows, the governing equation applicable to the gap and the bearing essential quantities are presented.

2.1.2 Reynolds equation in the lubrication gap

In bearing design the most interesting parameter is the bearing load capacity, which describes the ability of the bearing to carry the applied load. This can be estimated by integrating the pressure in the lubricant film. In this sense, the theory developed by O. Reynolds in 1886 [15] for the flow in thin films is of fundamental importance for hydrodynamic bearings. He derived an equation for the pressure starting from the equilibrium and continuity conditions for an infinitesimal fluid element and explained the generation of a viscous fluid layer in between two surfaces moving relatively to one another. The full derivation of the Reynolds equation is widely available and thus will not be detailed here. However, its most general form will be presented below.

The conditions under which the Reynolds equation can be applied are as follows:

- the slender-gap approximation (Eq. 2.7) is valid, hence only small variations of the pressure, density and viscosity across the gap; this is referred to as the Reynolds limit;
- inertia neglected $Re \varepsilon^2 \ll 1$, where Re denotes the Reynolds number $Re = \tilde{u}\tilde{l}/\tilde{\nu}$ and the flow is laminar;
- no slip at the solid/lubricant interface;
- the fluid exhibits a Newtonian behaviour.

Using the geometrical quantities shown in Fig. 2.3 a), Reynolds equation is written in its most general form:

$$\begin{aligned} \frac{\partial}{\partial \tilde{x}} \left(\frac{\tilde{\rho} \tilde{h}^3}{12\tilde{\eta}} \frac{\partial \tilde{p}}{\partial \tilde{x}} \right) + \frac{\partial}{\partial \tilde{z}} \left(\frac{\tilde{\rho} \tilde{h}^3}{12\tilde{\eta}} \frac{\partial \tilde{p}}{\partial \tilde{z}} \right) = \frac{\partial}{\partial \tilde{x}} \left(\frac{\tilde{\rho} \tilde{h} (\tilde{u}_s + \tilde{u}_b)}{2} \right) + \frac{\partial}{\partial \tilde{z}} \left(\frac{\tilde{\rho} \tilde{h} (\tilde{v}_s + \tilde{v}_b)}{2} \right) + \\ \tilde{\rho} (\tilde{w}_s - \tilde{w}_b) - \tilde{\rho} \tilde{u}_s \frac{\partial \tilde{h}}{\partial \tilde{x}} - \tilde{\rho} \tilde{v}_s \frac{\partial \tilde{h}}{\partial \tilde{z}} + \tilde{h} \frac{\partial \tilde{\rho}}{\partial t} \end{aligned} \quad (2.9)$$

Here $\tilde{u}, \tilde{v}, \tilde{w}$ are the surface velocities in the $\tilde{x}, \tilde{y}, \tilde{z}$ directions and the subscripts s, b denote the surfaces at which the quantities are measured (in the case of a bearing, the

shaft and journal surfaces, respectively). The two terms on the left hand side of Eq. 2.9 are due to the pressure gradients in the lubricant film, and are called Poiseuille terms, while the first two terms on the right arise due to the motions of the bounding surfaces, and are called the Couette terms. The remaining two terms on the right hand side are the squeeze term (for the case when the surfaces are pushed closer to one another), and the flow contribution arising from a local time rate of density, respectively. In standard journal bearings only sliding motion is present, so the surface velocities in \tilde{y} direction are 0, and the corresponding terms can be neglected. The surface speed in \tilde{x} direction can be averaged as $\tilde{u} = (\tilde{u}_s + \tilde{u}_b)/2$. Using this simplifications, and considering only the steady-state case and pure tangential motion, the Reynolds equation is given in a more simple form as:

$$\frac{\partial}{\partial \tilde{x}} \left(\frac{\tilde{\rho} \tilde{h}^3}{\tilde{\eta}} \frac{\partial \tilde{p}}{\partial \tilde{x}} \right) + \frac{\partial}{\partial \tilde{z}} \left(\frac{\tilde{\rho} \tilde{h}^3}{\tilde{\eta}} \frac{\partial \tilde{p}}{\partial \tilde{z}} \right) = 12\tilde{u} \frac{\partial(\tilde{\rho}\tilde{h})}{\partial \tilde{x}} \quad (2.10)$$

The solution of the Reynolds equation is the film pressure \tilde{p} , yet manipulation of the full Reynolds equation is difficult, and numerical solutions are usually more easy to be obtained. However, for the case of pure hydrodynamic lubrication, where the fluid properties (e.g. density) do not vary significantly, three journal bearing approximations are available, all of which are presented below.

Closed-form solutions of the Reynolds equation

The subsequent solutions are useful for many bearings where the lubricant can be assumed as incompressible, namely the liquid density is taken as constant $\tilde{\rho} = const.$ Hence, the load-carrying capacity \tilde{w} of a journal bearing depends essentially on the eccentricity of the displaced journal, the rotational speed, fluid viscosity and the geometry of the bearing (radius, width, clearance):

$$\tilde{w} = f(\tilde{e}, \tilde{\omega}, \tilde{\eta}, \tilde{r}_b, \tilde{l}, \tilde{c}) \quad (2.11)$$

The simplifications consist of reducing the bearing geometry in such a way that the major part of the flow contributing to the lubrication process occurs only in one dimension, or assuming the idealised case of an almost concentric bearing-shaft pair.

1) The *infinitely-wide journal bearing approximation* considers that the width of the bearing \tilde{l} is much larger than its diameter $\tilde{d} = 2\tilde{r}_b$. This implies that the major part of the flow occurs in the circumferential direction, and the axial flow is so small that it can be neglected. In terms of the Reynolds equation, the second term on the left hand side in Eq. 2.10 drops out and the corresponding equation is:

$$\frac{\partial}{\partial \tilde{x}} \left(\tilde{h}^3 \frac{\partial \tilde{p}}{\partial \tilde{x}} \right) = 6\tilde{\eta}\tilde{u} \frac{\partial \tilde{h}}{\partial \tilde{x}} \quad (2.12)$$

By using Sommerfeld's substitution [16] and the circumferential coordinate $\theta = \tilde{x}/\tilde{r}_b$ one can obtain a solution in a closed form:

$$\tilde{p} = 6 \frac{\tilde{\eta} \tilde{u} \tilde{r}_b}{\tilde{c}^2} \left[\frac{6\varepsilon \sin\theta(2 + \varepsilon \cos\theta)}{(2 + \varepsilon^2)(1 + \varepsilon \cos\theta)^2} \right]. \quad (2.13)$$

The friction force due to the shearing of the lubricant is then given by:

$$\tilde{f}_f = \int_0^{2\pi} \left(\frac{\tilde{h}}{2\tilde{r}_b} \frac{d\tilde{p}}{d\theta} + \frac{\tilde{\eta} \tilde{r}_b \tilde{\omega}}{\tilde{h}} \right) d\theta \quad (2.14)$$

2) The Ocvirk approximation assumes a *short-width bearing*, $\tilde{d} \gg \tilde{l}$, such that the first term in Eq. 2.10 can be neglected. The agreement with this approximation increases for $\tilde{d}/\tilde{l} > 2$. The pressure distribution is now given by:

$$\tilde{p} = \frac{6\pi\tilde{\omega}\tilde{\eta}}{\tilde{c}^2} \frac{\varepsilon \sin\theta}{(1 + \varepsilon \cos\theta)^3} \left(\frac{\tilde{l}^2}{4} - z^2 \right) \quad (2.15)$$

In both cases the force per unit width can be easily obtained by integrating the pressure over the bearing area:

$$\begin{aligned} \tilde{w}_x &= \int_0^\pi \tilde{p} \tilde{r}_b \sin\theta \, d\theta, & \tilde{w}_y &= - \int_0^\pi \tilde{p} \tilde{r}_b \cos\theta \, d\theta \\ \tilde{w} &= \sqrt{\tilde{w}_x^2 + \tilde{w}_y^2} \end{aligned} \quad (2.16)$$

3) Finally, Petroff [17] assumed ideal operating conditions: lightly loaded bearing such that the shaft and the bearing are almost concentric, the gap is fully filled with liquid and no leakage occurs. Under these conditions he derived a straightforward relation for the frictional moment in bearings:

$$\tilde{m}_f = \frac{\tilde{\eta} \tilde{l} \pi^2 \tilde{d}^3 \tilde{\omega}}{2\tilde{c}} \quad (2.17)$$

This approach along with 1) and 2) work reasonable well for their specific cases, but very often such simplifications are not applicable. Therefore, numerical solutions are still necessary in order to calculate the pressure in the lubricant.

2.1.3 Frictional behaviour of journal bearings

The ultimate goal in solving the Reynolds equation (either the reduced or full geometry) is to obtain a pressure profile, which, by integration provides the two forces occurring in the bearing: the load and the friction force. The ratio of these two is in fact the friction coefficient μ , one of the most important performance parameter for the journal bearing:

$$\mu = \frac{\tilde{f}_f}{\tilde{w}}. \quad (2.18)$$

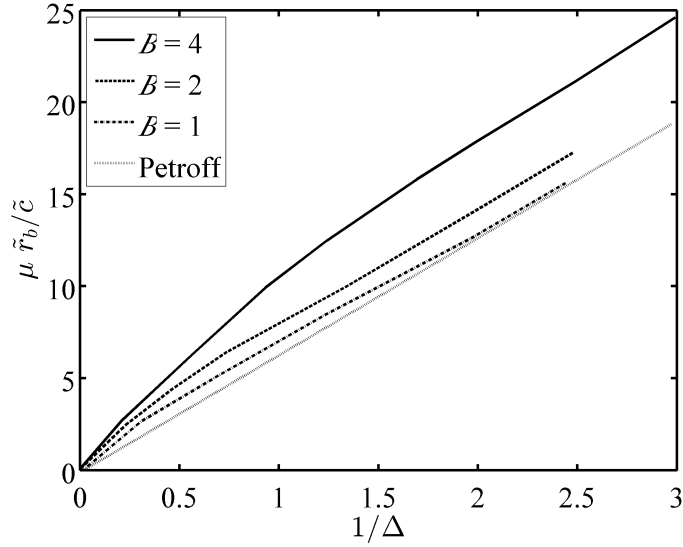


Figure 2.4: Results according to Cameron [18]: normalized friction coefficient $\tilde{r}_b/\tilde{c}\mu$ vs. the inverse of the Sommerfeld's number $1/\Delta$ for various aspect ratios $B = 2\tilde{r}_b/\tilde{l}$

Even if the supplied lubricant prevents dry friction (direct contact between bearing and shaft), the bearing friction (due to shearing) should be kept at a minimum level. This can be achieved by either improved geometry, material or lubricant type. Engineers use the friction coefficient in order to quantify the change in the frictional behaviour in journal bearings, and here, the classical Stribeck curve (see Fig. 2.2) proves a very useful approach. Another parameter used in this kind of representation is the Sommerfeld number (or duty parameter) defined as $\Delta = \tilde{w}/(\tilde{\eta}\tilde{u}\tilde{l})(\tilde{c}/\tilde{r}_b)^2$. The lubrication regimes described in Sect. 2.1 represent typical behaviour for lubricated pairs, however, in some situations not all identified branches can be simultaneously seen on the Stribeck curve.

A fundamental formula for calculating the friction coefficient in bearings was given in 1949 by Cameron and Wood [18], and it was obtained for the case $2\tilde{r}_b = \tilde{l}$ and the assumption that the viscosity is constant along the bearing. It relates the friction coefficient and Sommerfeld number as follows:

$$\mu \frac{\tilde{r}_b}{\tilde{c}} = \frac{1}{\Delta} \frac{2\pi}{\sqrt{1-\varepsilon^2}} + \frac{\varepsilon}{2} \sin\psi. \quad (2.19)$$

Their results show that the curves $\tilde{r}_b\tilde{c}/\mu$ vs. $1/\Delta$ obtained for various values of a defined aspect ratio of $B = 2\tilde{r}_b/\tilde{l}$ are parallel to the line describing the case of a lightly loaded bearing (Petroff's solution), as seen in Fig. 2.4. As B is increased, the lines are further displaced from the concentric case, apart from the region near $1/\Delta \rightarrow 0$.

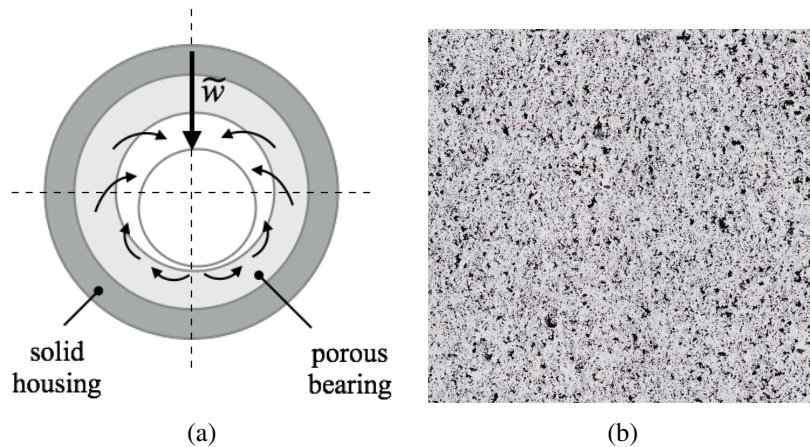


Figure 2.5: Porous bearing: (a) oil circulation from/into the porous seat, (b) metallographic sample of a cross-section of a porous bearing. (Source: GKN Sinter Metals)

2.2 Self lubricating bearings

Self lubricating bearings operate in a similar manner as classical journal bearings, yet without the need of an external source of lubricant. Sintered bearings are a category of self lubricating bearings which are able to store the necessary amount of lubricant within their porous seat. The characteristic porosity of the seat (ϕ , the ratio between the cumulated volume of the pores and the total volume) is controlled during the sintering process and it usually amounts to 10-40% of the total bearing volume [19].

The basic principle behind the functioning of these type of bearings is that their porous seat acts as a reservoir of the fluid necessary to achieve a cohesive film of lubricant filling the slender interstice separating the shaft from the seat. In the loaded part of the bearing the lubricant is pushed into the porous channels of the seat, while in the unloaded part oil will be drawn from the pores, contributing in refilling the lubrication gap [20], as depicted in Fig. 2.5 a). This mechanism of oil circulation has been demonstrated experimentally in the above mentioned study by impregnating the bearing with a coloured oil and wrapping it in a felt cylinder impregnated with uncoloured oil. Periodic re-impregnation is not necessary since the bearing remains filled with liquid. This represents an advantage for applications where the access to the bearing is restricted or not possible. Moreover, porous bearings offer more flexibility in manufacturing as compared to standard solid bearings, as their composition and their porosity degree can be decided according to the desired operating conditions.

In contrast to their simple operation and maintenance, the flow through the porous structure is rather complex. The porous network consists of highly interconnected microscopic channels of random distribution (Fig. 2.5 b) that cannot be described in an

exact manner. Darcy's classical experiment [21] on water flow through sand beds gives a proportionality relation between the total volume of fluid percolating a filter bed and the pressure drop across its length. His theory holds as long as the flow is laminar and the flow velocities are rather low. In differential form, it writes:

$$\tilde{q} = -\frac{\tilde{\Phi}}{\tilde{\eta}} \nabla \tilde{p}, \quad (2.20)$$

where \tilde{q} is the *seepage velocity*, as termed by Scheidegger [22], $\nabla \tilde{p}$ the pressure gradient. $\tilde{\Phi}$, the permeability, expresses the ability of a porous medium to allow fluid to pass through. The validity of the Darcy's law has been verified by means of experiments [23, 24], but also theoretical (see derivation by Whitaker [25]).

However, an accurate estimation of the permeability entering Darcy's law has not yet been established since merely its measurement poses difficulties. On the other hand, the scalar porosity ϕ can be measured much more easily, but an accurate relationship between $\tilde{\Phi}$ and ϕ is not yet available. A number of semi-empirical expressions and theories were proposed in this sense, among which the one advanced by Kozeny [26] remains the most widely known. His approach is based on the rough assumption that the porous medium is equivalent to a set of thin circular channels exhibiting varying area cross-sections embedded in a rigid matrix. The equation he derived expresses the dependence of the permeability on the specific overall surface area of the porous medium S_a :

$$\tilde{\Phi} = \frac{c\phi^3}{S_a^2}. \quad (2.21)$$

c is referred to as the 'Kozeny constant' and it varies with shape (e.g. for a circle $c = 0.5$, for a strip $c = 2/3$). However, the accuracy of this theory was never fully proven, as studies like the ones by Childs and Collis-George [27] criticize that high deviations from the theory are likely to occur.

Nevertheless, Darcy's law constitutes a fundamental law in earth sciences, particularly in hydrogeology, as long as the flow remains laminar. The latter condition is widely assumed in the case of porous journal bearings, and so, Darcy's law was applied many times in the simulation of the flow through porous bearings [9, 19, 28, 29]. The classical Darcy equation was extended by Brinkmann [30], where the viscous shear effects are considered, and later on when inertial effects were included, via the Darcy-Forchheimer law [31].

2.2.1 Particularities of porous journal bearings

The interest the industry has shown in porous journal bearings (PJBs) encouraged a lot of research in this field. Apart from the multitude of experiments conducted on PJBs, [32–34] to mention just a few, several authors have dedicated to the theoretical analysis of porous bearings, in particular to accurately describe the flow through

the porous matrix and find the most appropriate boundary condition at the interface lubricant–porous matrix (see [35] and the references therein). The analysis made by Cameron and Morgan [19] is worth mentioning as a fundamental development in the study of porous bearings. The authors took on the assumption of a narrow seat, i.e. $\tilde{l}/\tilde{d} \rightarrow 0$ and offered an analytical solution which was also verified experimentally [36]. Their analysis showed that there exists a threshold (in the lubrication of short porous bearings) beyond which hydrodynamic lubrication cannot be achieved. The critical limit is identified by plotting the calculated friction coefficient versus the Sommerfeld number for different values of the design parameter, defined as a function of the bearing wall thickness ($\tilde{\lambda}$), clearance and permeability:

$$\Psi = \frac{\tilde{\phi} \tilde{\lambda}}{\tilde{c}^3}. \quad (2.22)$$

Regarding the obtaining of the friction coefficient, the derivation of Eq. 2.19 shows it to be universally valid for solid and porous bearings and any geometry having $\tilde{l}/\tilde{r}_b = O(1)$. The results of this strategy for various design parameter values Ψ are illustrated in Fig. 2.6 a), along with the solution for a solid bearing $\Psi = 0$. For high values of the Sommerfeld number the results collapse on the same line, and one cannot distinguish between the bearing types. As Δ decreases, the friction coefficient increases dramatically, specifically at a critical point Δ_c which varies according to Ψ . The region of very high friction coefficients corresponds to the case of highly loaded bearings, when the film thickness in the lubrication gap becomes comparable to the height of the surface asperities. However, before the sharp increase, μ will first exhibit a minimum, localized at Δ_{min} , which is actually of more interest from the design point of view. These findings demonstrate the importance of the design parameter and the implied limitations to the full hydrodynamic lubrication. The involved equations have been further improved by Rouleau [37], who argued that the initial solution could not satisfy an arbitrary boundary condition at $\tilde{z} = \tilde{l}/2$, and Murti [38] who extended the theory as to solve the same problem but with arbitrary wall thickness. In any case, the findings by Morgan and Cameron [19] [36] provide valuable insight on the fundamental principles of lubrication in PJBs.

2.2.2 Highly loaded porous bearings

When the load acting on the shaft is very large, the lubricant layer between the surfaces becomes so small such that its thickness is comparable with the height of the surface asperities. In this situation asperity contact will take place and therefore hydrodynamic lubrication is no longer possible. In plain (solid) bearings this issue is mathematically dealt with by applying various techniques (e.g. stochastic, deterministic or homogenization [39]) aimed at approximating the film thickness in the region $\varepsilon \rightarrow 1$. Porous bearings on the other hand, exhibit very smooth surfaces, such that roughness effects are

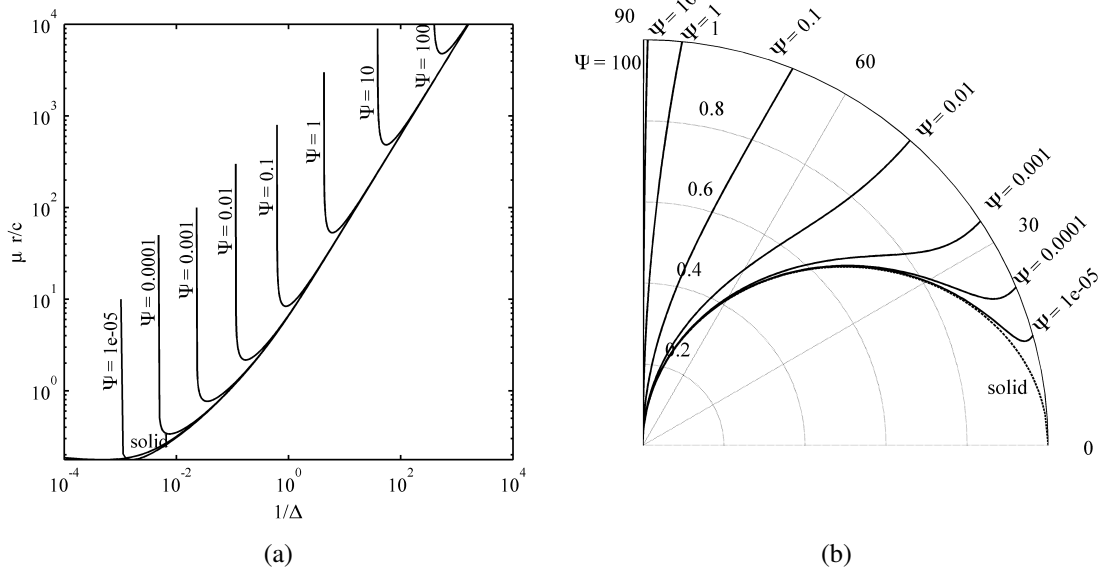
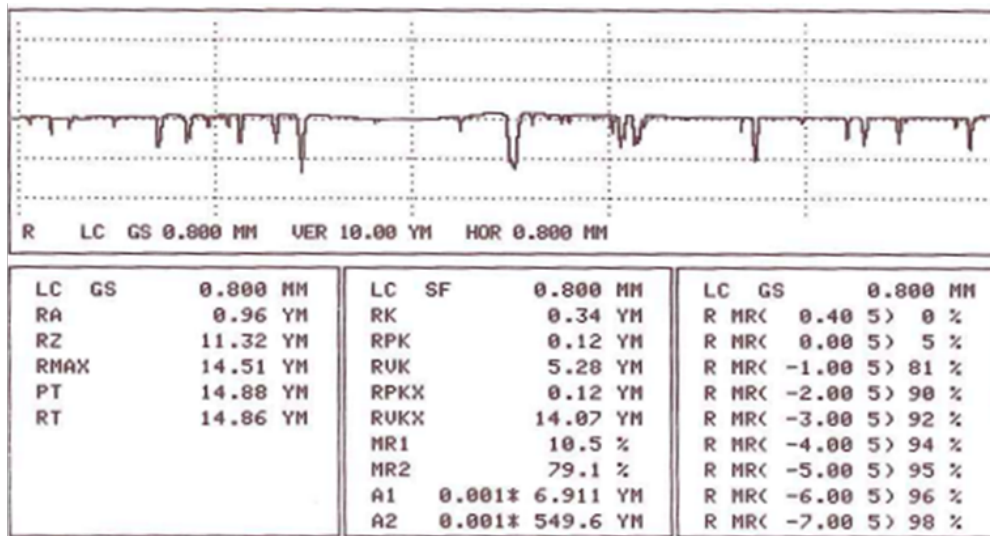


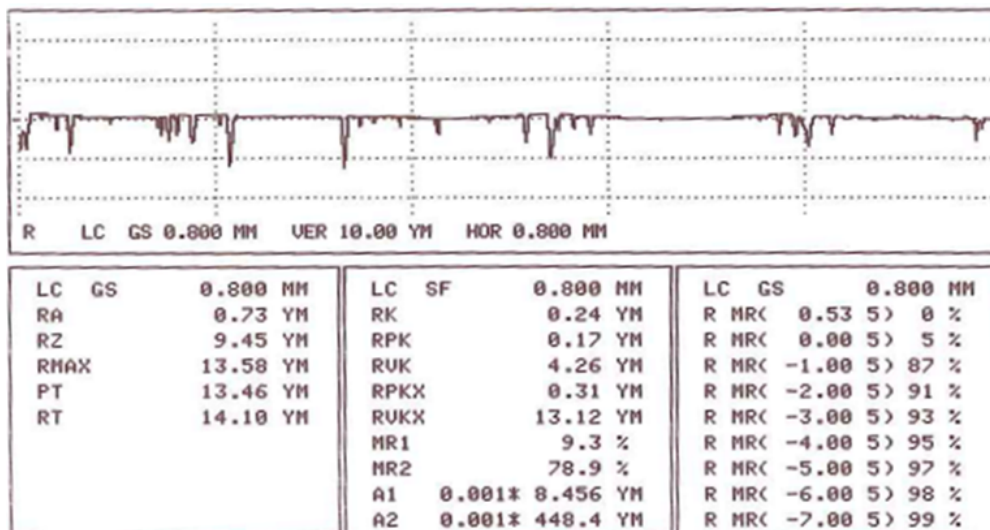
Figure 2.6: Results by Cameron [36] for various values of the design parameter Ψ : (a) friction coefficient vs. the inverse of Sommerfeld number, (b) attitude angle vs. the eccentricity ratio

not an issue when high loads are applied. An example of a surface profile of a porous bearing is given in Fig. 2.7, where two measurements of a representative porous bearing were taken before and after operation. There the recorded valleys in the roughness correspond to the depth of the pores, and no other roughness peaks are observed. After 15 hours of operation the average roughness decreases by 25%. This can be explained in the following manner: direct contact between the bearing and the shaft can generate the effect of pore closure, at least at the upper surface. The effect is that the surface permeability can be reduced, as is the porosity (exemplified by Fig. 2.7). This ultimately affects the design parameter Ψ and implicitly the minimum S_o that can be achieved so that the design curves in Fig. 2.6 a) are not valid. The lack of lubricant sufficient to separate the surfaces can occur also during start-up and interrupted operation, as there is not enough lubricant in the gap to support the applied load.

Another particularity of PJBs is the resulting attitude angle at varying loads. Using the earlier formula provided by Cameron, (Eq. 2.19), the attitude angle is easily calculated for the same set of design parameters as in [36] and in the same approximation, $\tilde{l}/\tilde{d} \rightarrow 0$, and is represented in Fig. 2.6 b). The dependency of ψ on ε is drastically attenuated when Ψ increases, up to such a high value of Ψ that they become independent. For a solid bearing and under a maximum load $\varepsilon = 1$, the line of centres will be perfectly aligned with the line of the applied load, i.e. $\psi = 0$, as in the perfectly concentric case



(a)



(b)

Figure 2.7: Example of the surface profile of a porous bearing measured on a length of 5 mm on the inner diameter of the bearing (a) before operation, (b) after 15 hours of operation under a load of 1 N/mm². The recorded irregular crevices are the pores of the bearing surface, which, after a regular operation cycle are either diminished or closed completely. The roughness parameters R_a , R_z , R_{max} are used to quantify the changes in the profile. (Image source: GKN Sintered metals)

$\varepsilon = 0$. On the other hand, this behaviour is never encountered when the eccentricity of a porous bearing approaches 1. In this case, the flow arising through the pores of the porous matrix (even for very low values of Ψ) is enough to displace the journal from the perfectly concentric position.

2.3 Discontinuities in the fluid film

We have seen that by means of Reynolds theory one can estimate the pressure distribution and load capacity in a journal bearing, the essential quantities in bearing design. However, this theory has its shortcomings, as it is strictly valid for an assumed fully coherent fluid film, like in the case of quite low values of the eccentricity ratio $\varepsilon \leq 0.5$. In reality, the lubricant often exhibits an almost discontinuous phase change from the initial liquid phase, when the hydrodynamic pressure drops significantly in the divergent part of the lubrication gap, even below the ambient pressure. As a result, in the divergent zone of the lubrication gap a discontinuity in form of a gas or vapour cavity will occur, as depicted already in Fig. 2.3 a) but not clarified so far. This discontinuity associated with the sudden pressure decrease is referred to as cavitation.

Since this limitation of the Reynolds theory was recognized, many authors have tried to elucidate the mechanisms and characteristics of this phenomenon. The particular interest in tribological systems is due to the fact that these systems are usually subject to high tangential shear and abrupt changes of pressure which ultimately favor film rupture. The dynamics of the cavity is very complex and can therefore shape as traveling, vibratory or fixed cavities, as Swales [40] first categorized them. Another way of distinguishing between the various types of cavities is by their composition, i.e. whether they contain vapor, gas or a combination of the two. A quite lucid categorisation of these mechanisms was provided by Dowson and Taylor [41] and also Braun [42]:

- (i) *gaseous cavitation* assumes the penetration of quite large amounts of gas (air) from the surroundings, thus favouring film rupture from the surface and accompanying the formation of a bubble or cavity as the pressure falls below the saturation pressure;
- (ii) *pseudo-cavitation* as a form of gaseous cavitation, when an existing cavity bubble expands due to a further decrease of the lubricant pressure;
- (iii) *vaporous cavitation* occurs when the lubricant pressure falls below the vapour pressure such that an inner partial vaporization takes place, leading to a mixture phase composed of liquid (containing dissolved gases), and vapour (containing released gases). Assuming that the process is an isothermal, thermodynamically stable one, and that the dissolved gases occur as tiny colliding bubbles, the cavi-

tation region can be viewed as a homogeneous two-phase mixture exhibiting very small pressure changes, and essentially $\tilde{p} = \text{const}$.

It was shown experimentally that vaporous and gaseous cavitation may occur in bearings [41, 43, 44] under both steady state and dynamic loading conditions, however capturing the exact position at which the lubricant film ruptures remains a difficult task to accomplish. From a theoretical point of view the situation is not much different either, as many scientists have tried to find the most appropriate boundary condition which connects the fully liquid area to the cavitating one and accurately predict the cavitation boundaries. The earliest efforts in both directions are marked by the symposia ‘‘Cavitation in real liquid’’ organized in Michigan 1962 and the ‘‘1st Leeds-Lyon Symposium’’ in 1974, yet it is safe to say that the issue of cavitation has not been satisfactorily elucidated yet. Nevertheless, several theoretical models have contributed to a better understanding of the phenomenon. These are reviewed in the following section.

2.3.1 Review of cavitation boundary conditions

Reynolds famous equation was initially solved by Sommerfeld [16], who used a trigonometric substitution for obtaining analytical solutions. The result is an anti-symmetric pressure distribution along the circumferential coordinate θ , as depicted in Fig. 2.8. The negative pressures in the region $\pi - 2\pi$ however, are not physically realistic. This led to an even more simplistic way of accessing for the occurrence of cavitation, namely by keeping the gap pressure constant in the regions where the solution of the Reynolds equation predicts lower ones otherwise. In other words, in the area of subambient pressures, originating at the point of minimum film thickness, the lubricant pressure \tilde{p} will automatically be set to \tilde{p}_{cav} , no matter how low \tilde{p}_{cav} would be. Gumbel [45] accounted for film rupture by stating that cavitation occurs very close to the location of the minimum film thickness, at a prescribed constant pressure \tilde{p}_{cav} . However, this so-called half-Sommerfeld or Gumbel boundary condition is incorrect insofar as it does not respect continuity of mass. Hence, a more suitable boundary condition would have to provide the continuity of the mass flux across the liquid-mixture interface. Assuming that only a fraction φ of the gap height carries the liquid (the remaining one being filled with cavitating lubricant) and taking $\tilde{\rho}_m, \tilde{\rho}_l$ as the densities in the cavitating (mixture) and liquid regime, respectively, a more general condition respecting continuity (see [46]) reads:

$$\frac{1}{\tilde{r}} \frac{\partial \tilde{p}}{\partial \tilde{\theta}} - \tilde{r} \frac{\partial \tilde{p}}{\partial \tilde{z}} \frac{d\theta}{d\tilde{z}} = \frac{6\tilde{U}\tilde{\eta}}{\tilde{h}^2} [1 - 2\varphi - (1 - \varphi)S], \quad S := \frac{\tilde{\rho}_m}{\tilde{\rho}_l} \quad (2.23)$$

More importantly, condition 2.23 holds for both inception and termination of cavitation, while inside the cavitation region the hereby introduced lubricant saturation S ($0 < S \leq 1$) becomes the dependent variable in regions where the gradient of \tilde{p} is 0.

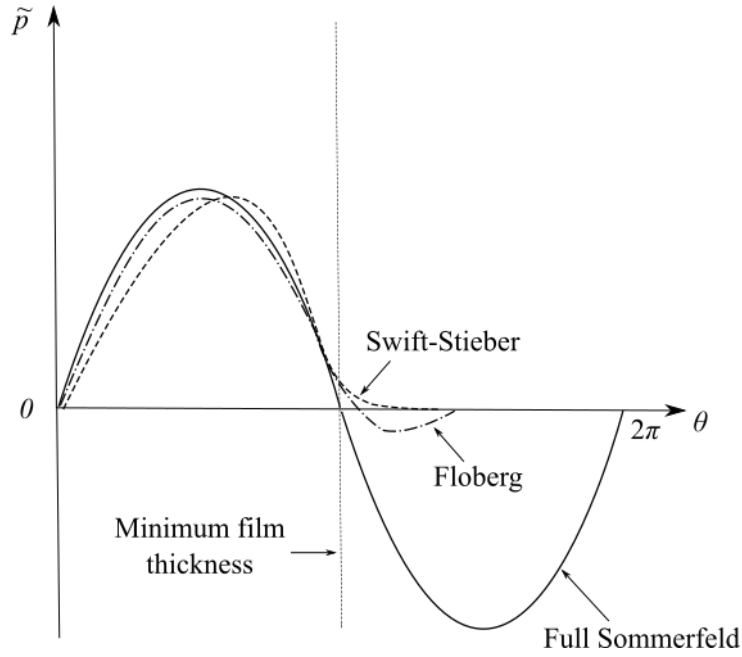


Figure 2.8: Pressure distribution along the circumferential coordinate of a journal bearing: different cavitation models

Swift and Stieber [47, 48], although working independently, considered that the inception of cavitation is conditioned by vanishing pressure gradient and restricted the pressure in the cavitation region to \tilde{p}_{cav} :

$$\frac{d\tilde{p}}{d\tilde{x}} = \frac{d\tilde{p}}{d\tilde{y}} = 0, \tilde{p} = \tilde{p}_{cav}. \quad (2.24)$$

This is also commonly referred to as Reynolds boundary condition and derived from Eq. 2.23 when a continuous entrainment of gas is assumed, $\varphi = 0$ and $S = 1$. In the divergent area of the bearing the flow is assumed to break down into layered streamers of gas and liquid across the bearing width (see Fig. 2.10 a), and the flow to be driven solely by the rotational movement of the shaft, such that only the Couette contribution remains active. Although this condition works well at moderate loads [49], it does not properly handle film reformation [50] nor can accept sub-ambient pressures. In 1963 Taylor [51] performed several experiments on cavitation in narrow passages where he was particularly interested in measuring the position of the meniscus of the cavitation bubble. His experiments showed that cavitation has the appearance of a separated flow, where the lubricant moves above and/or below the cavity, and is triggered by a pressure gradient upstream of the meniscus. Taylor pointed out that in fact, two types of cavitation can be identified. The first one does not consider the effects of surface tension, while the second type, separation cavitation, is strongly affected by surface tension. In

the latter case, the flow is two dimensional and the fluid is carried under and/or the air cavities, see Fig. 2.9. He considered that the number of streamers in the divergent region is controlled by the non-dimensional capillary number Ca , a ratio between the sliding velocity \tilde{u} , fluid viscosity $\tilde{\eta}$ and surface tension, \tilde{t} : $Ca = \tilde{\eta} \tilde{u} / \tilde{t}$. While Taylor's

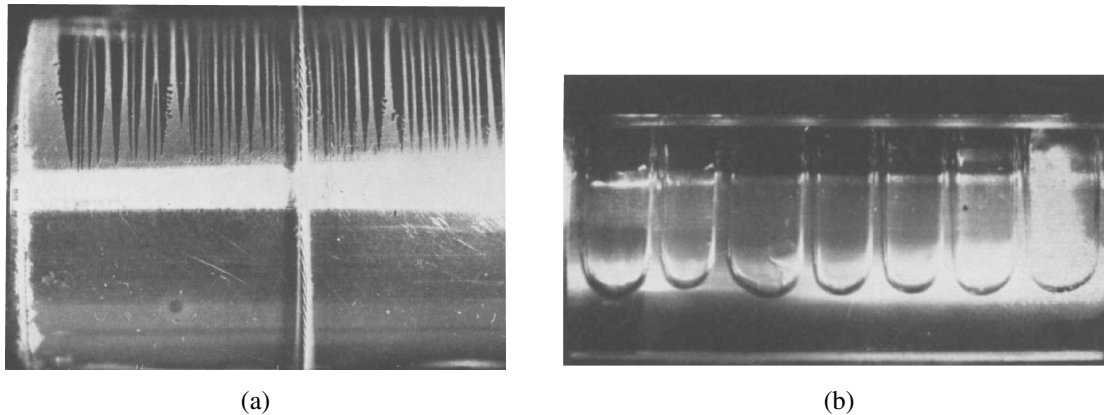


Figure 2.9: Cavitation fingers according to experiments by Taylor: (a) $Ca = 0.03$ many thin streamlets, (b) $Ca = 2.2$ few, wide streamlets

separation theory can accommodate subatmospheric pressures, it neglects the influence of the sub-cavity pressures upstreams of the cavitated regions, i.e. the pressure an oil can withstand before cavitating. On contrast, Floberg [52, 53] showed that sub-cavity pressures affect the extent of cavitation: when the number of streamers is decreased, the position of the cavitation-film interface moves downstream. In his theory the cavity extends the transverse section of gap and the flow is carried between the cavities. Additionally, the cavity is filled almost entirely with air and no net mass flow enters the cavitation bubble. Based on these assumptions Floberg formulated a condition that governs both the upstream and downstream cavitation boundary, by setting $S = 0$ and $\varphi = 0$ in Eq. 2.23:

$$\frac{1}{\tilde{r}} \frac{\partial \tilde{p}}{\partial \theta} - \tilde{r} \frac{\partial \tilde{p}}{\partial \tilde{z}} \frac{d\theta}{d\tilde{z}} = \frac{6\tilde{U}\tilde{\eta}}{\tilde{h}^2}, \quad (2.25)$$

In his analysis he was able to calculate the number of streamers on unit width based on the minimum sub-cavity pressure. Braun [42] studied Swift and Stieber model, separation theory and Floberg's model and concluded that out of all three proposed cavitation conditions, the latter reflects best the experimental findings.

Surface tension, gravity and fluid inertia effects were considered by Coyne and Elrod [54, 55], in a study where they determine the rupture of the liquid-gas interface from a fixed point on a stationary surface. Cavitation develops as a single bubble which is being swept away on the opposing moving surface, like the one represented in Fig. 2.10 b). The authors assumed a quadratic tangential velocity profile across the film and used the

Navier-Stokes equations to describe the flow upstream of the rupture point. Two boundary conditions were then derived to match the upstream Reynolds pressure with the one from the separating film. The first one, when the inertia and gravity forces are neglected, reads:

$$\frac{d\tilde{p}}{d\tilde{x}} = \frac{6\tilde{\eta}\tilde{U}}{\tilde{h}^2} \left(1 - 2\frac{\tilde{h}_\infty}{\tilde{h}}\right), \quad (2.26)$$

where \tilde{h}_∞ represents the asymptotic film thickness downstream, and is function of the liquid-gas surface tension and the viscous forces. The second boundary condition related the pressure to the radius of curvature at the separation point R_0 , the surface tension \tilde{t} and the pressure change upstream of the cavity:

$$\tilde{p} = -\frac{T}{R_0} + \delta\tilde{p}. \quad (2.27)$$

Separated-flow models use the continuity of mass flux to define the cavitation interface. This, however, is not sufficient as mass at a liquid/gas boundary should be preserved in both the cavitation region and perpendicular to the boundary. The seminal work of Jakobsson-Floberg-Olson [4, 5] is the first theory (known as the JFO theory) to respect conservation of mass across the whole bearing. They assumed that film rupture occurs when the pressure falls below the respective saturation pressure, forming thin layers of lubricant that extend fully to both neighbouring surfaces of the clearance gap (see Fig. 2.10 a). In fact, experimental images taken by Cole and Hughes [56] support very well the JFO theory. In the cavitation region the fluid is transported through a Couette-type flow, such that the pressure is constant throughout. The boundary conditions for cavitation inception are set to vanishing pressure gradients as in Eq.2.24. At inception and reformation continuity is respected by:

$$\tilde{q}_{\theta,i}\Delta z - \tilde{q}_{z,i}\Delta\theta = \tilde{q}_{cav}\Delta z, \quad (2.28)$$

where $i = 1, 2$ are the upstream and downstream positions of the mass fluxes \tilde{q} . This finally leads to a differential equation which provides a relation between the pressure gradient and the corresponding film thickness (see Eq. 2.23). Thereby the strictly mass-preserving JFO model completes a self-consistent theory of lubrication within the Reynolds limit.

2.3.2 Numerical algorithms for implementing cavitation

As computational power increased over time, so did the interest in solving cavitation by means of numerical methods. The JFO theory was applied many times, due to its robustness and its ability to predict the shape of cavitation. Many algorithms were therefore developed for its implementation in numerical programs, and few of what we consider the most representative ones will be reviewed below.

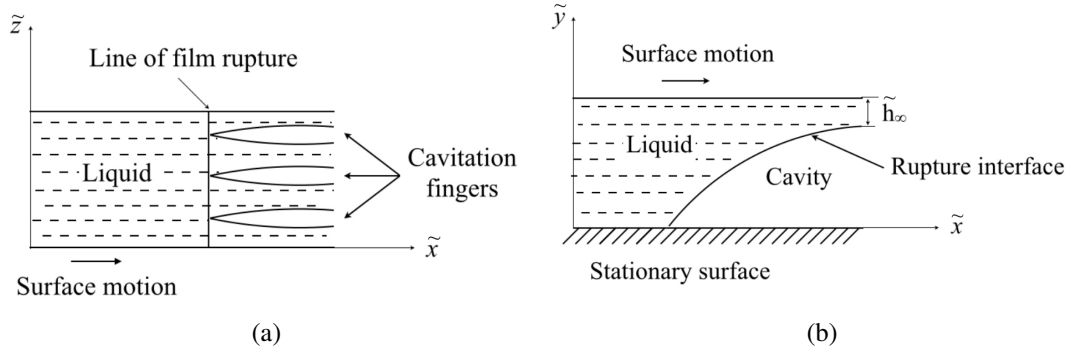


Figure 2.10: Film rupture models: (a) Reynolds boundary condition, (b) separation according to Coyne and Elrod [54, 55]

Elrod and Adams [57] and later on Elrod [6] successfully solved a modified Reynolds equation with imposed JFO conditions. Their simple approach was based on introducing in the Reynolds differential equation a switch function that accounts for the presence of cavitation and preserves the continuity of mass on the entire flow domain. A cavitation index g has the role of switching between the two regimes (cavitated and non-cavitated flow) and it is defined as a function of θ^* , the density ratio of the liquid and cavitated region ($\theta^* = \tilde{\rho}_l / \tilde{\rho}_c$):

$$\begin{cases} g(\theta^*) = 1, & \tilde{p} \geq \tilde{p}_{cav}, \rho \geq \rho_c \\ g(\theta^*) = 0, & \tilde{p} \leq \tilde{p}_{cav}, \rho \leq \rho_c. \end{cases} \quad (2.29)$$

Under the assumption that in the cavitated region only a fraction of the film gap is occupied, the resulting modified Reynolds equation is governed by θ^* and the void fraction in the liquid is $1 - \theta^*$. The lubricant pressure and the density are related via the isothermal bulk modulus of the fluid (or expansion coefficient), $\beta_l = \tilde{\rho}_l \partial \tilde{p} / \partial \tilde{\rho}_l$, which by integration for a constant β_l leads to a relationship $\tilde{p} - \tilde{p}_{cav}$:

$$\tilde{p} = \tilde{p}_{cav} + \beta_l \ln \theta. \quad (2.30)$$

The algorithm showed encouraging results when applied in the case of a slider bearing and grooved journal bearings. However, while this model worked well for compressible cases, it proved to become unstable when incompressible cases were considered. The authors used an alternating-direct-implicit method (ADI), but they admitted that the encountered instabilities suggest the need to search for a more direct form of solving the system.

Vijayaraghavan and Keith [8] attempted to improve Elrod's algorithm by directly coupling the switch function g with the bulk modulus β_l so that $g\beta_l = \partial \tilde{p} / \partial \theta^*$ and $\tilde{p} = \tilde{p}_{cav} + g\beta_l \ln \theta^*$. Similar with Elrod, they obtained a new modified Reynolds equation,

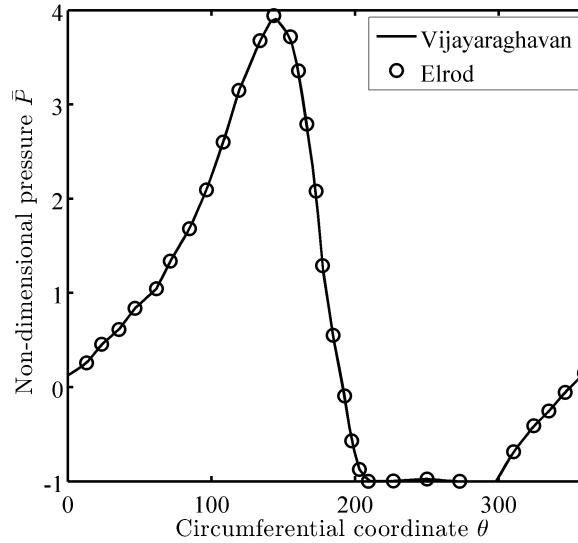


Figure 2.11: Comparison of circumferential non-dimensional pressure profiles of a submerged journal bearing at a location $1/5 \tilde{l}/\tilde{d}$ from the centerline: Elrod [6] vs. Vijayaraghavan et. al. [8] Reference non-dimensional cavitation pressure taken at -1. The location of the cavitation region agrees well in both methods. (Image source [8])

an elliptical partial differential equation in the full fluid zone, and hyperbolic otherwise as only the Couette component was at play. The discretisation of the θ^* dependent Reynolds equation consisted of central differences for any point in the full fluid film and upwind differences for the cavitated region. Also, they argued that compressibility effects should not be neglected in the cavitated region, as was done by Elrod. For this, they introduced an artificial viscosity function in the shear flow equation. The authors compared their results with the initial Elrod algorithm and found satisfactory agreement between pressure profiles of journal bearings (see Fig. 2.11). However, in order to use Elrod's algorithm a rather empirical adjustments of the bulk modulus must be made. Vijayaraghavan's et. al. merely aimed at refining the algorithm, and for the sake of comparison they have used the data already provided by Elrod, and no discussion regarding the value of β_l was made.

Brewe [7] focused on simulating cavitation in both steady and dynamically loaded journal bearings by using the conservative algorithm of Elrod. He obtained excellent agreement with experimental data given by Jakobsson and Floberg [58] for steady cavitation, but his results showed a significant discrepancy, partially attributed to thermal effects, when compared with the ones of Jacobson and Hamrock [59]. Also, the authors mention that at eccentricities as high as 0.98, numerical instabilities were encountered. In a more recent study, Fesanghary et. al. [60] presented a new switching function for

the Elrod's algorithm, which increases the convergence rate with up to 61% and is less prone to instabilities.

The multitude of models that applied the JFO theory in Elrod's algorithm (for a more extensive list of references see [61]), rendered this type of approach the state-of-the-art in the simulation of cavitation in hydrodynamic bearings, regardless of the reported numerical instabilities. The algorithm was mostly applied to grooved journal bearings, slider bearings or textured bearings, and less to the case of porous journal bearings. The work of Meurisse et. al. [9] is however, a good example of the latter application. They applied the mass conservative approach assuming that there is no side leakage and no air entrainment into the bearing and calculated the oil exchange between the gap, porous matrix and the surrounding environment.

2.4 Thermo-physical properties of adopted lubricants

Choosing the right type of lubricant for the specific tribologic application can be a crucial task. One must take into account various factors including operation environment, lifetime, and the load-carrying capacity. Apart from the role in reducing friction and wear, in some cases lubricants are also required to prevent over-heating of the neighbouring surfaces or to prevent corrosion. All these issues have been thoroughly investigated in research, with the final scope of tailoring novel lubricants with outstanding tribological properties.

Most lubrication oils are composed of a base oil and a multitude of additives that enhance the specific desired properties. They can be grouped into various categories like liquids, semi-solids, solids, gaseous or based on the origin of the substance used, i.e. renewable or non-renewable [62]. Moreover, their degree of biodegradability is also taken into account, such that a lower impact on the environment can be achieved. Most common properties of lubricants are viscosity, viscosity-temperature behaviour, thermal stability, lubricity and volatility.

In 2001, ionic liquids (ILs) were proposed as viable candidates for lubrication applications. Ionic liquids are organic salts whose melting temperature is below 100°C. Tests have shown that they exhibit an interesting low wear rate when used as lubricants. Additionally, their properties can be chemically altered and modelled as to adapt to specific application necessities [63], [64]. Apart from this, they exhibit good thermal stability and a weak dependence of the viscosity on temperature, such that relations like Eq. 2.6 can predict the viscosity change satisfactorily. It is known that in journal bearings the vapour pressure of the lubricant plays an important role in the development of cavitation. In this respect, ionic liquids showed interesting attributes: very low vapour pressures (which in addition means a correspondingly reduced tendency to evaporate over time). At room temperature, the vapour pressures of ILs are almost impossible to be detected. For example, Zaitsau [65] recorded vapour pressures in the range of

10^{-2} – 10^{-1} Pa at 450–530K under standard conditions, i.e. rather moderate lubrication pressures These are specified below by the adopted values of the reference pressure (\tilde{p}_{ref}).

These promising features lead to an increased interest of industry into choosing ILs as prospective lubricants, but also the present work into the investigation of their possible applications. Apart from the advantageous thermo-physical properties, ILs appear to be suitable for the specific operating conditions of porous journal bearing. Here the most simple ones are used though:

- Newtonian rheology;
- $\tilde{T} = const$ and therefore $\tilde{\eta} = const$ across gap justified by relatively weak dissipation at moderate shaft speeds due to
- loads/pressures relatively moderate.

Analysis of self-lubricated systems with a porous reservoir

In this chapter we present the premises of the novel cavitation model that we employ in the present work. We note that the flow in the journal bearing exhibits two forms of appearance, where the interaction between the two associated regions preserves the continuity of mass. In the current configuration, cavitation develops as a stable two-phase regime and expands in both axial and circumferential direction. Our main concern is with the determination of the gap pressure, including the formation of cavitation, under various load regimes. The number of input independent variables in the resulting system is rather large, and therefore, dimensional analysis is used to reduce the system to an equivalent, more economical form. In this way functional relationships between input variables are derived, which serve to systematically analyse the system behaviour under various conditions. Finally, we present one application of the dimensional analysis: the study of a thin bearing of infinite permeability, as a limiting case of the standard configuration, for which the two initial flow regions decouple.

3.1 Motivation

Since their introduction in industry as self-lubricating mechanisms for supporting load, the demand for porous journal bearings has increased greatly. The experimental and theoretical studies presented in Ch. 2 are merely a small fraction of the available literature, yet are considered the pioneering works in the field. Nonetheless, a thorough self-consistent analysis of the arising lubrication problem is still not available, and therefore, the need of in-depth fundamental research is apparent. The present work aims at refining some of the scientific efforts made so far, particularly to avoid issues arising

from non-rational modelling of the involved physics and to bring in a new efficient numerical strategy that copes with cavitation of an incompressible lubricant for porous journal bearings.

3.2 Adopted cavitation model

Porous journal bearings are usually encapsulated in solid metal casings, which means that lubricant cannot leak from the sinter to the exterior, and that entrainment of air from the outside is not possible. Under these conditions, we can safely assume the complete insulation of the exterior surfaces of the bearing. Moreover, the oil rings that usually form at the edges of the lubrication gap prevent the air to enter into it. These specific conditions point to the occurrence of a cavitation mechanism as described in Sect. 2.3 (iii), and referred to as vaporous cavitation. Here cavitation initiates when the lubricant pressure drops from \tilde{p} down to the respective vapour pressure, \tilde{p}_c . The cavitation region then comprises a two-phase homogeneous mixture of oil and vapour of varying concentrations, where no individual bubbles can be detected. By neglecting any dissolved gas in the liquid, the pressure is equal to \tilde{p}_c all throughout the cavitation area. Curvature effects like the Gibbs-Thomson variation of the vapour pressure across a curved surface are also neglected. In addition, we assume that the two surfaces adjacent to the gap take on the same temperature, and that the lubricant temperature increase due to viscous dissipation is negligible small.

In this formulation of the cavitation mechanism we deal with a lubricant undergoing an isothermal process of change of state, from an one-phase regime (fully liquid) to a two-phase regime (cavitation, mixture). The first regime is characterized by a uniform density $\tilde{\rho}_l$ incompressible liquid, while the two-phase regime contains parts liquid of density $\tilde{\rho}_l$ and parts vapour described by the density $\tilde{\rho}_v$. Here we define the lubricant saturation as:

$$S = \frac{\tilde{\rho}_m}{\tilde{\rho}_l}, \quad (3.1)$$

which achieves a minimum value if the mixture density $\tilde{\rho}_m$ contains only vapour of $\tilde{\rho}_v$. However, this limiting case is not considered, as we definitely disregard complete vaporization. In fact, in (porous) journal bearings preference is given to lubricants with low tendency to evaporate, which encourages the formulation of the cavitation mechanism addressed in Sect. 2.3 (vaporization), and accordingly, in this employed model. It results that S can only take positive values below 1 and satisfies the relations for the mass and volumetric compositions of a fluid particle:

$$S = \alpha_l/x_l = \alpha_l + (\tilde{\rho}_v/\tilde{\rho}_l)(1 - \alpha_l) = [x_l + (\tilde{\rho}_l/\tilde{\rho}_v)(1 - x_l)]^{-1}, \quad (3.2)$$

with α_l, x_l denoting the volumetric and mass fractions of the liquid phase.

The specific surface topography of porous journal bearings described by a random distribution of small and large pores is treated here in a homogenized manner. This means that no microscopic surface effects are considered, and that the sinter pore distribution is incorporated by means of the permeability tensor Φ . Assuming that the sinter material is orthotropic in the radial, circumferential and axial directions of the bearing, Φ is a symmetric tensor represented by three diagonal components $\Phi(r, \theta, z)$. The lubricant flow is then governed by the material bulk properties, which implies the classical no-slip condition at the stationary surface of the gap. Applying a micro-slip at the porous surface appears to have very small effects on the lubrication pressure, as studied in [66]. We neglect any elastic deflection of the bush, as porous journal bearings commonly operate under low to moderate loads and adopt the fundamental assumptions of the Reynolds lubrication theory (see Sect.2.1.2). Hence, the lubricant pressure in the gap (denoted by \tilde{p}_r from now on) is obtained by a modification of the Reynolds equation, and relies on the incorporation of an artificial relationship between the introduced saturation S and the lubricant pressure \tilde{p}_r . In particular, $\tilde{p}_r - S$ is controlled by a so-called compressibility factor β in order to insure smooth transition from the one-phase to the two-phase regime. This process is reproduced on the phase diagram in Fig. 3.1. The arrow attached to the solid curve describes the resultant isothermal change of state of the lubricant passing the onset of vaporization, $\tilde{p}_r = \tilde{p}_r(\tilde{\rho})$. Film reformation occurs at a previously unknown location and is characterized by the increase of S to 1. The lubricant pressure is a function of the varying lubricant density but inside the two-phase region it remains at a constant level given by the cavitation pressure, \tilde{p}_c .

Finally, in what concerns the fluid flow through the sinter matrix, we exclude the extension of the cavitation region beyond the limits of the lubrication gap. Essentially, the sinter matrix is cavitation-free, and the governing pressure \tilde{p}_d satisfies:

$$\tilde{p}_d > \tilde{p}_c, \quad (3.3)$$

a specification adopted in [9] and proven in [46].

3.3 Geometry of the investigated system

The specific way of operation of porous journal bearings was explained in Ch. 2.4, however let us revisit in more detail the quantities involved. The investigated system is given in Fig. 3.2, where \tilde{r} , θ and \tilde{z} denote the radial, circumferential and axial coordinates. The seat consists of a hollow cylinder of inner radius \tilde{r}_b , a wall thickness $\tilde{\lambda}$ and a length \tilde{l} . The porous seat is characterized by the porosity $\tilde{\phi}$ and a reference permeability $\tilde{\Phi}_{ref}$. Inside the bearing a shaft of radius \tilde{r}_s rotates with $\tilde{\omega}$ around the circumferential direction θ . The radial clearance between the seat and the shaft defined as $\tilde{c} = \tilde{r}_b - \tilde{r}_s$ is assumed to be entirely filled with a lubricant of viscosity $\tilde{\eta}$ and density $\tilde{\rho}$.

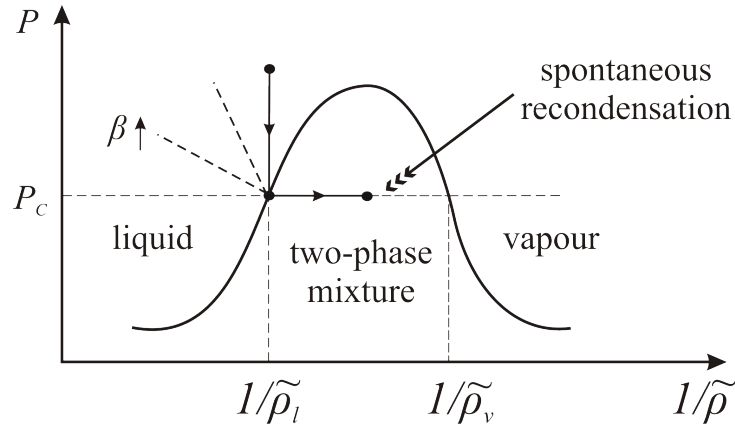


Figure 3.1: Phase diagram

When the load \tilde{w} is applied on the bearing and the shaft is rotating, a convergent/divergent gap will form, creating the “wedge” effect that lifts and displaces the shaft eccentrically (with a distance \tilde{e}) from the center of the bearing. In the loaded part of the bearing the hydrodynamic pressure, \tilde{p}_r , lower than the pressure in the unloaded part, carries the load \tilde{w} applied on the shaft. The pressure difference between the two areas causes the lubricant to circulate through the pores of the seat, and ultimately to provide with the necessary amount of lubricant for the build-up of the fluid film in the gap.

As a result of the eccentric displacement of the journal, the thickness of the fluid film is not constant, but varies along θ and is dependent on \tilde{e} . As a first assumption for the theoretical model, any axial tilt of the shaft is neglected such that Eq. 2.8 applies for the film thickness \tilde{h} and the maximum value that \tilde{h} can take is the available clearance \tilde{c} .

The location of the journal is measured by the attitude angle ψ , which is the angle formed by a line passing through the center of both the bearing and shaft, and the line describing the direction of the applied load. ψ is a function of the speed of rotation and of the load. Finally, we consider that the system is symmetric with respect to the axial coordinate, such that only half of the bearing is enough for the pressure calculation.

The configuration described herein summarizes all the parameters that play a role in the lubrication process of a porous journal bearing. The physical assumptions that formulate the specific conditions for cavitation formation in the chosen geometry will be presented in the following section.

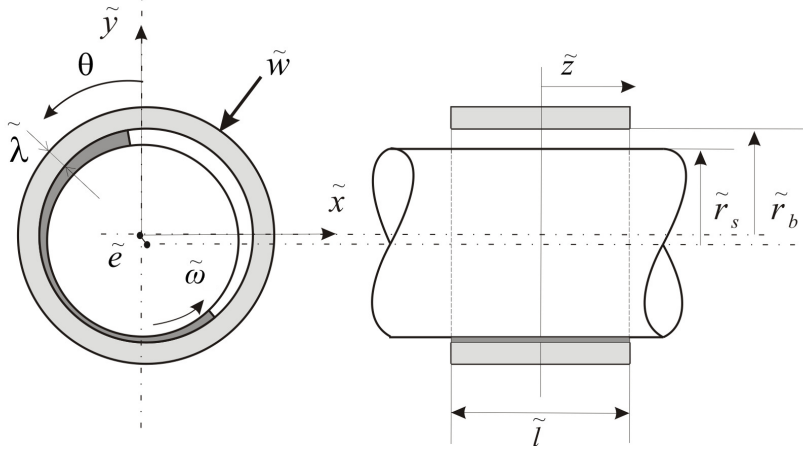


Figure 3.2: Journal bearing: notations used for the geometrical quantities

3.4 Dimensional analysis

The problem presented so far involves a high number of input variables, as a total of 9 physical quantities determines the complete lubrication problem. The pressures in the two lubrication regions, film gap \tilde{p}_r and sinter matrix, \tilde{p}_d , depend on:

$$[\tilde{p}_r, \tilde{p}_d] = [f_r, f_d](\tilde{c}, \tilde{r}_b, \tilde{l}, \tilde{\lambda}, \tilde{\Phi}_{ref}, \tilde{\omega}, \tilde{e}, \tilde{\eta}, \tilde{p}_c), \quad (3.4)$$

with f_r, f_d to be obtained by testing. It is therefore more advantageous to reduce the number of input variables to a smaller number of non-dimensional parameters, which can ease the subsequent numerical/theoretical investigations. In dimensional analysis, one method to do so is to apply the Buckingham- π theorem [67]. This states that for n number of input dimensional variables, one can extract $p = n - m$ dimensionless quantities denoted $\Pi_k, k = 1 \dots p$, where m is the rank of the dimensional matrix. If the complete set of dimensional quantities has been correctly identified, the solution of the system is of the form:

$$\Pi = f(\Pi_1, \Pi_2, \dots \Pi_p). \quad (3.5)$$

The choice of independent variable is not unique, as the Buckingham π theorem yields merely the number of the dimensionless quantities governing the equation, and not necessarily their explicit form.

In our case $n = 9$ and the resulting dimensional matrix expressed via the conventional base dimensions $[L, T, M]$ -[length, time, inertial mass] is of the form:

$$\mathbf{D} = \begin{matrix} & \tilde{c} & \tilde{r}_b & \tilde{l} & \tilde{\lambda} & \tilde{\Phi}_{ref} & \tilde{\omega} & \tilde{e} & \tilde{\eta} & \tilde{p}_c \\ \begin{matrix} L \\ T \\ M \end{matrix} & \begin{pmatrix} 1 & 1 & 1 & 1 & 2 & 0 & 1 & -1 & -1 \\ 0 & \dots & & & 0 & -1 & 0 & -1 & -2 \\ 0 & \dots & & & 0 & 0 & 0 & 1 & 1 \end{pmatrix} \end{matrix} \quad (3.6)$$

The rank of \mathbf{D} yields $m = 3$, such that the system is reduced to a number $n - m = 6$ non dimensional parameters, given in Tab. 3.1. \tilde{p}_r is defined as the usual reference pressure and is the sole quantity that entails the lubricant specific characteristic viscosity $\tilde{\eta}$ and the operation shaft speed $\tilde{\omega}$. K is a function of the surface permeability $\tilde{\Phi}_{ref}$ and highly sensitive to the gap radial clearance \tilde{c} (cubic inverse proportional). The choice of the squared length \tilde{c}^3/\tilde{r}_s rather than $\tilde{\lambda}^2$ in K reflects the strong coupling between the two flow regions. Γ and Λ are chosen to represent aspect ratios specific to the chosen geometry. Although a dependent variable, the film thickness can be expressed in non-dimensional form by the leading order relationship

$$H(\theta) = \tilde{h}/\tilde{c} = 1 + \varepsilon \cos\theta. \quad (3.7)$$

To complete the non-dimensionalisation of the system, the radial and axial coordinates \tilde{r}, \tilde{z} are parametrized by $r = \tilde{r}/\tilde{r}_s$ and $z = \tilde{l}/2$. The latter respects the assumption made in Sect. 3.3 that the considered problem is symmetric with respect to the \tilde{z} -axis. Finally, when \tilde{p}_r, \tilde{p}_d are made non-dimensional with p_{ref} , Eq. 3.4 is replaced by

\tilde{p}_r	$6 \tilde{\omega} \tilde{\eta} \tilde{r}_s / \tilde{c}^2$	reference pressure
ε	\tilde{e}/\tilde{c}	eccentricity ratio
Γ	$(2 \tilde{r}_s / \tilde{l})^2$	aspect ratio
Λ	$\tilde{\lambda} / \tilde{r}_s$	thickness ratio
K	$12 \tilde{\Phi}_{ref} \tilde{r}_s / \tilde{c}^3$	permeability parameter
P_C	$\tilde{p}_c / \tilde{p}_{ref}$	cavitation pressure
So	$\tilde{\omega} / (\tilde{p}_{ref} \tilde{r}_s \tilde{l})$	Sommerfeld number

Table 3.1: Reference pressure and non-dimensional groups

$$[P_R, P_D] = [F_R, F_D](\varepsilon, \Gamma, K, \Lambda, P_C), \quad (3.8)$$

The advantage of Eq. 3.8 lies in the possibility to systematically vary in numerical calculations the 5 non-dimensional parameters and asses the limitations and specific behaviour that they enforce. This is studied thoroughly in Ch. 4.5.

3.5 Governing equations and boundary conditions

The classical theory developed by O. Reynolds in 1886 (see Sect. 2.1.2) is the most rigorous approach for the calculation of the fluid pressure in thin fluid film gaps. We will modify the standard Reynolds equation in order to accommodate the formation of cavitation according to the mechanism described above. Regarding the second flow

region, namely the sinter matrix, Darcy's classical law will be applied, as its derivations (Brinkman, Forchheimer) are rather phenomenological. The coupling of these two equations yields a closed system of equations describing the posed lubrication problem which returns the pressure distribution through the system. The steps of this approach are explained in the following paragraphs, where the non-dimensional quantities obtained in Sect. 3.4 are used.

The flow through the lubrication gap The modified Reynolds equation is written in non-dimensional form as:

$$\frac{\partial}{\partial \theta} \left(H^3 \frac{\partial P_R}{\partial \theta} \right) + \Gamma \frac{\partial}{\partial z} \left(H^3 \frac{\partial P_R}{\partial z} \right) = \frac{\partial(HS)}{\partial \theta} - v_{D,r}. \quad (3.9)$$

The terms on the left hand side of Eq. 3.9 represent the known Poiseuille contribution to the gap flow while the first term on the right hand side represents the Couette flow. The rightmost term in Eq. 3.9 accounts for the inflow from the porous seat, with the negative sign giving the flow direction. In the two-phase regime Eq. 3.9 is governed solely by the right hand side, as the right hand terms completely vanish. This requires a smooth $S - P_R$ relationship so as to overcome the sudden transition. The imposed empirical relation $S = S(P_R)$ entails the switching between the one- and two-phase flow regime and the limit of perfectly incompressible flow behaviour is reached when:

$$S = S(P_R) : \begin{cases} S \equiv 1, & P_R > P_C, \\ 0 < S < 1, & P_R \equiv P_C. \end{cases} \quad (3.10)$$

Additionally, the pressure is bounded from below by P_C such that $P_R > P_C$. This formulation is more general than the Elrod's original algorithm, as it does not rely on the choice of a fluid property (bulk modulus), and no additional variable is introduced. The appropriate boundary conditions for Eq. 3.9 are given by periodicity in θ , symmetry with respect to $z = 0$, and the prescription of the ambient pressure at the edge of the lubrication gap $z = 1$:

$$\begin{aligned} P_R|_{\theta=0} &= P_R|_{\theta=2\pi}, & \frac{\partial P_R}{\partial \theta}|_{\theta=0} &= \frac{\partial P_R}{\partial \theta}|_{\theta=2\pi}, \\ \frac{\partial P_R}{\partial z}|_{z=0} &= 0, & P_R|_{z=1} &= 0. \end{aligned} \quad (3.11)$$

The flow through the sinter matrix The second flow region is governed by the Darcy's law (Eq. 2.20). Applying the law of mass conservation for an incompressible fluid for the Darcy flux q :

$$\nabla \tilde{p} \cdot q = 0, \quad (3.12)$$

it results that the flow through the sinter matrix is described by the Laplace's equation

$$\Delta \tilde{p} = 0. \quad (3.13)$$

Assuming that the material permeability is orthotropic, Eq. 3.13 is written in cylindrical coordinates as

$$\frac{1}{r} \frac{\partial}{\partial r} \left(r \Phi_r \frac{\partial P_D}{\partial r} \right) + \frac{1}{r^2} \frac{\partial}{\partial \theta} \left(\Phi_\theta \frac{\partial P_D}{\partial \theta} \right) + \Gamma \frac{\partial}{\partial z} \left(\Phi_z \frac{\partial P_D}{\partial z} \right) = 0. \quad (3.14)$$

Here $\Phi_{r,\theta,z}(r, \theta, z)$ are the components of the permeability tensor Φ , when made non-dimensional with an appropriate reference value $\tilde{\Phi}_{ref}$. In the case of homogeneous and isotropic permeability, $\Phi_{r,\theta,z}(r, \theta, z)$ are identified with unity. Also, P_D is a function of the three spatial coordinates, $P_D(r, \theta, z)$ and is constrained by the boundary conditions of periodicity in θ , symmetry in axial direction z , and external insulation:

$$\begin{aligned} P_D \Big|_{\theta=0} &= P_D \Big|_{\theta=2\pi}, \\ \frac{\partial P_D}{\partial \theta} \Big|_{\theta=0} &= \frac{\partial P_D}{\partial \theta} \Big|_{\theta=2\pi}, \\ \frac{\partial P_D}{\partial z} \Big|_{z=0} &= \frac{\partial P_D}{\partial z} \Big|_{z=1} = \frac{\partial P_D}{\partial r} \Big|_{r=1+\Lambda} = 0. \end{aligned} \quad (3.15)$$

We impose that at the boundary between the fluid film and the porous seat the two pressures are equal:

$$r = 1 : P_R = P_D, \quad (3.16)$$

a condition which is valid as long as the characteristic scale of the porous surface (e.g. pore diameter or distance between pores) is sufficiently small when compared to the gap height, which otherwise would require a homogenization process. The final coupling between the two regions is given by:

$$v_{D,r} = K \frac{\partial P_D}{\partial r}. \quad (3.17)$$

The boundaries of the cavitation region are not known in advance, rendering the lubrication problem a free-surface problem. The general approach to this issue (as seen in Sect. 2.3) is associating specific boundary conditions to the Reynolds equation. The very basic Gumbel condition, although reported to deliver deviations for the load capacity of about 15% ([41]) as compared to more refined models, is clearly not a solution as it violates the continuity of mass. We therefore consider it necessary to impose a condition which requires a zero net mass flux across the cavitation interface, like Eq. 2.25, applied by Floberg in his analysis [53]. On the other hand, in the case of a vaporous cavitation, as the one adopted in this work, the earlier Reynolds boundary condition of

vanishing pressure gradient (Eq. 2.24) applies only at the stage of inception, and not at film reformation. The reason is because the two governing quantities, the pressure and saturation, terminate in a discontinuity, as a result of the anticipated spontaneous recondensation. This is why the termination of the cavitation area should definitely be accompanied by a more rational condition to support the associated jump. These being said, the system of equations formed by Eqs. 3.9 and Eq. 3.14 is supplemented with the following conditions.

$$\begin{aligned}
 \text{Onset of cavitation:} \quad & P_R = P_C, \quad \frac{\partial P_R}{\partial \theta} = \frac{\partial P_R}{\partial z} = 0; \\
 \text{recondensation:} \quad & P_R = P_C, \quad \frac{\partial P_R}{\partial \theta} - \Gamma \frac{\partial P_R}{\partial z} \frac{d\theta}{dz} = \frac{1 - S}{H^2},
 \end{aligned} \tag{3.18}$$

which is essentially the JFO condition.

Notwithstanding its simplicity, the presented model brings on the following novel points:

- the inclusion of vaporous cavitation by considering the cavitated region a homogeneous two-phase mixture;
- a smooth transition between the fully liquid and cavitated regime via an advantageous empirical relation $S(P_R)$;
- a lower bounding of the lubrication pressure by the cavitation pressure $P_R \geq P_C$;
- an inevitable spontaneous recondensation in steady-state porous bearings, due to their periodic geometry.

3.6 The case of highly permeable seat $K \gg 1$

Using the dimensional analysis for the reduction of the original number of inputs to a smaller number of governing parameters brings on an additional advantage. It eases the identification of limiting processes, which can be thoroughly studied by considering the marginal values for the non-dimensional inputs. For example, very narrow or long bearings can be studied by taking the aspect ratio $\Gamma \gg 1$ or $\Gamma \ll 1$, respectively. However, more interesting situations occur when the two flow regions of the bearing decouple, and a single equation is sufficient to describe the flow. This is the case when one assumes a bearing having a very narrow (thin) but at the same time highly permeable seat. The first prerequisite implies that $\Lambda \ll 1$, and, furthermore very weak variations of the permeability components across the thickness of the seat, while the second assumption renders $K \gg 1$. Let

$$\hat{K} = K\Lambda = O(1) \tag{3.19}$$

be the quantity which characterizes this limiting process. The original pressure components P_R and P_D are now described by the approximations:

$$P_R \sim \hat{P}_0(\theta, z) + o(1) \quad (3.20)$$

$$P_D \sim \hat{P}_0(\theta, z) + \Lambda^2 \hat{P}_2(\hat{r}, \theta, z) + O(\Lambda^3) \quad (3.21)$$

with $\hat{r} = (r - 1)/\Lambda$. The original Reynolds Eq. 3.9 now becomes

$$\frac{\partial}{\partial \theta} \left[(H^3 + \hat{K} \Phi_\theta) \frac{\partial \hat{P}}{\partial \theta} \right] + \Gamma \frac{\partial}{\partial z} \left[(H^3 + \hat{K} \Phi_z) \frac{\partial \hat{P}}{\partial z} \right] = \frac{\partial(HS)}{\partial \theta}. \quad (3.22)$$

The problem is closed by adopting the same specifications as in Eq. 3.10. Herein \hat{P} depends on the azimuthal angle θ and symmetrically on the axial direction z , non-dimensional with $\tilde{l}/2$, of the gap, apart from the remaining governing parameters Γ , ε , \hat{K} , and P_C . Furthermore, $H := \tilde{h}/\tilde{c}$ is the non-dimensional film thickness, $\Phi_{\theta,z}$ denotes the non-dimensional permeability components of the sinter matrix in the azimuthal and the axial direction, respectively, when $\tilde{\Phi}_{ref}$ is considered as a reference, and S represents the lubricant saturation, i.e., the ratio between the density of the two-phase mixture and the one of the liquid phase. In contrast to the full simulations, here insulation and vanishing pressure at the edge of the bearing cannot be satisfied simultaneously since this would require a separate treatment of square regions in the seat close to $z = 1$. As a result, here the bearing allows for a local oil flux through its edges, but still giving zero net flux.

A related problem was studied by Cameron [36], neglecting cavitation and assuming an isotropic and homogeneous permeability, yet yielding an analytical solution for infinitely long/short bearings. Nevertheless, the thus reduced problem, Eq. 3.22, not only drastically eases the systematic investigation of the bearing operation, but allows correct qualitative insight.

Numerical study

In the first part of this chapter we present the numerical discretisation scheme and the algorithm used for solving the theoretical model. This is achieved by discretising the equations using second-order accuracy finite differences and iterating for converged solutions. We then search for the most suitable numerical parameters which yield satisfactory numerical results. Specifically, the parametrization of the $P_R - S$ relationship and the admissible values of the compressibility parameter β provide with stable and fast converging solutions. Once these parameters are fixed, we run calculations for a standard bearing configuration: there, typical pressure and saturation distributions show the extent of the cavitation region and how this is affected by the variation of the eccentricity ratio. The non dimensional load, friction coefficient and attitude angle are part of the solution and are given as functions of K and ε . The analysis of the results is completed by an extended parameter database, which not only gives preliminary indications on the range of admissible input parameters to yield converged solutions, but also serves to the extraction of an empirical relation between the non-dimensional parameters, to be used further on for the experimental validation of the model. Finally, results for the case of highly permeable seat described in Sect. 3.6 are presented.

4.1 Discretisation and iterative scheme

The physical model described by Eqs. 3.9–3.14 requires conservation of mass at the interface between the liquid and the two-phase mixture. This is satisfied when a conservative finite-differences discretisation is employed. The system of equations can be written in matrix form as

$$\begin{aligned} A_R \cdot S &= B_R, \\ A_D \cdot P_D &= B_D, \end{aligned} \tag{4.1}$$

so that the dependent variables in the Reynolds and Darcy's equations are S and P_D , respectively. All discrete points are calculated on an orthogonal mesh which contains uniformly distributed grid points, but with variable number of nodes in the orthogonal directions r, θ, z . The grid spacing between nodes are $\Delta\theta$ and Δz for θ and z , respectively. The common notations North, South, East, West (N, S, E, W) are used for the r, z directions, supplemented with Front, Back (F, B) points for the θ direction. A typical grid stencil for the discretisation of the two-dimensional Reynolds equation (in $\theta - z$) is depicted in Fig. 4.1). Upper-case symbols denote values located at the actual grid point while lower-case points are evaluated half-way the grid points, $\Delta\theta/2, \Delta z/2$.

The employed discretisation scheme for both Reynolds and Darcy equation is a combination of central differences—for the inner grid points—and forward/backward differences—required at the boundaries—of second order accuracy. The discretised terms are explained below.

Reynold's equation For the equation pertaining to the lubricant gap we first perform a linearisation of the initial equation, such that the dependent variable is the lubricant saturation, S . To this end, if we consider that superscripts indicate the i -th iterated discrete approximation of S and P_R , a change of variable and pressure approximation yields the linearisation of P_R :

$$\left. \begin{aligned} \frac{\partial P_R}{\partial \theta} &= \frac{\partial P_R}{\partial S} \frac{\partial S}{\partial \theta} \\ \frac{\partial P_R}{\partial z} &= \frac{\partial P_R}{\partial S} \frac{\partial S}{\partial z} \\ P_R^{i+1} &= P_R^i + \Delta P_R \end{aligned} \right\} \Rightarrow P_R^{i+1} = P_R^i + \frac{\partial P_R^i}{\partial S^i} \Delta S. \quad (4.2)$$

The derivatives in θ and z of the pressure P_R according to Eq. 4.2 are

$$\frac{\partial P_R^{i+1}}{\partial \theta} = \frac{\partial P_R^i}{\partial S^i} \frac{\partial S^{i+1}}{\partial \theta} + \frac{\partial^2 P_R^i}{\partial S^{i2}} \frac{\partial S^i}{\partial \theta} (S^{i+1} - S^i), \quad (4.3)$$

$$\frac{\partial P_R^{i+1}}{\partial z} = \frac{\partial P_R^i}{\partial S^i} \frac{\partial S^{i+1}}{\partial z} + \frac{\partial^2 P_R^i}{\partial S^{i2}} \frac{\partial S^i}{\partial z} (S^{i+1} - S^i). \quad (4.4)$$

These new terms are now introduced in the initial Reynolds equation (3.9), so as to yield the sought linearisation:

$$\begin{aligned} & \frac{\partial}{\partial \theta} \left\{ H^3 \left[\frac{\partial P_R^i}{\partial S^i} \frac{\partial S^{i+1}}{\partial \theta} + \frac{\partial^2 P_R^i}{\partial S^{i2}} \frac{\partial S^i}{\partial \theta} (S^{i+1} - S^i) \right] \right\} + \\ + \Gamma & \frac{\partial}{\partial z} \left\{ H^3 \left[\frac{\partial P_R^i}{\partial S^i} \frac{\partial S^{i+1}}{\partial z} + \frac{\partial^2 P_R^i}{\partial S^{i2}} \frac{\partial S^i}{\partial z} (S^{i+1} - S^i) \right] \right\} = \\ & = \frac{\partial(S^{i+1}H)}{\partial \theta} - K \frac{\partial P_D}{\partial r}, \end{aligned} \quad (4.5)$$

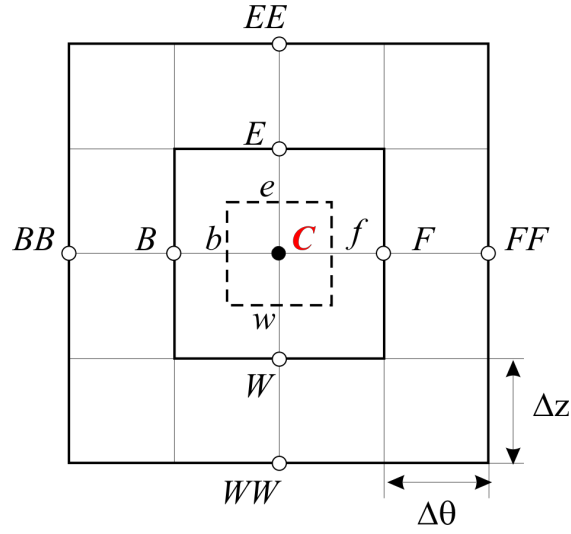


Figure 4.1: Grid of the mapped coordinates: single index one grid point away, double indexes two grid points away, lower-case indexes at half grid point; Eq. 3.9 and 3.14 to be satisfied at center point C

which can be written in a more compact form when the local (conservative) coefficients of S are denoted by R_θ , $R_{\theta\theta}$, R_z and R_{zz} :

$$\begin{aligned} R_\theta &= H^3 \frac{\partial P_R^i}{\partial S^i}, & R_{\theta\theta} &= H^3 \frac{\partial^2 P_R^i}{\partial S^{i^2}} \frac{\partial S^i}{\partial \theta}, \\ R_z &= \Gamma H^3 \frac{\partial P_R^i}{\partial S^i}, & R_{zz} &= \Gamma H^3 \frac{\partial^2 P_R^i}{\partial S^{i^2}} \frac{\partial S^i}{\partial z}. \end{aligned} \quad (4.6)$$

Finally we obtain the linearised equation that is to be discretised:

$$\begin{aligned} \frac{\partial}{\partial \theta} \left(R_\theta \frac{\partial S^{i+1}}{\partial \theta} + R_{\theta\theta} S^{i+1} - S^{i+1} H \right) + \frac{\partial}{\partial z} \left(R_z \frac{\partial S^{i+1}}{\partial z} + R_{zz} S^{i+1} \right) = \\ -K \frac{\partial P_D}{\partial r} + \frac{\partial}{\partial \theta} \left(R_{\theta\theta} S^i \right) + \frac{\partial}{\partial z} \left(R_{zz} S^i \right). \end{aligned} \quad (4.7)$$

Let us consider the first equivalent Poiseuille term in θ -direction of Eq. 4.7 and neglect for the time being the iteration indices $i, i+1$. The outer differential is discretised by a central-differences scheme:

$$\frac{\partial}{\partial \theta} \left(R_\theta \frac{\partial S}{\partial \theta} \right) = \frac{\left(R_\theta \frac{\partial S}{\partial \theta} \right)^f - \left(R_\theta \frac{\partial S}{\partial \theta} \right)^b}{\Delta \theta}. \quad (4.8)$$

Employing once more a central discretisation, the inner differentials are developed as follows:

$$\left(R_\theta \frac{\partial S}{\partial \theta}\right)^f = R_\theta^f \frac{S^F - S^C}{\Delta \theta} \quad \text{and} \quad \left(R_\theta \frac{\partial S}{\partial \theta}\right)^b = R_\theta^b \frac{S^C - S^B}{\Delta \theta}. \quad (4.9)$$

The coefficients R_θ^f and R_θ^b are evaluated at intermediate locations (half grid points), by averaging:

$$R_\theta^f = \frac{1}{2} (R_\theta^c + R_\theta^f), \quad R_\theta^b = \frac{1}{2} (R_\theta^c + R_\theta^b). \quad (4.10)$$

Combining 4.8 and 4.9 gives:

$$\frac{\partial}{\partial \theta} \left(R_\theta \frac{\partial S}{\partial \theta}\right) = \frac{R_\theta^f S^F - (R_\theta^f + R_\theta^b) S^C + R_\theta^b S^B}{\Delta \theta^2}. \quad (4.11)$$

In a similar way we obtain the discretisation of the equivalent "Poiseuille term" in z direction:

$$\frac{\partial}{\partial z} \left(R_z \frac{\partial S}{\partial z}\right) = \frac{R_z^f S^F - (R_z^f + R_z^b) S^C + R_z^b S^B}{\Delta z^2}. \quad (4.12)$$

The second term in 4.7 is discretised using a direct central-differences scheme:

$$\frac{\partial}{\partial \theta} \left(R_{\theta\theta} S\right) = \frac{R_{\theta\theta}^F S^F - R_{\theta\theta}^B S^B}{\Delta \theta}, \quad (4.13)$$

and in the same way for the z -direction:

$$\frac{\partial}{\partial z} \left(R_{zz} S\right) = \frac{R_{zz}^F S^F - R_{zz}^B S^B}{\Delta z}. \quad (4.14)$$

In order to achieve a smooth transition between the original conservative scheme and the advective operator on the right hand side of Eq. 3.9, we employ a backward differences scheme for the wedge term $\partial_\theta(HS)$. This insures that any possible instabilities like grid oscillations are avoided:

$$\frac{\partial}{\partial \theta} (-SH) = \frac{S^B H^B - S^C H^C}{\Delta \theta}. \quad (4.15)$$

Summarizing the discretised terms one can identify the coefficients of the saturation S :

$$\begin{aligned} (\mathbf{S}^{i+1})^F : A_R^F &= \frac{1}{\Delta \theta^2} R_\theta^f + \frac{1}{2\Delta \theta} (R_{\theta\theta}^F), \\ (\mathbf{S}^{i+1})^B : A_R^B &= \frac{1}{\Delta \theta^2} R_\theta^b - \frac{1}{2\Delta \theta} (R_{\theta\theta}^B + 2H^B), \\ (\mathbf{S}^{i+1})^E : A_R^E &= \frac{1}{\Delta z^2} R_z^e + \frac{1}{2\Delta z} R_{zz}^E, \\ (\mathbf{S}^{i+1})^W : A_R^W &= \frac{1}{\Delta z^2} R_z^w - \frac{1}{2\Delta z} R_{zz}^W, \\ (\mathbf{S}^{i+1})^C : A_R^C &= (-1) \left[\frac{1}{\Delta \theta^2} (R_\theta^f + R_\theta^b) + \frac{1}{\Delta \theta} H^C + \frac{1}{\Delta z^2} (R_z^e + R_z^w) \right], \end{aligned} \quad (4.16)$$

while the right hand side is

$$B_R = -K \frac{\partial P_D}{\partial r} + \frac{\partial}{\partial \theta} (R_{\theta\theta} S_i) + \frac{\partial}{\partial z} (R_{zz} S^i) \quad (4.17)$$

Given the boundary conditions from Sect. 3.5 we now finalize the discrete system by numerically implementing the boundary conditions. Let $j = 1 \dots J$ and $k = 1 \dots K$ denote the domain bounded by $[0, 2\pi]$ in θ and $[0, 1]$ in z , be the corresponding grid sizes. Ambient pressure at the edge of the bearing, $P_R|_{z=1} = 0$ becomes in terms of S

$$S_{j,K} = 1 - \frac{P_C}{2\beta}. \quad (4.18)$$

The symmetry line at $z = 0 (k = 1)$ is prescribed by setting the second order accuracy forward difference of S to 0:

$$-3S_{j,1} + 4S_{j,2} - S_{j,3} = 0. \quad (4.19)$$

Periodicity in θ is equally valid for the lubricant saturation, S , and is enforced by considering in the numerical scheme additional grid points, schematically represented in Fig. 4.2. Left and right from the θ stencil we formally identify neighbouring grid points, denoted by $-P$ and $+P$ for the previous and upcoming grid, respectively. For enforcing equal gradients on the 0 and 2π boundaries additional 3 grid points are required: $-P_1, -P_2, -P_3$, while for prescribing $S_{\theta=0} = S_{\theta=2\pi}$ only one point is required. In this way

$$S^{(C)} - S^{(+P)} = 0, \quad (4.20)$$

and the continuity of the derivative is enforced by:

$$-3S^{(C)} + 4S^{(B)} - S^{(BB)} - 3S^{(-P1)} + 4S^{(-P2)} - S^{(-P3)} = 0. \quad (4.21)$$

The components $A_R^F, A_R^B, A_R^E, A_R^W, A_R^C$ represent the diagonal elements of the Jacobian. The resulting system matrix consists on average of 0.1% non-zero elements (see Fig. 4.3 a) for an example 8×8 matrix), which numerically is easy to manipulate and store.

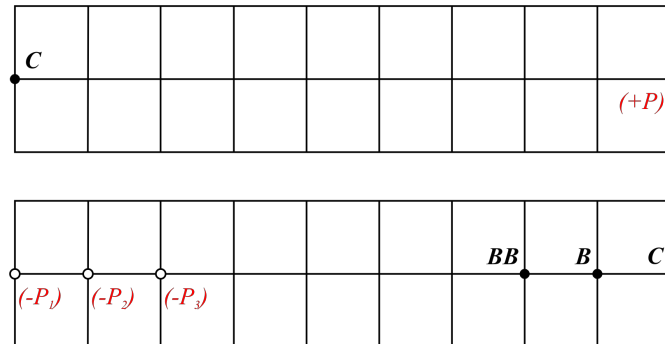


Figure 4.2: Grid points considered for the implementation of periodic boundary conditions

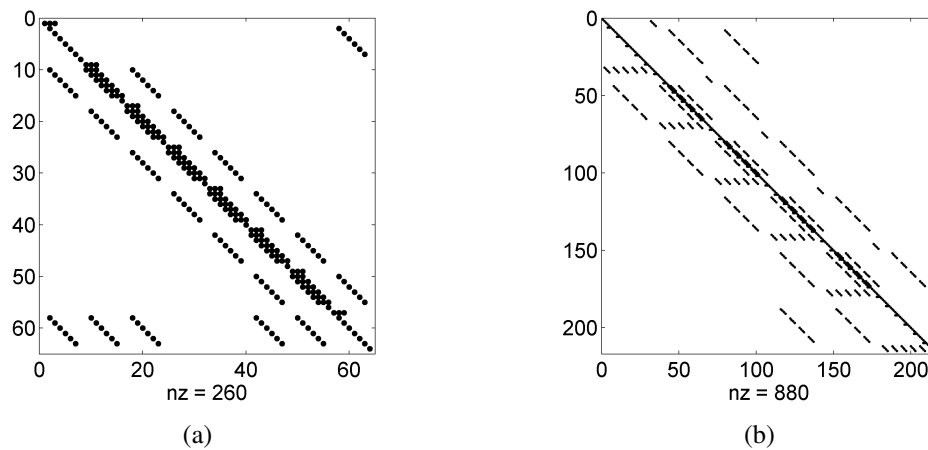


Figure 4.3: Typical sparse Jacobian: distribution of non-zero entries and their total number (nz) for (a) A_R , (b) A_D

Darcy's law Similar steps are performed for the discretisation of the terms in Eq. 3.14. The outer derivatives are approximated as:

$$\begin{aligned}
\frac{1}{r} \frac{\partial}{\partial r} \left(r \Phi_r \frac{\partial P_D}{\partial r} \right) &= \frac{1}{r} \frac{\left(r \Phi_r \frac{\partial P_D}{\partial r} \right)^n - \left(r \Phi_r \frac{\partial P_D}{\partial r} \right)^s}{\Delta r}, \\
\frac{1}{r^2} \frac{\partial}{\partial \theta} \left(\Phi_\theta \frac{\partial P_D}{\partial \theta} \right) &= \frac{1}{r^2} \frac{\left(\Phi_\theta \frac{\partial P_D}{\partial \theta} \right)^f - \left(\Phi_\theta \frac{\partial P_D}{\partial \theta} \right)^b}{\Delta \theta}, \\
\Gamma \frac{\partial}{\partial z} \left(\Phi_z \frac{\partial P_D}{\partial z} \right) &= \Gamma \frac{\left(\Phi_z \frac{\partial P_D}{\partial z} \right)^e - \left(\Phi_z \frac{\partial P_D}{\partial z} \right)^w}{\Delta z},
\end{aligned} \tag{4.22}$$

while the inner derivatives are:

$$\begin{aligned}
\left(r \Phi_r \frac{\partial P_D}{\partial r} \right)^n &= \frac{(r \Phi_r)^n P_D^N - (r \Phi_r)^c P_D^C}{\Delta r}, & \left(r \Phi_r \frac{\partial P_D}{\partial r} \right)^s &= \frac{(r \Phi_r)^c P_D^C - (r \Phi_r)^s P_D^S}{\Delta r}, \\
\left(\Phi_\theta \frac{\partial P_D}{\partial \theta} \right)^f &= \frac{(\Phi_\theta)^f P_D^F - (\Phi_\theta)^c P_D^C}{\Delta \theta}, & \left(\Phi_\theta \frac{\partial P_D}{\partial \theta} \right)^b &= \frac{(\Phi_\theta)^c P_D^C - (\Phi_\theta)^b P_D^B}{\Delta \theta}, \\
\left(\Phi_z \frac{\partial P_D}{\partial z} \right)^e &= \frac{(\Phi_z)^e P_D^E - (\Phi_z)^c P_D^C}{\Delta z}, & \left(\Phi_z \frac{\partial P_D}{\partial z} \right)^w &= \frac{(\Phi_z)^c P_D^C - (\Phi_z)^w P_D^W}{\Delta z}.
\end{aligned} \tag{4.23}$$

For the sake of simplicity we denote

$$D_r = r \Phi_r, \quad D_\theta = \Phi_\theta, \quad D_z = \Gamma \Phi_z. \tag{4.24}$$

Finally, by combining the inner and outer derivatives one obtains:

$$\begin{aligned}
\frac{1}{r} \frac{\partial}{\partial r} \left(r \Phi_r \frac{\partial P_D}{\partial r} \right) &= \frac{1}{r} \frac{D_r^n P_D^N - (D_r^n + D_r^s) P_D^C + D_r^s P_D^S}{\Delta r^2}, \\
\frac{1}{r^2} \frac{\partial}{\partial \theta} \left(\Phi_\theta \frac{\partial P_D}{\partial \theta} \right) &= \frac{1}{r^2} \frac{D_\theta^f P_D^F - (D_\theta^f + D_\theta^b) P_D^C + D_\theta^b P_D^B}{\Delta \theta^2}, \\
\frac{\partial}{\partial z} \left(\Phi_z \frac{\partial P_D}{\partial z} \right) &= \Gamma \frac{D_z^e P_D^E - (D_z^e + D_z^w) P_D^C + D_z^w P_D^W}{\Delta z^2}.
\end{aligned} \tag{4.25}$$

The coefficients of P_D are:

$$\begin{aligned}
(\mathbf{P}_D^{i+1})^N : A_D^N &= \frac{1}{r} \frac{1}{\Delta r^2} D_r^n, \\
(\mathbf{P}_D^{i+1})^S : A_D^S &= \frac{1}{r} \frac{1}{\Delta r^2} D_r^s, \\
(\mathbf{P}_D^{i+1})^F : A_D^F &= \frac{1}{r^2} \frac{1}{\Delta \theta^2} D_\theta^f, \\
(\mathbf{P}_D^{i+1})^B : A_D^B &= \frac{1}{r^2} \frac{1}{\Delta \theta^2} D_\theta^b, \\
(\mathbf{P}_D^{i+1})^E : A_D^E &= \frac{1}{\Delta z^2} D_z^e, \\
(\mathbf{P}_D^{i+1})^W : A_D^W &= \frac{1}{\Delta z^2} D_z^w, \\
(\mathbf{P}_D^{i+1})^C : A_D^C &= (-1) \left[\frac{1}{r} \frac{1}{\Delta r^2} (D_r^n + D_r^s) + \frac{1}{r^2} \frac{1}{\Delta \theta^2} (D_\theta^f + D_\theta^b) + \frac{1}{\Delta z^2} (D_z^e + D_z^w) \right].
\end{aligned} \tag{4.26}$$

These occupy a sparse pattern represented in Fig. 4.3 b). The mesh size of $6 \times 6 \times 6$ considered for the exemplified matrix yields 880 non-zero elements in the system matrix. The computation cost is therefore much higher than for the Reynolds equation, not surprisingly since the Darcy's equation is 3-dimensional.

The challenge of the numerical scheme is formulating the most suitable pressure-saturation relationship which would stabilize the steep transition between the phases. In the previous work of Elrod-Adams [6, 57], the pressure-density relationship used related the two quantities by the liquid bulk-modulus, a property which measures the compressibility of the medium. They used an alternating-direction implicit scheme in order to obtain steady-state solutions. This approach was stable as long as the value of the compressibility was kept finite, meaning that incompressible solutions could not be achieved. Moreover, their method was applied to tapered slider bearings, in which case the boundaries of the discontinuous phase were fixed by the geometry grooves, and did not occur spontaneously, as in the case of a circular journal bearing. We took on a different approach by using a technique referred to as ‘‘annealing’’, an analogy to the mechanical process of a high temperature heated metal cooled down at a low rate. From a numerical point of view, simulated annealing is an optimization technique that finds the global optimum of a system, avoiding solutions that would render only local minima/maxima [68]. Here we modify the initial Elrod-Adams scheme and solve the steady-state problem in a direct iterative scheme, for the incompressible case. The isothermal compressibility $\partial S / \partial P_R$ is controlled by β , a positive non-dimensional quantity ($\beta > 0$). This then enters in the artificial $P_R - S$ relationship by

$$P_R - P_C = \sqrt{1/\beta^n + \beta^2(S-1)^{2n_0}} + \beta(S-1)^{n_0}, \quad n \geq 4, \quad n_0 = 1, 3, 5, \dots, \tag{4.27}$$

such that the incompressible limit is reached when $\beta \rightarrow \infty$:

$$\frac{1}{\beta^n} \rightarrow 0 : \quad \frac{P_R - P_C}{2\beta} (S - 1)^{n_0} \quad \text{and} \quad S \rightarrow 1. \quad (4.28)$$

The quantity $P_R - P_C$ is taken as positive throughout, and large values are encountered outside of the cavitation region. A plain linear variation of β with each iteration proved a too harsh choice, and a more refined relationship was needed. We therefore implemented the relationship which favours fast convergence:

$$\beta = \beta_{min} + (\beta_{max} - \beta_{min}) \tanh[0.04(i - 1)], \quad (4.29)$$

with β_{min} and β_{max} to be fixed by trial and error.

The very core of the iterative algorithm is the switching between solving the Reynolds and Darcy problem. First, the Darcy's equation is solved. This yields a initial value for $P_{D,1}$ and thus, $v_{D,r}$. Then, at $i = 1$ the iterative loop starts and its step is incremented every time with 1. By employing the linearisation by $S = S_i$ of the Reynolds equation, i.e. 4.7, we obtain an approximation of S_{i+1} . This, together with $v_{D,r}$ feeds into the initial Reynolds problem 3.9 and $P_{R,i+1}$ is calculated on the basis of Eq. 4.27. $P_{D,i+1}$ is updated according to 3.17, and i is increased with 1. We consider to have reached a stable solution when the Euclidean norm between two consecutive values of P_R are below \mathbf{u} , the machine precision:

$$\frac{\|P_{R,i+1} - P_{R,i}\|_2}{\|P_{R,i+1}\|_2} < \sqrt{\mathbf{u}}. \quad (4.30)$$

Other types of norms can also be considered, however, using the Euclidean norm avoids the possible difficulties in the convergence due to round-off errors, while being sensitive enough to the very small variations of P_R inside the cavitation region.

Moreover, the solution of the Reynolds equation is stabilized by employing under-relaxation according to

$$P_{R,i} = \varrho P_{R,i-1} + (1 - \varrho) P_{R,i}, \quad 0 < \varrho < 1. \quad (4.31)$$

That is, only the fractions ϱ (under relaxation factor) of the updated approximations S_i and $P_{R,i}$ feed into the discretised Reynolds problem, to be solved for the consecutive update S_{i+1} , and the convergence criterion, respectively.

This advanced numerical scheme proves to handle the numerical instabilities due to the expected saturation discontinuity well enough. The proper mesh resolution together with the upwind (backwards in θ) discretisation of the advective term and the iterative adjustment of the P_R - S relationship avoids typical grid oscillations.

4.2 Parameter study: general case

In this section we present the first results of the numerical algorithm employed. The choice of the input parameters (both geometrical and numerical ones) which define the general case is explained below.

4.2.1 Set-up of the input parameters

The numerical approach to solving the system presented in Sect. 3.2 is based on the artificial pressure-density relationship given by Eq. 4.27. The parametrisation of the $P_R - S$ relation is depicted in Fig. 4.4, where β_{max} and n are varied. Already $\beta = 30$ appears to be sufficiently high for reaching the incompressible limit. Larger values of β increase the speed of convergence towards the solution, however, experience has shown that high values also render the occurrence of instabilities in the iteration process. The parameter n has no physical meaning, but it is used to smooth the transition of P_R around $S = 1$. In fact, the stability of the scheme depends not only on the choice of β_{max} but also on the under relaxation factor ϱ . For this reason, an overview of the convergence domain can be obtained when β_{max} and ϱ are systematically varied in a parameter study, but in the same time keeping all the other input parameters fixed. Figure 4.5 shows the number of iterations required to reach a converged solution (imposed numerical tolerance $\mathbf{u}_c = 10^{-8}$), for two values of $\varepsilon = 0.1, 0.8$, when evaluated by means of the L_2 norm. A value of 0 indicates the inability to reach a numerical converged solution. The results vary greatly with ε : for low eccentricities (Fig. 4.5 a)) the choices of ϱ and β_{max} appear to have only a very small influence on the speed of convergence and moreover, all parameters combinations yield converged solutions. In the case of higher eccentricity (Fig. 4.5 b)), less than a half of the parameter space given by ϱ shows converged solutions. The conclusion of this study is that $0.9 \leq \varrho \leq 1$, and $\beta_{max} < 12$ are viable choices for obtaining stable converged solutions.

Based on the results presented so far, we are now able to define a set of *standard* numerical parameters which will be used in the upcoming simulations and which we consider will bring the best results in terms in stability and convergence, given in Tab. 4.1.

Strong variations in the stability of the calculation definitely occur when extreme values of one or more of the 5 non-dimensional groups are employed, which may induce other effects not considered initially by the assumed physics. However, for this and the upcoming studies, unless stated otherwise, the *standard* set of geometrical/physical parameters defined in Tab. 4.2 will be used. The geometrical aspect ratios Γ , Λ as well as the coupling parameter K are chosen based on real industrial bearing geometries, while the parameter related to the operation conditions, P_C , corresponds to moderate rotational speeds and a measured viscosity of an oil commonly used in the lubrication of the chosen industrial bearing. Also, we assume that the permeability of the sinter is isotropic and homogeneous.

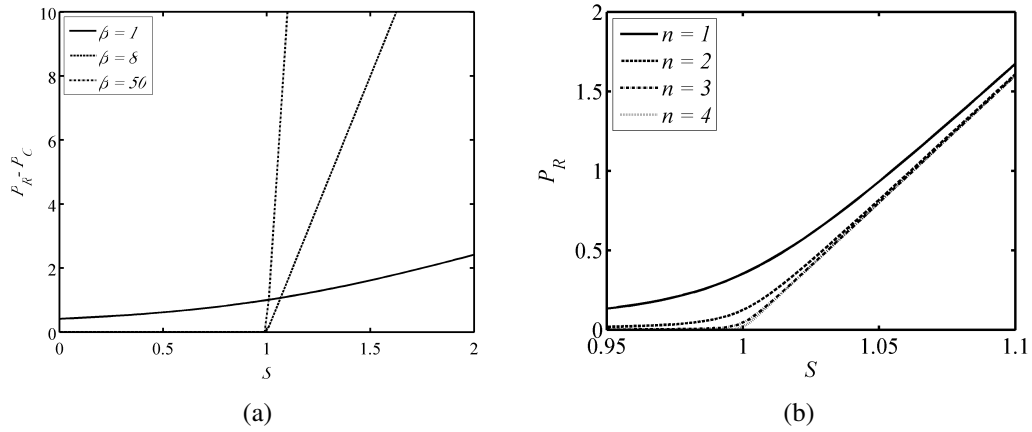


Figure 4.4: Parametrisation of the $P_R - S$ relationship: (a) different values of the compressibility parameter β , (b) fixed $\beta = 8$ and different values of the parameter n

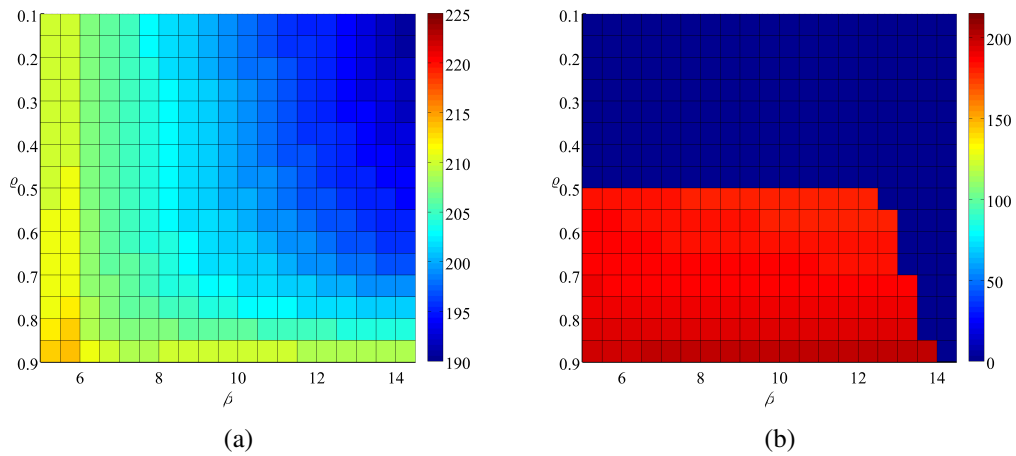


Figure 4.5: Convergence study for q, β_{max} : number of iterations needed to reach a converged solution versus q, β_{max} for: (a) $\varepsilon = 0.1$, (b) $\varepsilon = 0.8$ at a tolerance of $\mathbf{u}_c = 10^{-8}$; convergence criteria based on the L_2 norm

4.2.2 Typical pressure and saturation distribution

The results of the calculations performed with the standard parameters from Tab. 4.2 yield the spatial distributions of the lubricant pressure in the gap and its saturation. As a first insight into the flow behaviour under different loads, we consider two values of

n	n_0	β_{min}	β_{max}	ϱ
4	1	2	8	0.95

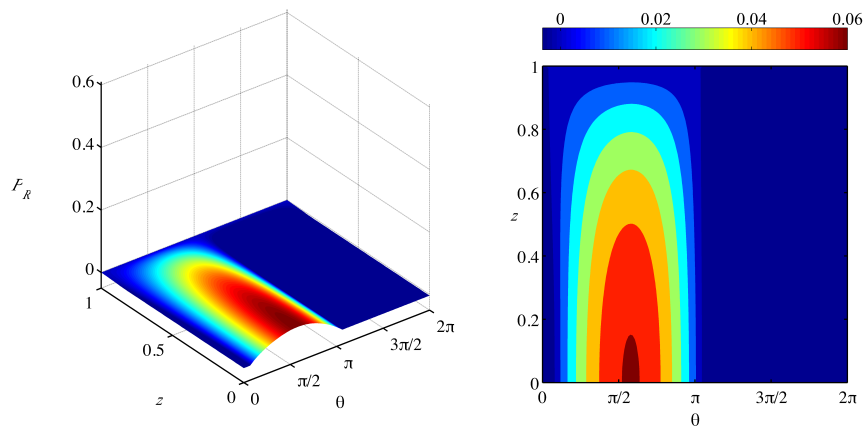
Table 4.1: Standard numerical parameters

\tilde{r}_b [mm]	\tilde{l}_b [mm]	$\tilde{\lambda}_b$ [mm]	\tilde{c} [μm]	$\tilde{\omega}$ [min^{-1}]	$\tilde{\Phi}_b$ [m^2]	$\tilde{\eta}$ [Pa s]	\tilde{p}_c [Pa]
4	11	3.75	8	2000	$1.8 \cdot 10^{-14}$	0.065	0.01
Γ	K	Λ	P_C				
0.52	0.64	0.93	-0.0049				

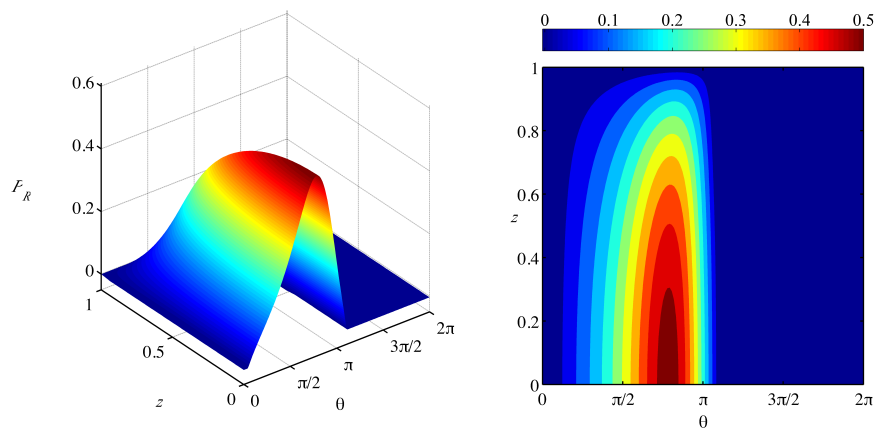
Table 4.2: Standard input parameters used in the calculation: dimensional inputs and their equivalent non-dimensional groups

the eccentricity ratio, namely $\varepsilon = 0.1, 0.6$. The resulting typical distributions for these values are depicted in Fig. 4.6,4.7, where two views for each case are shown. In both cases it is seen that cavitation initiates at the location of the minimum film thickness, around $\theta = \pi$, where on the one hand, P_R reaches its minimum value, P_C , and on the other hand S drops below 1. The extent of the cavitation in axial direction (z) varies with ε , so that for a value of $\varepsilon = 0.6$ the cavitated flow region spans until almost the edge of the bearing $z = 1$. When the load is increased, the drop in pressure becomes more abrupt and in the same time S takes on considerably smaller values. The latter implies that under higher loads the mixture region contains more vapour as compared to the case of low load.

We remark a recurring behaviour in the saturation distribution around $\theta = 2\pi$, where S exhibits a sudden jump to the value of the fully liquid phase. This discontinuity turns out to be present in every configuration studied (also in the subsequent numerical study), and can thus be safely considered as inevitable. Fig. 4.8 depicts the pressure of the lubricant passing through the sinter matrix, for the same standard configuration and taken at the bearing symmetry line $z = 0$. Its value across the radial direction decreases slightly from the one of P_R in the loaded area of the lubrication gap ($r = 1, \theta \in [0, \pi]$), while exhibiting a slight increase from P_C in the unloaded area ($\theta \in [\pi, 2\pi]$), the latter in agreement with the assumptions put forward in Sect. 3.2. The maximum of P_D is displaced towards π with the higher eccentricity ratio and shows a more abrupt drop around π .

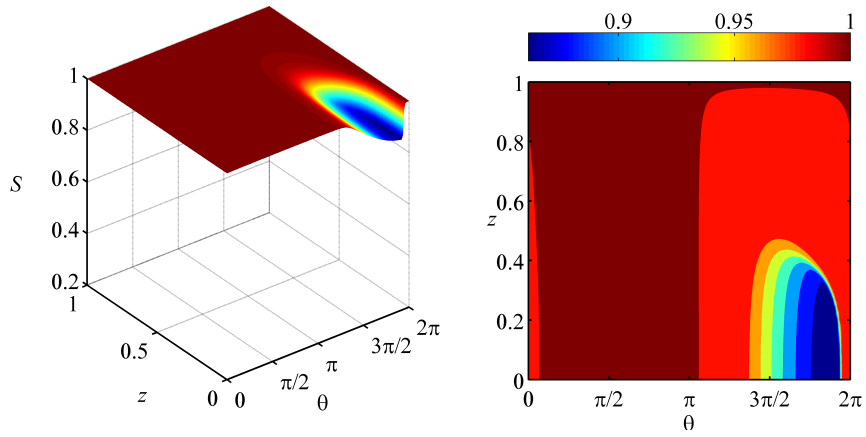


(a)

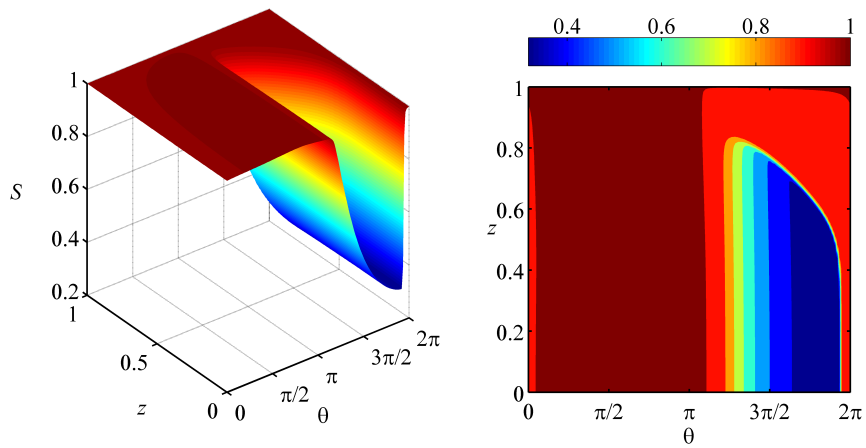


(b)

Figure 4.6: Numerical results for the standard parameters: non-dimensional pressure distribution in the lubrication gap for: (a) $\varepsilon = 0.1$, (b) $\varepsilon = 0.6$



(a)



(b)

Figure 4.7: Numerical results for the standard parameters: lubricant saturation for: (a) $\varepsilon = 0.1$, (b) $\varepsilon = 0.6$

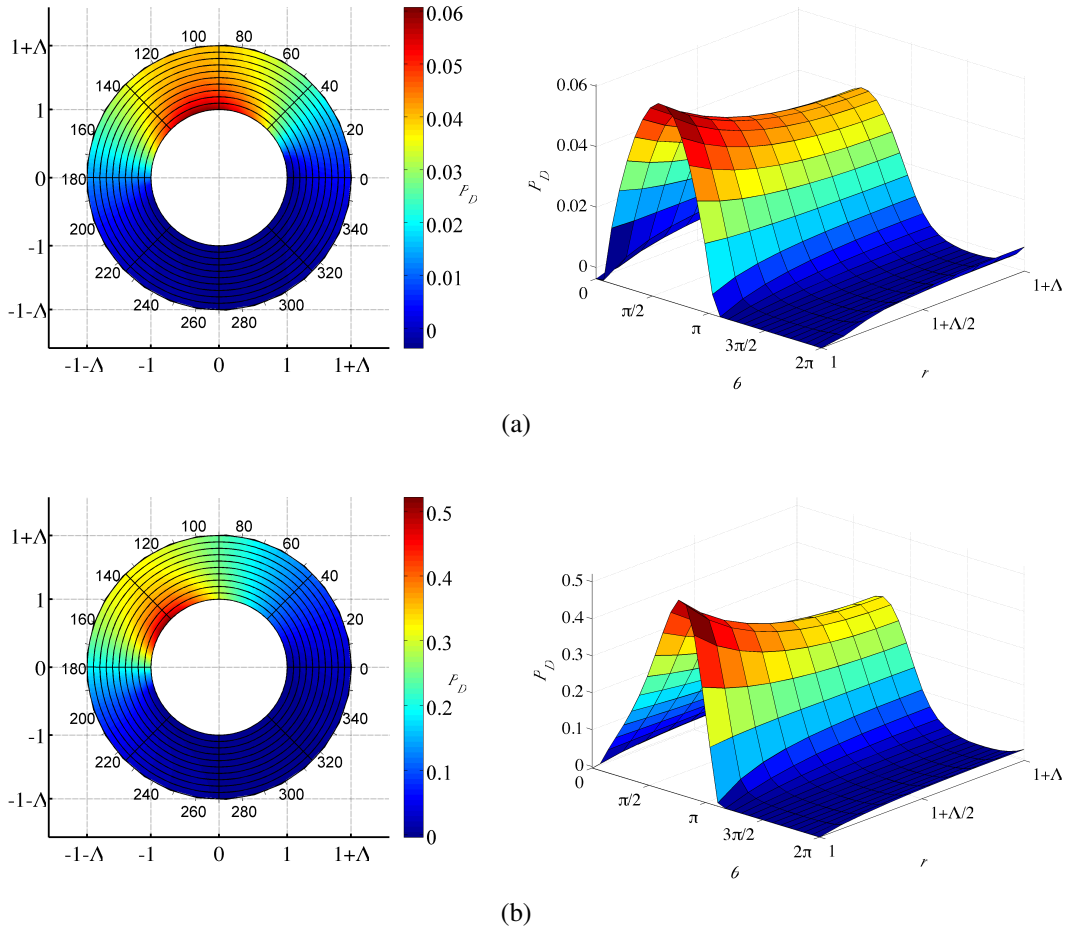


Figure 4.8: Numerical results for the standard parameters: non-dimensional sinter pressure taken at the bearing line of symmetry $z = 0$ for: (a) $\varepsilon = 0.1$, (b) $\varepsilon = 0.6$

4.2.3 Influence of K and ε

The variation of the eccentricity ratio, although providing with valuable knowledge regarding cavitation, is not enough to establish the performance of a certain configuration. We therefore proceeded with the variation of the coupling parameter K and extend the range of values for ε . Solutions are obtained only up to a value of ε situated near 0.9, as by exceeding this value we encounter a failure of convergence. The limits for K were chosen in such a way as to obtain a clear distinction between the values at which they are held constant.

In Fig. 4.9 the initial set-up is plotted for F_D for several distinct values of the coupling parameter K (for the same values of the eccentricity ratios), however this time by plotting

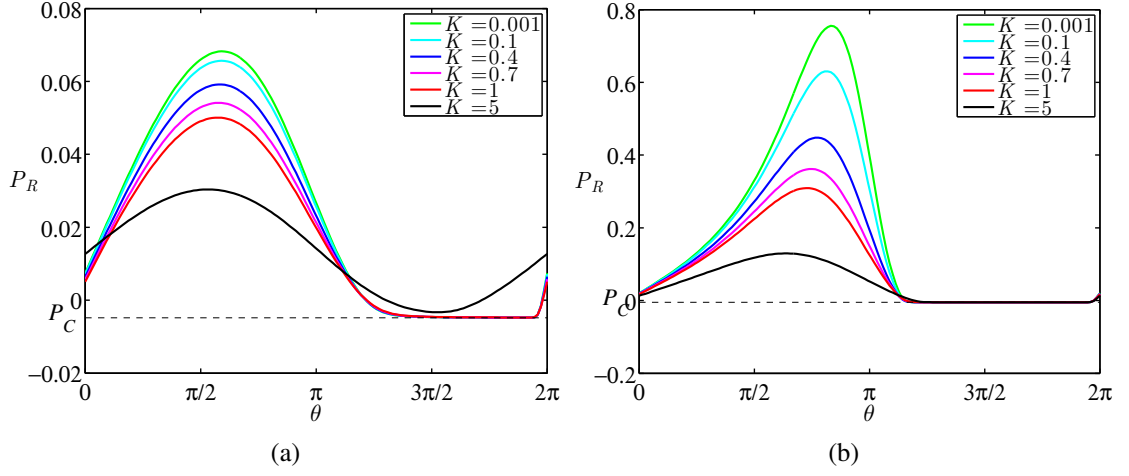


Figure 4.9: Pressure distribution in the lubrication gap at the symmetry line $z = 0$ for distinct values of K and: (a) $\varepsilon = 0.1$, (b) $\varepsilon = 0.6$

the values of P_R at the symmetry plane $z = 0$. This type of representation is useful insofar as it provides straightforward information regarding whether cavitation occurred. An increase in K of one order of magnitude can be the result of either increased permeability, smaller radial clearance or a combination of both. The effect of a significantly higher K is a lower P_R in the loaded area, which is explained by the reduced load carrying capacity of very permeable bearings as the lubricant escapes much easier through the pores of the matrix. It is interesting that for lower loads and high values of the coupling parameter cavitation does not appear to develop, as hinted by $P_R > P_C$ over θ . This points to the existence of a certain threshold for K , depending of ε , beyond which cavitation ceases to occur. This threshold is further identified by tracking the minimum pressure occurring in the lubrication gap for each combination of parameters ε – K . Figure 4.10 depicts *solely* the configurations for which the minimum pressure encountered is larger than the cavitation pressure: $P_{Rmin} > P_C$, indicating the fact that the lubricant does not cavitate. Particularly, we remark from Fig. 4.10 that only a narrow constellation of parameters ε – K delimited by $\varepsilon \in [0.001 - 0.15]$ is not affected by cavitation. Plotting the minimum P_R for $\varepsilon > 0.15$ would collapse on a single horizontal line corresponding to P_C , and are therefore not represented here.

The following curves in Fig. 4.11–4.13 are obtained by cubic interpolation of the calculated data points. From Fig. 4.11 a) one detects how changing the value of K affects the attitude angle ψ in dependence of ε , which is varied between 0 and 0.9. The (expected) range $\pi < \psi \leq 3\pi/2$ reflects the occurrence of the pressure maximum and of cavitation in the, respectively, convergent ($0 < \theta < \pi$) and divergent ($\pi < \theta < 2\pi$) parts of the bearing. In the case of an almost solid bearing ($K = 0.001$), ψ exhibits a major

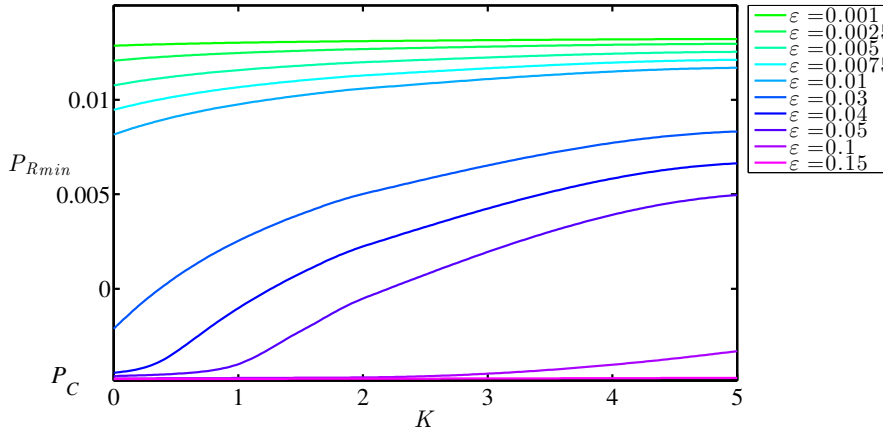


Figure 4.10: Minimum pressure in the lubrication gap vs. K for distinct values of ε

change when ε is varied in its entire range, bounded by 0 and 1. We remark that for more porous bearings, this change is not so drastic, and the curve globally flattens. On the contrary, ψ attains smaller values the smaller K is in the limit $\varepsilon \rightarrow 0$, though we concede that the then intersecting curves can locally be hardly distinguished from each other.

Next, the variation of S_o is plotted in Fig. 4.11 b), where one can see that the load capacity generally decreases for increasing values of K . The impact of its variation on the load is more pronounced for lower values of K and medium to high values of ε . Finally, as K becomes quite large, the bearing loses its capacity of carrying the load.

The frictional characteristics of the standard configuration are put in evidence by plotting μ over ε and K . This type of representation contributes to the design of porous journal bearings as it can point out the optimum set-up which yields to suitably low friction coefficients. Fig. 4.12 and 4.13 depict these results, and due to the different scales involved, are resolved into two regions. In the case of μ vs. ε (Fig. 4.12), the friction coefficient shows an overall decreasing trend, with an abrupt decrease in the region $\varepsilon \in [0, 0.02]$. In contrast, near $\varepsilon = 0.8$, and for higher values of K , μ appears to increase slightly. The lack of data points beyond $\varepsilon = 0.85$ in the case of $K = 5$ indicates that for the respective configuration no converged solutions were obtained.

For fixed values of ε , the friction coefficient μ is seen to increase almost linearly when K is increased, at an almost constant slope for a fixed value of ε (see Fig. 4.13). Interestingly, varying the coupling parameter has comparatively little effect on the evolution of μ considering that K spans a rather wide range of values.

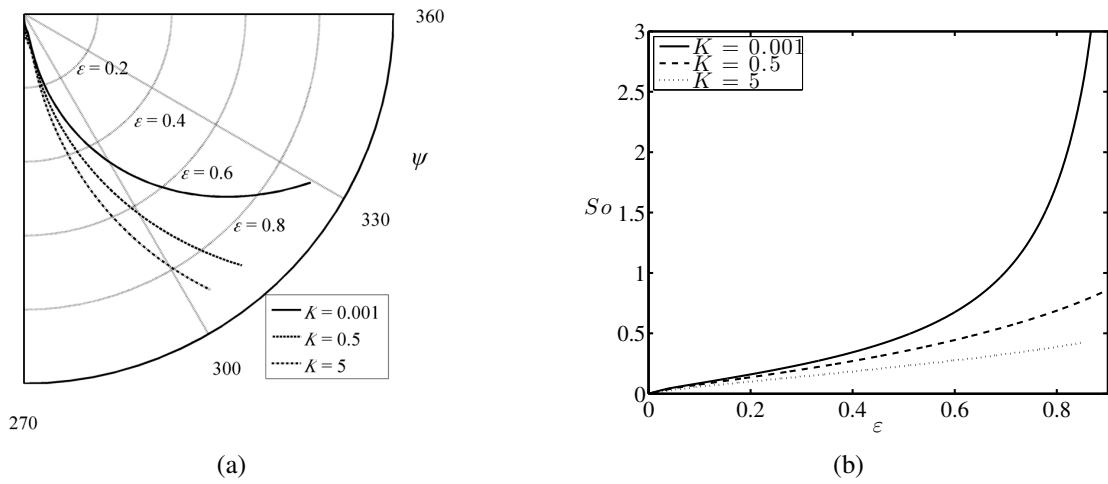


Figure 4.11: (a) Attitude angle ψ , (b) Sommerfeld number So vs. eccentricity ratio ε for various values of the permeability parameter K

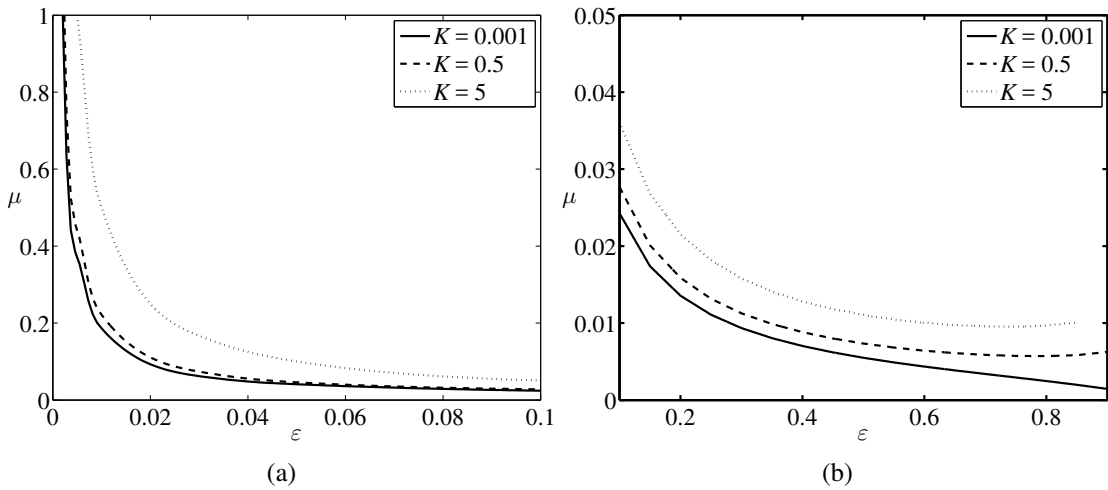


Figure 4.12: Variation of the friction coefficient μ with the eccentricity ratio ε resolved into two regions: (a) $\varepsilon \in [0, 0.1]$, (b) $\varepsilon \in [0.1, 0.9]$

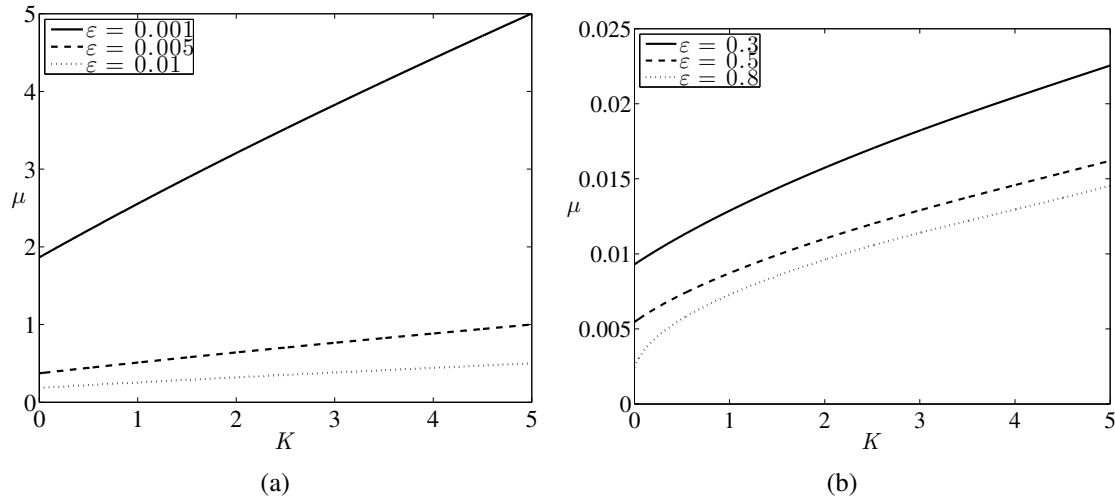


Figure 4.13: Variation of the friction coefficient μ with the coupling factor K resolved into two regions of ε : (a) low values of ε and (b) high values of ε

4.3 Extended parametric study

A more complete analysis involves an extensive parameter study where all the 5 non-dimensional parameters are gradually varied. This will not only provide with the limitations and specific behaviour of the bearing under various conditions, but as we will see in Ch. 5.4, it enables a strategy to approximate the bearing load beforehand, as the load is merely a result of the calculation, and not a direct input. We build a structured database which consists of a large number of calculations for all the parameter combinations given by the ranges of Γ , ε , K , Λ and P_C , given in Tab. 4.3. One may remark that the maximum value of ε in the database is 0.8. This is due to the increased sensitivity of the calculation as $\varepsilon \rightarrow 1$ on the other 4 involved parameters. While for middle range values of Γ , K , Λ and P_C we can obtain converged solutions for up to $\varepsilon = 0.9$ (as seen in Sect. 4.2.3), this cannot be achieved for all Γ , K , Λ and P_C . Even so, the data contained in the database provides with valuable input on the general tendencies and characteristic behaviour of the solutions by examining the change of the Sommerfeld number, So .

Γ	ε	K	Λ	P_C
[0.3,10]	[0.005, 0.8]	[0.01, 20]	[0.4, 1.6]	$[-10^2, -10^{-5}]$

Table 4.3: Computation domain for the parameter study

A total of 206976 configurations were calculated. The ranges of the parameter values are chosen so as to approach the limits for which the current theory becomes in-

sufficient without proper extra handling. This in fact is the first output of the database, as the lack of data points in the resulting 5-dimensional matrix indicates loss of solution. Due to the very high amount of data, we look at the results obtained for four types of geometries and assessing the friction coefficients and Sommerfeld number when the two essential parameters, ε and K are varied. As a necessary remark, here the analysed friction coefficient represents a normalized value of the original quantity of the form:

$$\mu_n = \mu \tilde{r}_b / \tilde{c}.$$

Secondly, the results shown in Sect. 4.2.2 suggested that the saturation jump may be a recurrent behaviour in all configurations. In order to assess the validity of this statement by means of the calculated database, we resort to plotting saturation curves at the bearing symmetry line $z = 0$, versus the circumferential coordinate θ , for cases where cavitation occurs. Knowing that varying the eccentricity ratio affects the most the evolution of the saturation in the cavitation area, we plot the saturation for two values of ε and, in turn, the lower and upper limits of the parameters which make-up the database domain. It turns out that only Γ and K have a relevant influence on the way saturation progresses, as explained in the section below.

Short vs. long width bearing In a first instance we extract the data points corresponding to a short (narrow) width bearing of $\Gamma = 5$ and compare them to a long width bearing of $\Gamma = 0.3$. The evolution of μ_n and S_o over the eccentricity ratio and various values of the coupling parameter K are shown in Fig. 4.14 and Fig. 4.15, respectively. In both cases $\Lambda = 0.8$ and $P_C = -0.001$.

A long width bearing shows considerable lower friction coefficients than a short width one, and has an increase of an approximately factor 3 in load capacity. In fact, a variable permeability in short bearings is of interest only for highly loaded bearings, in this case $\varepsilon > 0.5$. At high values of K and ε however the loss of solution is remarked to occur earlier than $\varepsilon = 0.8$, suggested by the lack of data points. In terms of the saturation jump, the distinction between long- and short-width bearing is shown in Fig. 4.16 a). For a short width bearing under moderate loading ($\varepsilon = 0.3$, $\Gamma = 10$), the cavitation area is restricted to a narrow region around $\theta = 3\pi/2$, while for the case of a long bearing, it spans on almost half of the circumference of the bearing. In the case of higher loading however, the curves lie more closely to each other.

A more interesting behaviour is the smoothing out of the otherwise sharp transition of S near $\theta = 2\pi$ for the case of high load and high coupling parameter ($\varepsilon = 0.7$, $K = 20$). In fact, the case $K = 20$ is associated with noticeably smaller cavitation regions, also for small eccentricity ratios.

Thin seat vs. thick seat bearing The second direction for evaluating the data contained in the database is to check whether the thickness of the porous seat plays any role into the frictional behaviour. In the same manner as above, we plot the normalized

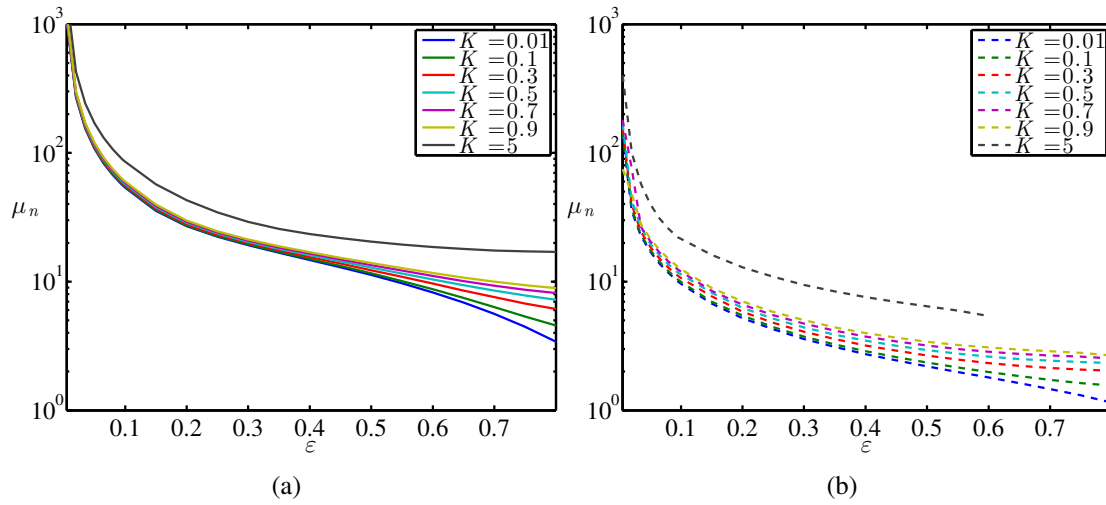


Figure 4.14: Normalized friction coefficient μ_n vs. ε for (a) short width bearing $\Gamma = 5$ and (b) long width bearing $\Gamma = 0.3$. In both cases $\Lambda = 0.8, P_C = -0.001$

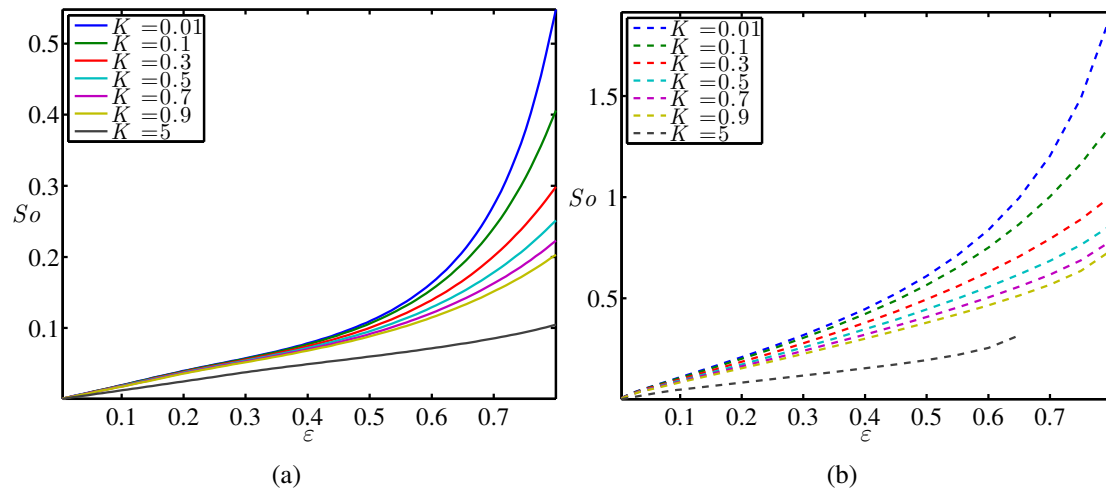


Figure 4.15: Sommerfeld number S_o vs. ε for (a) short width bearing $\Gamma = 5$ and (b) long width bearing $\Gamma = 0.3$. In both cases $\Lambda = 0.8, P_C = -0.001$

friction coefficient and Sommerfeld number vs. the eccentricity ratio, and the results are seen in Fig. 4.17. The curves lie very closely to one another, indicating no significant distinction between the case of a thin or thick bearing seat, apart from an apparent loss of solution for the particular case of a thin, but permeable seat, $\Lambda = 0.3, K = 5$. We therefore continue with selecting a broader domain around this case, namely $\Lambda = 0.4$ and $K = 20$ and plot the sought quantities for various values of the aspect ratio.

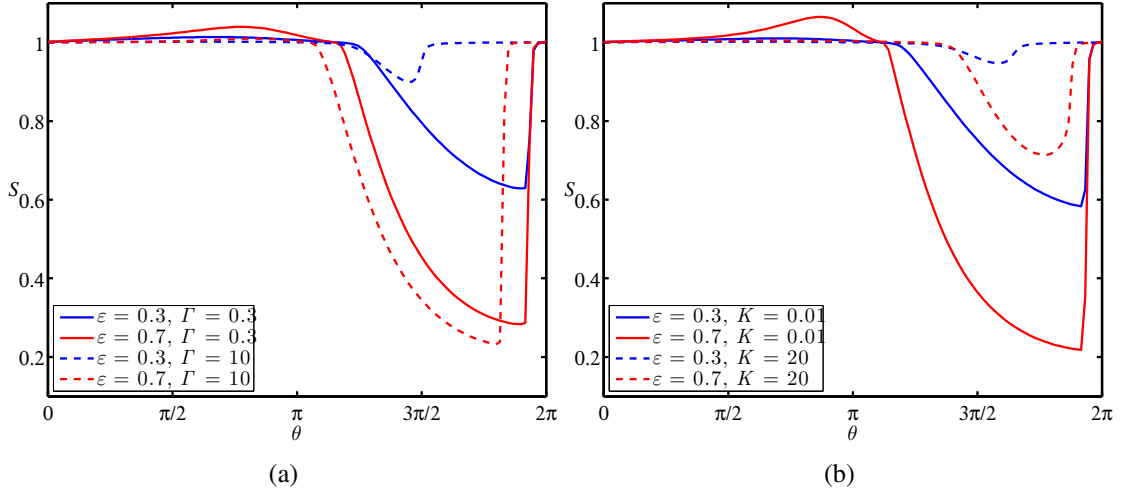


Figure 4.16: Lubricant saturation plotted at the symmetry line $z = 0$ over the circumferential coordinate θ , for two distinct values of the eccentricity ratio and (a) two limiting values of the aspect ratio Γ and (b) two limiting values of the coupling parameter K . Otherwise stated, the input parameters are: $\Gamma = 0.9, K = 0.5, \Lambda = 0.8, P_C = -0.001$

Figure 4.18 shows the limitation of the database, namely the particular combination of parameters for which solutions cannot be achieved. Only a few of the calculated configurations yielded converged solutions, with the maximum reached eccentricity ratio being $\varepsilon = 0.6$, corresponding to a very permeable thin-seat, short-width bearing. These numerical results demonstrate that the case $K \gg 1, \Lambda \ll 1$ cannot be calculated by the classical lubrication approach used so far. Here the reduced Eq. 3.22 is applicable. The numerical results obtained for this case are shown in the upcoming Sect. 4.5.

4.4 Anisotropic permeability distribution

The results presented so far were obtained for configurations where the permeability was considered isotropic. This is however not true in reality, as the pressure applied in the manufacturing processes of sintered bearings cannot be perfectly equally distributed throughout ([69]). The variation in permeability can therefore be a function of the bearing design parameters [70], in our case Γ and Λ . In this section we will vary the permeability tensor Φ and look at its effects on the friction coefficient and load capacity for various geometries.

The first strategy pursued here is to vary the diagonal components of the permeability tensor. We therefore choose 3 particular distributions, where in each case the permeability in one direction is much greater than the one in the other 2 directions and

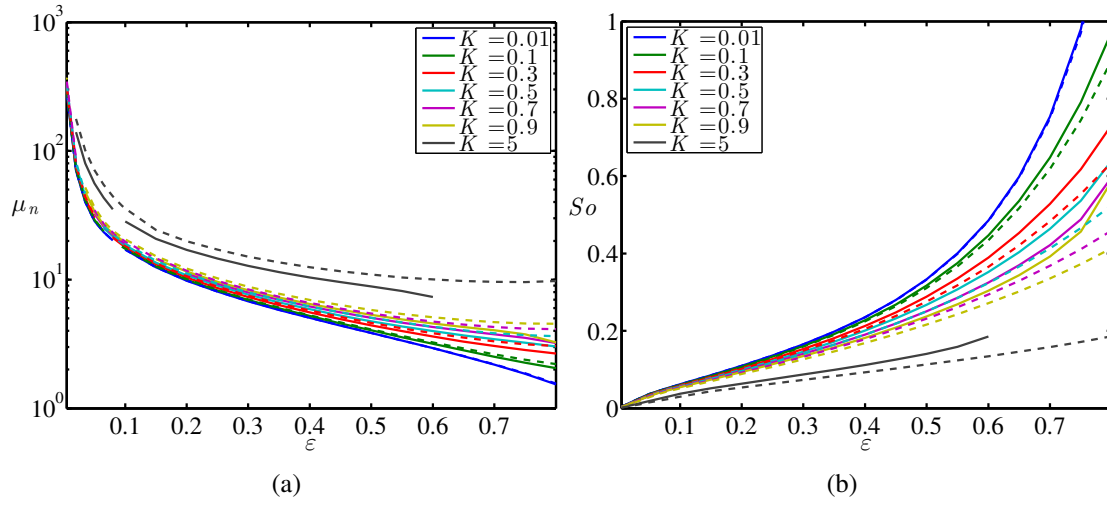


Figure 4.17: (a) Normalized friction coefficient μ_n and (b) Sommerfeld number S_o vs. ε for a thin seat bearing $\Lambda = 0.3$ (continuous line) and a thick seat bearing $\Lambda = 1.6$ (dashed line). In both cases $\Gamma = 1, P_C = -0.001$

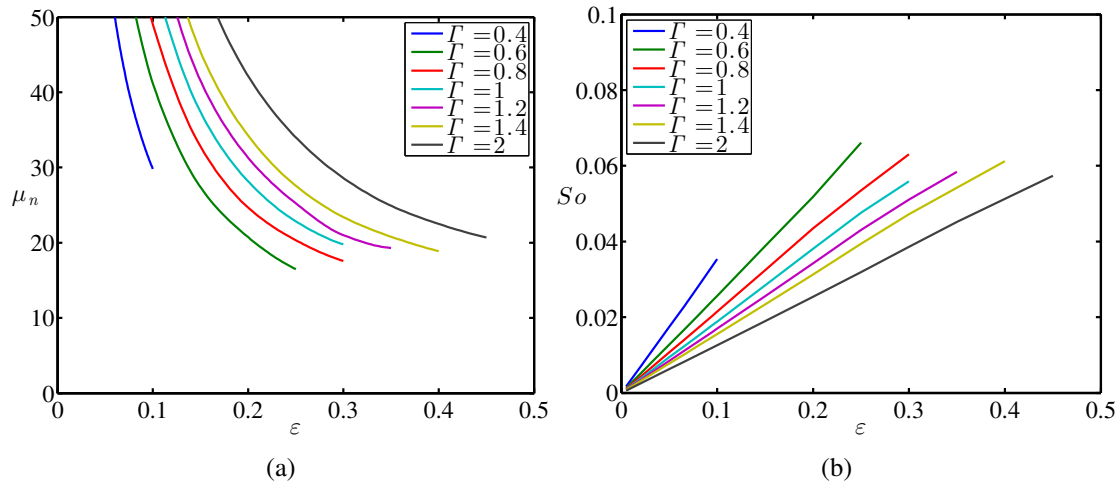


Figure 4.18: (a) Non dimensional friction coefficient and (b) Sommerfeld number vs. the eccentricity ratio for $\Lambda = 0.4, K = 20, P_C = -0.001$

compare the resulting friction coefficients with the isotropic case. The proposed distributions are as follows:

$$\Phi_1 = \begin{bmatrix} 1 & 0 & 0 \\ 0 & 1 & 0 \\ 0 & 0 & 10 \end{bmatrix}; \quad \Phi_2 = \begin{bmatrix} 1 & 0 & 0 \\ 0 & 10 & 0 \\ 0 & 0 & 1 \end{bmatrix}; \quad \Phi_3 = \begin{bmatrix} 10 & 0 & 0 \\ 0 & 1 & 0 \\ 0 & 0 & 1 \end{bmatrix}, \quad (4.32)$$

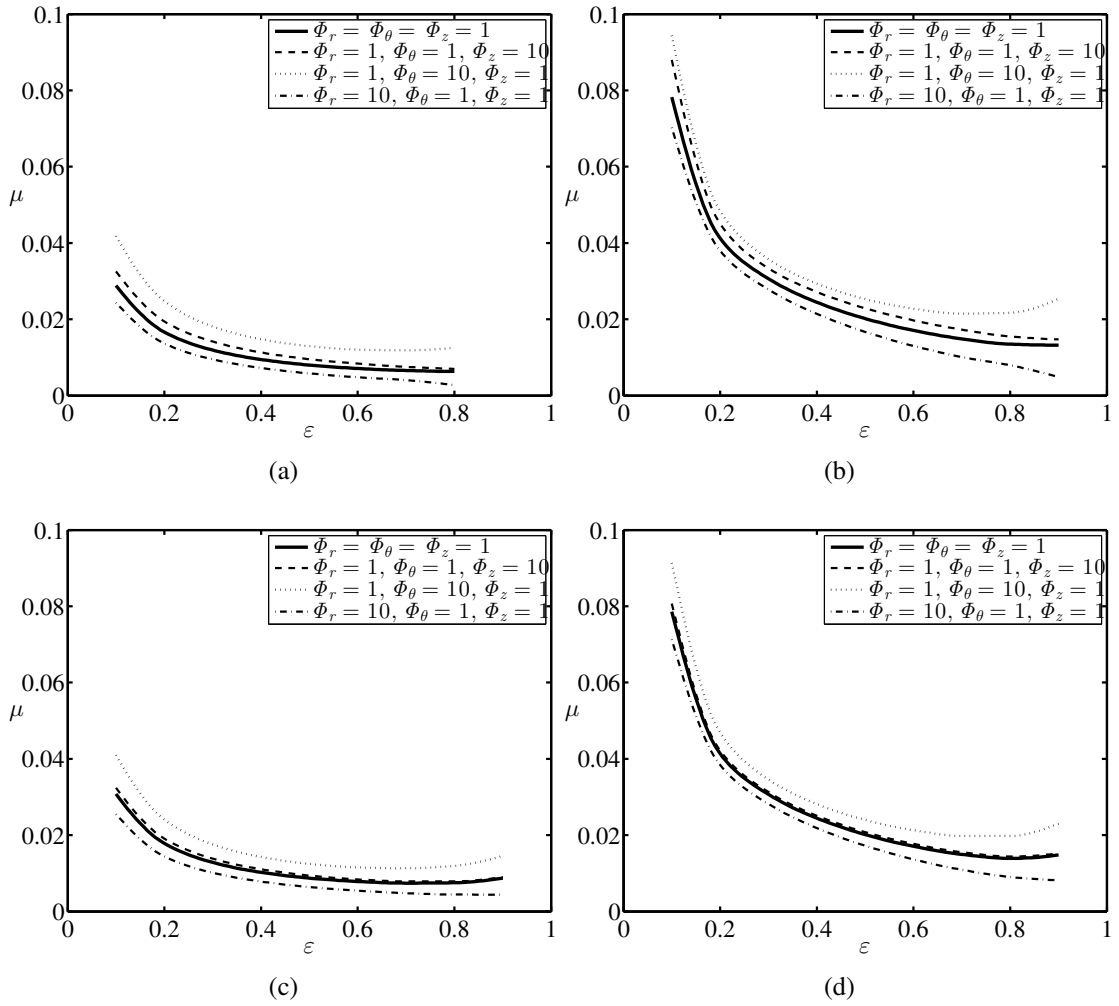


Figure 4.19: Friction coefficients for a non-homogeneous permeability distribution for (a) thin, long bearing $\Lambda = 0.5, \Gamma = 0.5$, (b) thin, short bearing $\Lambda = 0.5, \Gamma = 3$, (c) thick, long bearing $\Lambda = 2, \Gamma = 0.5$, (d) thick, short bearing $\Lambda = 2, \Gamma = 3$

For this purpose Λ takes on the values 0.5, 2, corresponding to a thin and thick porous seat, respectively, while $\Gamma = 0.5, 3$, the cases of a short and long width bearing. K is kept constant at $K = 1$ and $P_C = -0.046$. The results of this study are presented below.

From Fig. 4.19 one can observe an overall trend: a dominant radial permeability ($\Phi_r = 10, \Phi_\theta = 1, \Phi_z = 1$) performs better from the point of view of frictional coefficient as it seen to lie below the other 3 curves. The separation from the isotropic curve of narrow bearings is more pronounced for medium to high loads ($\varepsilon > 0.5$), as seen in Fig. 4.19 b), d). For the same configurations, at low loads one can see that the

4 curves are very close to one another, in contrast with the case of long bearing cases (Fig. 4.19 a), c)).

Next, we employ a more complex permeability variation through the seat by applying a sinusoidal function which governs its variation. The parametrized two-dimensional function defines the permeability variation in the circumferential and radial direction, and is of the form

$$\Phi(r, \theta) = \left[1 + (1 - \Phi_c) \frac{\arctan(J_\theta \cos(n\theta)) - \arctan J_\theta}{2 \arctan J_\theta} \right] \cdot \left[\frac{\arctan[J_r \Lambda(1 - \lambda_c)] - \arctan[J_r(r - 1 - \Lambda\lambda_c)]}{\arctan[J_r \Lambda(1 - \lambda_c)] - \arctan(-J_r \Lambda \lambda_c)} \right], \quad (4.33)$$

where the parameters Φ_c, J_θ, n, J_r and λ_c control as follows, the permeability of the compressed areas in multiples of $\tilde{\Phi}_r$, the sharpness of the transition in θ direction, profile multiplicity, sharpness of the r -transition and depth of compressed areas in multiples of Λ . Although Eq. 4.33 allows for a multitude of combinations of the permeability distribution, we chose for this study only 4 particular ones. The combinations of parameters used are given in Tab. 4.4 and shown graphically in Fig. 4.20. Profiles a), b) depict distributions with an even and odd number of multiplicities, while in c) we vary the permeability of the compressed areas, and in d) the compression in radial direction (pointing to a permeability variation at the inner surface of the seat). We thus applied

Set	Φ_c	J_θ	n	J_r	λ_c
(a)	0.1	10	2	30	0.8
(b)	0.1	10	3	30	0.8
(c)	0.7	10	2	30	0.8
(d)	0.1	10	2	30	0.2

Table 4.4: Parameters used for the sinusoidal permeability bearing

these profiles to a bearing with $\Gamma = 0.5, \Lambda = 2, P_C = -0.0046$, and only varied the usual parameters ε and K . The results obtained for these 4 types of permeability distributions are given in Fig. 4.21 in comparison with the case $\Phi_r = \Phi_\theta = \Phi_z$ for $K = 1$ and for higher values of K in Tab. 4.5. Even if mostly small deviations from the constant case can be observed, the distinction between a two-fold multiplicity (a) and a three-fold one (b) is apparent in both friction coefficient and load capacity representations. Interestingly, for high values of K (see Tab. 4.5) a 3-fold multiplicity of the bearing permeability yields a decrease in the friction coefficient, even more, in comparison with the constant case. Also, varying the permeability only near the inner bearing surface (d), rather than throughout its whole thickness (a), (b) considerably lowers the bearing's capacity of carrying the load.

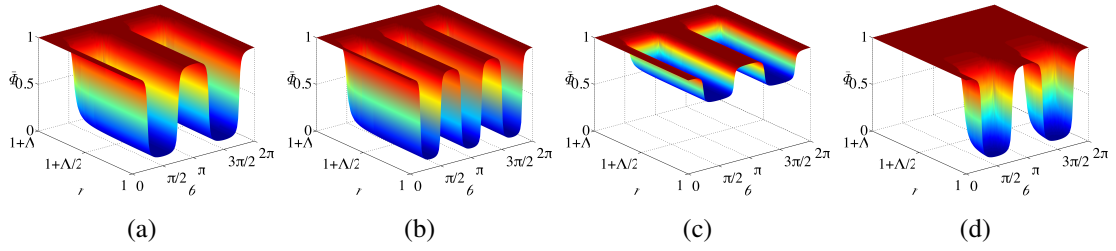


Figure 4.20: Sinusoidal permeability distributions in radial-circumferential direction corresponding to the parameters given in Tab. 4.4

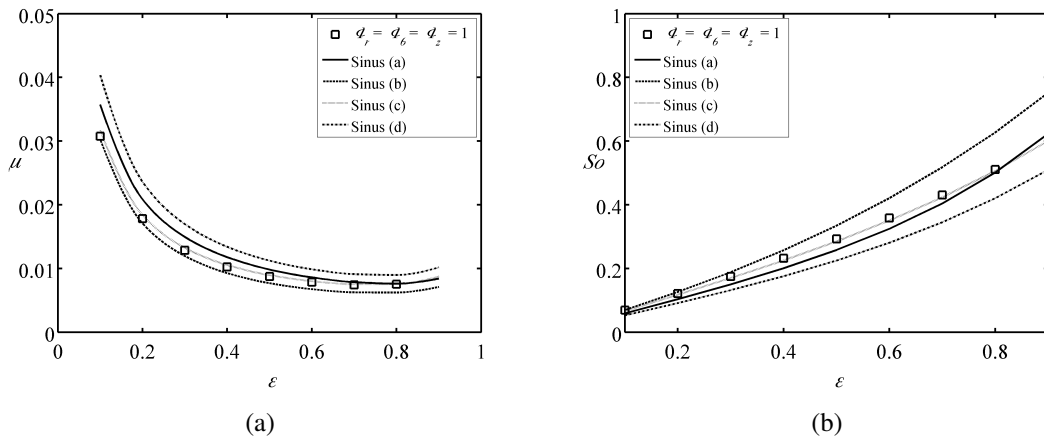


Figure 4.21: Results obtained for the sinusoidal permeability case where $K = 1$: (a) friction coefficient vs. eccentricity ratio and (b) Sommerfeld number vs. eccentricity ratio, compared to the homogeneous case

To sum up, multi-directional variations of the permeability clearly affect the frictional behaviour of porous journal bearings. Definite rules regarding which is the most advantageous distribution cannot be established, yet one can concede that a controlled permeability distribution serves in bearing design.

4.5 The case of highly permeable seat: $K \gg 1$

The theoretical background of a highly permeable thin seat, $K \gg 1, \Lambda \ll 1$, was covered in Sect. 3.6. We now solve numerically the accompanying modified Reynolds equation 3.22 following the same discretisation scheme as for the full Reynolds equation, and examine the results when the key quantity $\hat{K} = K\Lambda$ is varied.

ε	Constant		Sinus (a)		Sinus (b)		Sinus (c)		Sinus (d)	
	$K = 2$	$K = 5$	$K = 2$	$K = 5$	$K = 2$	$K = 5$	$K = 2$	$K = 5$	$K = 2$	$K = 5$
0.1	0.036	0.054	0.045	0.081	0.035	0.050	0.038	0.059	0.056	0.108
0.2	0.021	0.031	0.027	0.041	0.020	0.028	0.022	0.033	0.031	0.054
0.3	0.015	0.023	0.019	0.031	0.014	0.02	0.016	0.025	0.023	0.038
0.4	0.012	0.019	0.015	0.026	0.011	0.016	0.013	0.02	0.018	0.032
0.5	0.011	0.017	0.013	0.022	0.009	0.013	0.011	0.018	0.016	0.028
0.6	0.01	0.015	0.012	0.020	0.008	0.012	0.01	0.016	0.014	0.025
0.7	0.009	0.015	0.011	0.019	0.007	0.011	0.01	0.016	0.013	0.024
0.8	0.01	0.016	0.011	0.020	0.007	0.011	0.01	0.016	0.013	0.025
0.9	0.012	NA	0.012	NA	0.009	NA	0.012	NA	0.016	NA

Table 4.5: Friction coefficients for the sinusoidal permeability distributions for large value of the coupling parameter K

The original set of 5 governing parameters is now condensed into : $\Gamma, \varepsilon, \hat{K}, P_C$. The subsequent numerical calculations are performed for a bearing with $\Gamma = 0.9$ and $P_C = -0.01$, and an assumed constant and isotropic permeability, such that $\Phi_\theta = \Phi_z = 1$. ε takes the usual values between 0 and 1, while \hat{K} is varied sequentially from 10^{-1} to 10^2 . The outcome of this study is given in Fig. 4.22 where values of μ_n are plotted against the inverse of the Sommerfeld number So and the eccentricity ratio ε , respectively.

It results that the representation μ_n vs. $1/So$ shows the same characteristics as the curves obtained by Cameron [36] and already shown in Fig. 2.6. The curves show what Cameron et al. stated in their paper: above a certain threshold of the Sommerfeld number, So_c say, hydrodynamic lubrication cannot be sustained, and as a result friction increases abruptly. The curves in Fig. 4.22 a) show two asymptotes: they collapse onto a single straight line as $1/So$ becomes very small and reveal that μ_n varies with $(So_c - So)^{1/2}$ as the value of So approaches So_c . On the same common asymptote lies also Petroff's friction for lightly loaded bearings (see Eq. 2.17). When represented vs. ε , one remarks the asymptotic behaviour of μ_n around both $\varepsilon \rightarrow 0$ and $\varepsilon \rightarrow 1$. Due to the modified pressure coefficients in Eq. 3.22 shown in Sect. 3.6 it is possible to achieve a solution for the case $\varepsilon \rightarrow 1$. Also, the friction coefficient reaches its minimum around $\varepsilon \in [0.6, 0.75]$, which is not the case for the standard set-up.

In what concerns the occurrence of cavitation, Fig. 4.23 depicts the minimum pressure \hat{P} recorded for each combination of ε - \hat{K} . Should P_C be encountered at any point in the θ - z space, one will consider that for the specific constellation of parameters, the lubricant has cavitated. The spectrum defined by Fig. 4.23 shows that the cavitation-free region ($\hat{P} > P_C$) is comprised in the region of low eccentricities and high values of \hat{K} . For the case of an unloaded bearing $\varepsilon \rightarrow 0$ the lubricant remains in a fully liquid state regardless of the value \hat{K} attains.

In the closely related study presented in Ch.2.4, Fig. 2.6, Cameron et. al. [36] reproduced these theoretical friction curves by an analytical solution for the narrow bearing, where cavitation was neglected. A correspondingly simplified theoretical description can be obtained, allowing a fully analytical solution for the case of an infinitely long bearing and an approximative one for a finite-width porous bearing, as shown in [71] (where the same values for the key parameter Ψ are considered). In what follows, we aim at verifying Cameron and co-workers' approach.

Equation (3.22) allows for the variation of \hat{K} , which is essentially equivalent to Ψ as $\hat{K} = 12\Psi$. The permeability is taken as isotropic and homogeneous, so that $C_\theta = C_z = \text{const}$. The results of these strategies are shown in Fig. 4.24, where the theoretical results by Cameron et al. [36] are represented by straight lines, and the data obtained numerically by Sect. 3.6 are marked by dashed lines.

By comparing the two methods one can remark that the associated critical values of $1/\Delta$ appear to be largely shifted. In our approach, the curves lie closer to one another, and for the cases $\Psi \rightarrow 0$ the critical values of $1/\Delta$ almost collapse. This can be explained by the fact that at high eccentricity ratios (or for $1/\Delta \rightarrow 0$) the cavitating regime has a greater impact on the pressure distribution, especially when we consider the limit of a solid bearing, whereas the approach by Cameron et al. does not include any cavitation effects. However, a main source for the discrepancy between their and our results is the fact that the assumptions in Sect. 3.6 are incompatible with the dimensions of the industrial bearings we assumed, see Tab. 4.2. Nevertheless, the thus reduced problem, Eq. (3.22), not only drastically eases the systematic investigation of

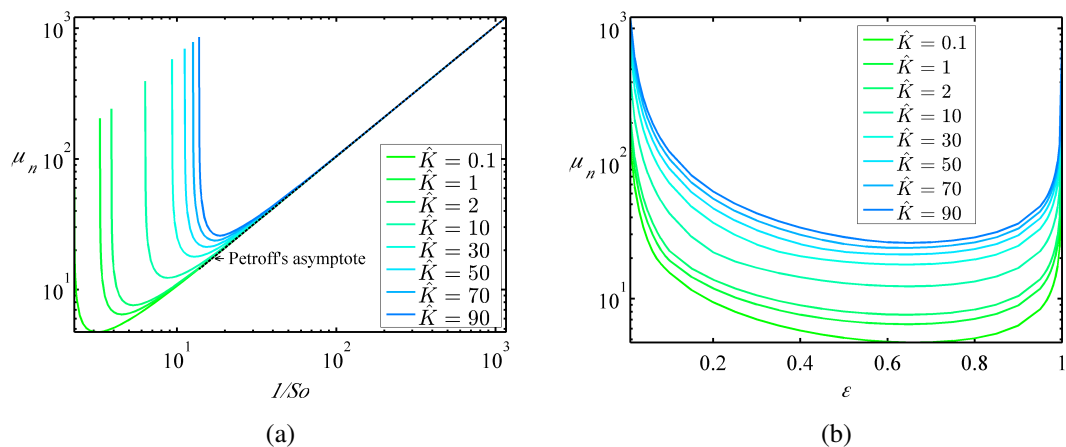


Figure 4.22: Numerical results for the case $K \gg 1$: normalized friction coefficient vs. inverse of the Sommerfeld number for: (a) distinct values of \hat{K} and (b) vs. the eccentricity ratio ε

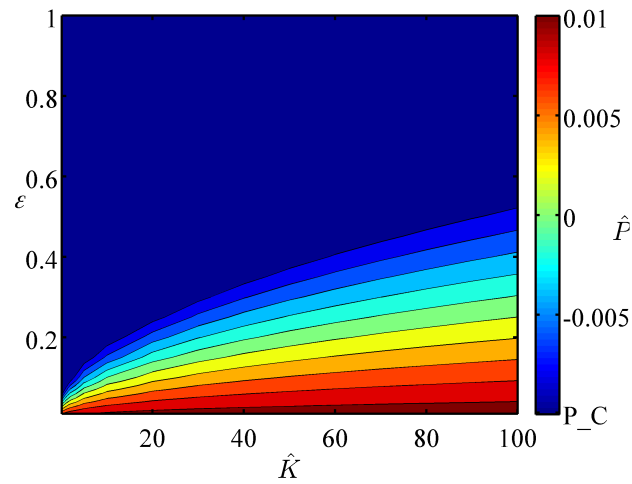


Figure 4.23: Numerical results for the case $K \gg 1$: minimum pressure in the lubricant gap \hat{P} vs. the modified coupling parameter \hat{K} and the eccentricity ratio ε

the bearing operation, but allows correct qualitative insight. For instance, the increase of the friction coefficient for a given load at increased permeability indicates the reduction of the load capacity found in tests, see, e.g., [33].

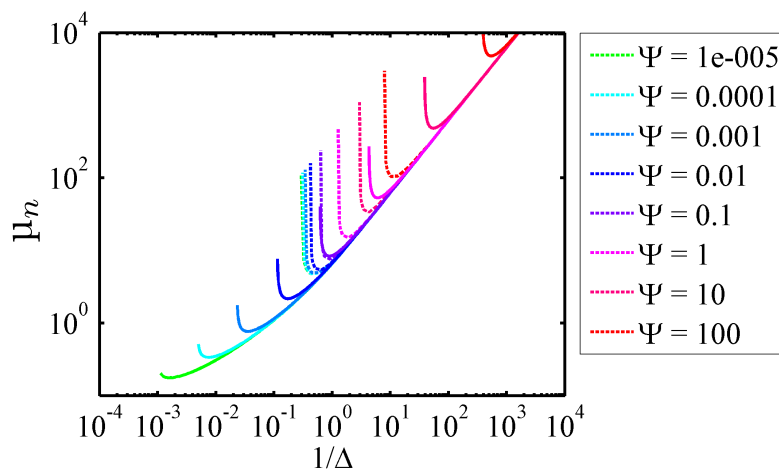


Figure 4.24: Comparison of friction coefficients calculated according to Cameron et al. [36] (continuous lines, see also Fig. 2.6) and Eq. 3.22 (dashed lines) for $\Gamma = 1$

Experimental validation of the model

The bearing behaviour predicted by the numerical simulations presented so far provides the basis for the experimental investigations within this chapter. In particular, we focus on the validation of the calculated friction coefficient by measurements based on a set of industrial bearing samples, impregnated with lubricants which differ distinctly by their nominal viscosities. As key operating conditions, the surrounding temperatures are varied, as well as both the rotational speed and loading of the bearing. The conversion between the eccentricity ratio and the applied load is made via a numerical interpolation scheme using the points stored in the database calculated in the previous chapter.

5.1 General motivation and purpose

The interest in porous bearings is reflected by the multitude of experiments available in literature. Many tests, however, were carried out on specifically designed bearings, rather than “real-life” ones. What we wish to achieve with our new in-house measurements is to evaluate industrial bearings, which, due to their geometrical imperfections stemming from the manufacturing process, increase the relative errors in measurements. Moreover, the experimental procedure should comply with real-life operating conditions, and consequently with (as much as possible) the assumptions taken by the theoretical model. Re-iterating the latter, we deal with four main idealizations on which the computation scheme is based on:

- (i) the assumption of stationary operation in a regime of predominantly hydrodynamic lubrication (neglect of pronounced mixed lubrication) throughout;
- (ii) cavitation dealt with as the emergence of a homogeneous two-phase regime of the lubricant;

- (iii) a strictly Newtonian rheology of the liquid and the partially vaporous lubricant;
- (iv) the neglect of imperfections/roughness of the seat and journal surfaces forming the gap and their associated wear (presumed run-in).

Run-in refers to the adjustment of the originally rough contacting surfaces, eventually achieving their conformal fit on the roughness scale (see [72]). Hence, running-in effects can only be simulated here by unsteady variations of the operation temperature, i.e., the viscosity of the lubricant simultaneously with those of the shaft speed at a given bearing load. Nevertheless, the comparison experiments-simulations focuses on the hydrodynamic branch of the Stribeck-type curves. In this sense, the experimental data used for the comparison with simulated results are taken after a run-in operation of 16 hrs., which proved sufficient for obtaining a periodic (quasi-static) hysteresis of the Stribeck-type curves. However, one must concede that even under the (assumed) absence of surface degradation, simulating running-in in this manner probably does not sufficiently resemble the associated real-life situation. In the same spirit, more efforts toward the understanding of quasi-static, transient, and finally even fully unsteady variations of parameters such as the lubricant temperature under correspondingly varying external conditions seem expedient. Having in mind this potential deficiency regarding issues (i) and (iii), in a first step we investigate the agreement between numerically and experimentally obtained friction coefficients for lubricants essentially distinguished by their viscosities at low to medium applied loads.

5.2 Experimental set-up and method of data evaluation

The experimental measurements were performed on a custom-made test rig for precision bearings (see Fig. 5.1). Its specific design allows the programming of a multitude of test procedures and the automatic recording and analysis of the test temperature, the shaft rotational speed, the normal load and the friction torque. The set-up is explained in the following paragraph.

With the aid of a chuck, a shaft can be (interchangeably) installed on a spindle mounted with precision roller bearings (max. concentricity deviation of 2 μm , rotational speed up to 18,000 min^{-1}). The free end of the shaft (typical diameter range 4–12 mm) is fitted with the test bearing in a holder. A torsion measurement device based on essentially frictionless air bearings integrated into the loading mechanism allows the measurement of the friction torque in the test bearing. The maximum allowed radial loading is 200 N. The bearing holder can be fitted to the bearing externally, independent of the test device, and prepared for the test run. It is compatible with numerous bearing dimensions and geometries via a set of adapters that allow simple assembly of the bearing–shaft pairing as well as installation in the test device. Variants of the

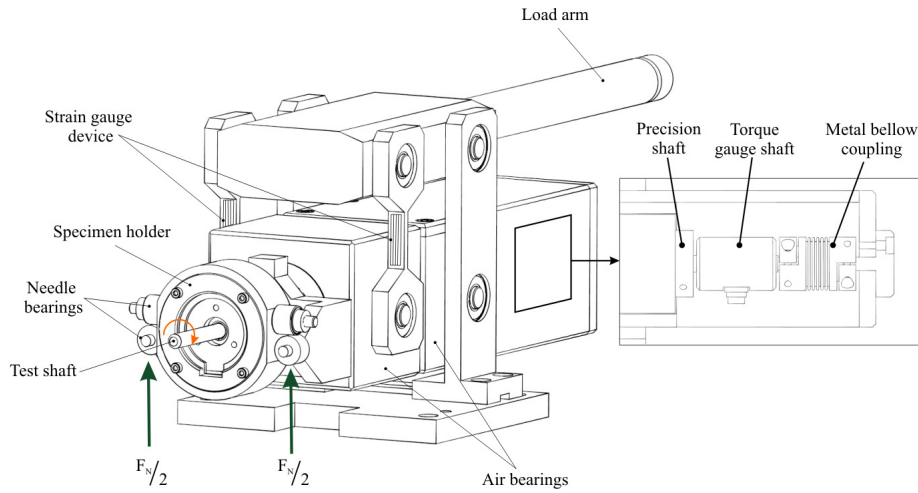


Figure 5.1: Porous bearings experimental test rig: main components

mount provide initial cooling, output-regulated heating, temperature measurement and monitoring of the lubrication conditions.

Spherical iron bearings of a uniform porosity of 20% (as specified by the manufacturer) and thus assumed uniform permeability were used. The permeability of the porous seat was measured using the method presented in [73], where on one side of the porous medium (bearing), compressed air is supplied, and the pressure drop through the medium is measured. More detailed work regarding the accuracy of the permeability value would include variations with viscosity and pressure difference, and correlations available between permeability and porosity, as already discussed in Sect. 2.2. However, since this topic is beyond the scope of this study, the values measured via the method mentioned above are considered sufficiently accurate compared to other input uncertainties used for the numerical calculations. Moreover, the local permeability entering Darcy's law is then viewed as isotropic and a scalar function of local porosity. The assumption (iv) is well supported by Fig. 2.7, shown previously in Sect. 2.2.2, where the roughness profile of a representative porous bearing is depicted. Even before operation (no run-in, new condition) an R_a -value of only $0.96 \mu\text{m}$ is measured, while after 15 hrs. of operation under a load of 1 N/mm^2 we find $R_a \doteq 0.73 \mu\text{m}$. These values account mainly for the depths of the surface pores, which are rather isolated and by a factor of about 10 smaller in diameter. However, the surface elevations, then referred to as roughness, are very smooth: their basic wavelengths are much larger than the typical pore depth, its amplitudes comparable to the typical pore diameter. A typical gap interstice of about $5 \mu\text{m}$ justifies the treatment of porosity in a homogenized manner as usual in the literature and in the underlying theoretical model. Furthermore, this shows that a typical mixed-film regime as provoked by small-scale roughness is not of concern

Sample		1	2	3	4	5	6	7	8
$\tilde{\eta}$ (40 °C)	[mm ² /s]	18	18	46	46	100	100	460	460
$\tilde{\Phi}$	[10 ⁻¹⁵ m ²]	2.9	2.74	2.8	2.83	2.89	2.96	2.89	2.97
\tilde{c}_d	[μm]	11	10.3	10.7	11	11.7	11	11	11.7

Table 5.1: Experimental matrix

Oil	PAO 18	PAO 46	PAO 100	PAO 460
a	9.09	8.31	7.84	6.99
b	3.6	3.24	3.02	2.63
f			0.7	

Table 5.2: Lubricant parameters used in the Ubbelohde-Walther relationship

here. Simultaneously, the large-scale waviness of the surface raises some doubts on the validity of presuming a regime of perfect bulk or hydrodynamic lubrication, controlled only by the nominal gap geometry.

The samples were impregnated with four polyalphaolefin (PAO) base oils of varying viscosities. For statistical reasons, each of the four lubricants was used to fill two bearing samples: the eight resulting samples are referred to as Samples 1–8 hereafter. Before performing the experimental tests, we measured the bearing and shaft diameters for each sample (by means of a calliper) in order to estimate the available clearance. The resulting experimental matrix is given in Tab. 5.1.

During the experimental tests, the temperature change in the system was measured through a thermocouple mounted on the bearing surface at a depth of 1 mm. The measured temperature was used for calculating the equivalent lubricant viscosity by applying the logarithmic relationship for Newtonian liquids introduced by Walther (see Eq.2.6 in Chapter 2.4), for which the lubricant-specific constants a and b are fixed by empirical correlations and given in Tab. 5.2.

Since $\tilde{\rho}$ is known, one so obtains the rotational speed–temperature relationship ($\tilde{\omega}$ – \tilde{T}) used in the numerical calculations and the method outlined above, which makes it possible to build up the system of non-dimensional parameters. Such typical values are given in Tab. 5.3 for the bearing Sample 1 and the lubricant viscosity taken at 3000 min⁻¹.

An approach based on the non-dimensionalisation cf. Sect. 3.4 pursued in the following eases the evaluation of experiments by the numerical analysis in a systematic manner: first, the limitations and characteristics of the bearing operation under the assumptions made are treated accurately by a directed variation of the five parameters on

\tilde{r}_s [mm]	\tilde{l} [mm]	$\tilde{\lambda}$ [mm]	$\tilde{\omega}$ [min ⁻¹]	\tilde{p}_c [Pa]	\tilde{p}_{ref} [MPa]
4.0	11.0	3.75	3000	10 ⁻³	20.8
	Γ	Λ	K	P_C	
	0.5289	0.9375	0.8367	-0.0048	

Table 5.3: Typical values of non-dimensional groups for test configuration Sample 1

the governing the system; secondly, a strategy to approximate the imposed load in terms of So and reproduce the testing conditions (prior to the calculation) is developed. The numerical steps required for this end are envisaged next.

The validation of the numerical simulations consists of comparing the calculated values of μ with measured ones. These can be obtained as the output of Eq. 3.8, rewritten in the form:

$$[\mu, \varepsilon] = [F_a, F_b](\Gamma, \Lambda, K, So, P_C), \quad (5.1)$$

an empirical relationship “modelling” the experiment with the dependent variables serving as input quantities and thus to be evaluated by the testing procedure in a straightforward manner. However, some preparatory steps have to be performed so that the results can also be replicated numerically, according to the underlying theoretical model: the simulations employ the eccentricity ε as the central input parameter (its values are varied conveniently between 0 and 1) and give So , which represents the applied load \tilde{w} , and μ as an output (via integration of the pressure \tilde{p} and the shear stresses acting on the shaft). That is, Eq. 5.1 is only manageable in inverted form, then to be evaluated numerically by means of an efficient interpolation scheme.

More precisely, for a sufficiently large set of values of the physical input parameters relevant to the bearings considered, the equivalent 4 non-dimensional parameters Γ , Λ , K , and P_C (which only varies weakly) were calculated in Sect. 4.3. An accordingly large number of simulations generated the corresponding values of So , and the data points referring to those five quantities were stored in a database. The latter has to be large enough to not only cover all configurations of interest here but also allow for a sufficiently accurate (with respect to the method of data interpolation described below) estimate of the value of So that corresponds to a targeted value of \tilde{w} . For a given configuration described by values of the last four parameters and those of So neighbouring the targeted one, we look up all the associated values of ε . Interpolating these accordingly gives a new value of ε , feeding into a further simulation run that finally yields a value of So to be compared with the targeted one. Our experience is that they differ by no more than 5%, so further iterations by additional runs are only required in extreme situations referring to points in the five-parameter space close to its boundary. In this manner, μ is calculated with satisfactory accuracy for a given load, according to Eq. 5.1.

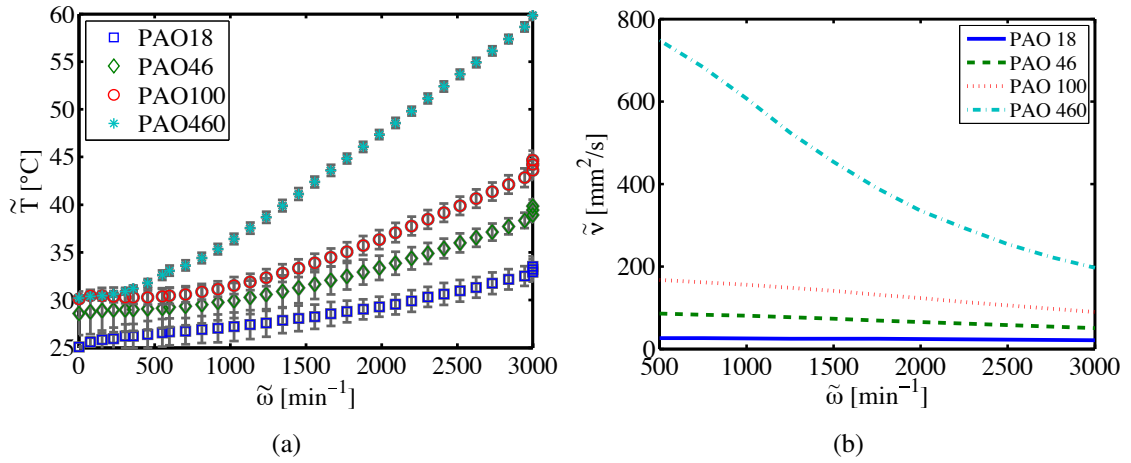


Figure 5.2: (a) Measured temperatures during experiments under a bearing load of 100 N and (b) the equivalent kinematic viscosities using the Ubbelohde–Walther equation for the same configuration

5.3 Results and Discussion: Simulations versus Experiments

Both the dynamic and kinematic viscosities of the selected lubricants cover a wide range of values. For this reason, we expect markedly different thermal behaviour from one lubricant to another. A representative graph of such a temperature variation is shown in Fig. 5.2 a), where the lubricant temperature is plotted over the rotational speed $\tilde{\omega}$ (specifically, the acceleration ramp during one Stribeck standard run as described above) and for an applied load of 100 N. The marker points represent average values between consecutive measurements of the same configuration, and the error bars are symmetric distributions of the standard deviation error calculated from the results for the two different samples. The temperature of the lubricant with the lowest viscosity (PAO 18) remains almost constant, while the most viscous lubricant (PAO 460) shows an increase of approximately 30°C. By applying Eq. 2.6 we can now estimate the variation of the viscosity with the rotational speed, and visualize the results in Fig. 5.2 b). Since the error of temperature measurements is so small, it is not replicated in the viscosity data. As expected, a variation of 5°C between the start and the end of the experiment (e.g. for PAO 18) will not have a major effect on the viscosity. However, in the case of PAO 460 the viscosity changes dramatically.

By applying the interpolation technique described above and including the temperature variation, we are able to obtain the main input required by the simulations which follows the operating conditions, namely the eccentricity ratio. Its variation over the

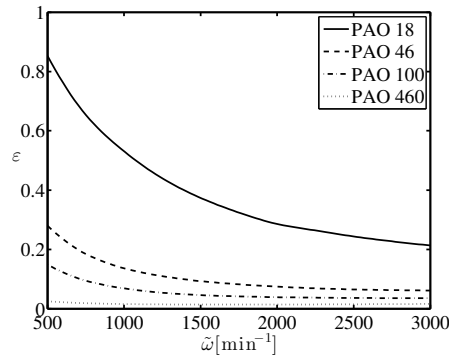


Figure 5.3: Interpolated eccentricity ratios over rotational speed for a constant load of 100 N.

rotational speed for a fixed load of 100 N is shown in Fig. 5.3. As expected, very thin lubricants operate at higher eccentricity ratios as they cannot support the applied load as well as thicker ones do. Again, the small error of measuring the temperature that propagates into the viscosity data entering the simulation and therefore the interpolation scheme is not taken into account.

5.3.1 Comparison with full simulations

The minimum value for $\tilde{\omega}$ used in the numerical calculations was chosen such that an appropriate comparison between experimentally and computationally obtained results should take into account only points that refer to a well-marked hydrodynamic regime. During a Stribeck run, the transition from the usual start-up mixed-lubrication regime to the hydrodynamic one occurs at low rotational speeds, with the exact value varying with the operating conditions and bearing type. Porous bearings can generally be assumed to have well-calibrated surfaces, which is also reflected in the roughness profiles in Fig. 2.7, so we estimate that surface roughness plays a minor role in the lubrication process. By realistically assuming a relatively fast transition to the hydrodynamic regime, we calculate the Stribeck curves over a range of 500–3000 min^{-1} .

Figure 5.4 shows the comparison between the friction coefficient μ obtained for the two sets of data, plotted over the rotational speed $\tilde{\omega}$. The experimental data points are depicted as markers, distinct for each load, and represent averaged values of six measurements: three repetitions for each of the two samples impregnated with one of the four oils. Each averaged data point is accompanied by an error bar of the standard deviation between these six measurements, and the average values of the standard deviation is given in Tab. 5.4. The lines represent the numerically calculated friction coefficients.

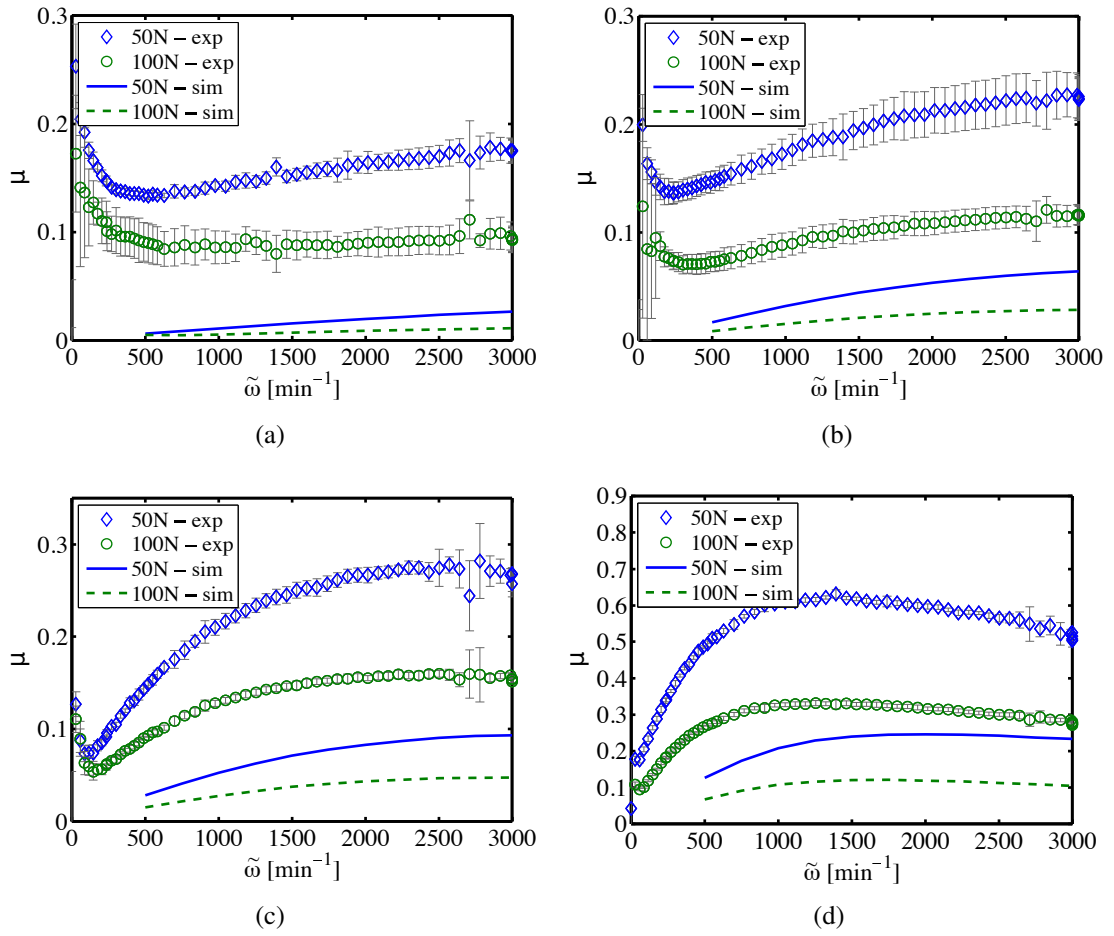


Figure 5.4: Stribeck curves for the lubricants (a) PAO 18, (b) PAO 46, (c) PAO 100 and (d) PAO 460. Markers represent experimentally obtained values, while lines depict numerical results. Error bars accompany each measured point, with the mean standard deviation for each configuration given in Tab.5.4

Configuration	PAO 18		PAO 46		PAO 100		PAO 460	
	50 N	100 N	50 N	100 N	50 N	100 N	50 N	100 N
SD_{mean}	0.0088	0.0164	0.0144	0.0108	0.0093	0.0054	0.0085	0.0054

Table 5.4: Mean standard deviation (SD_{mean}) for each tested configuration

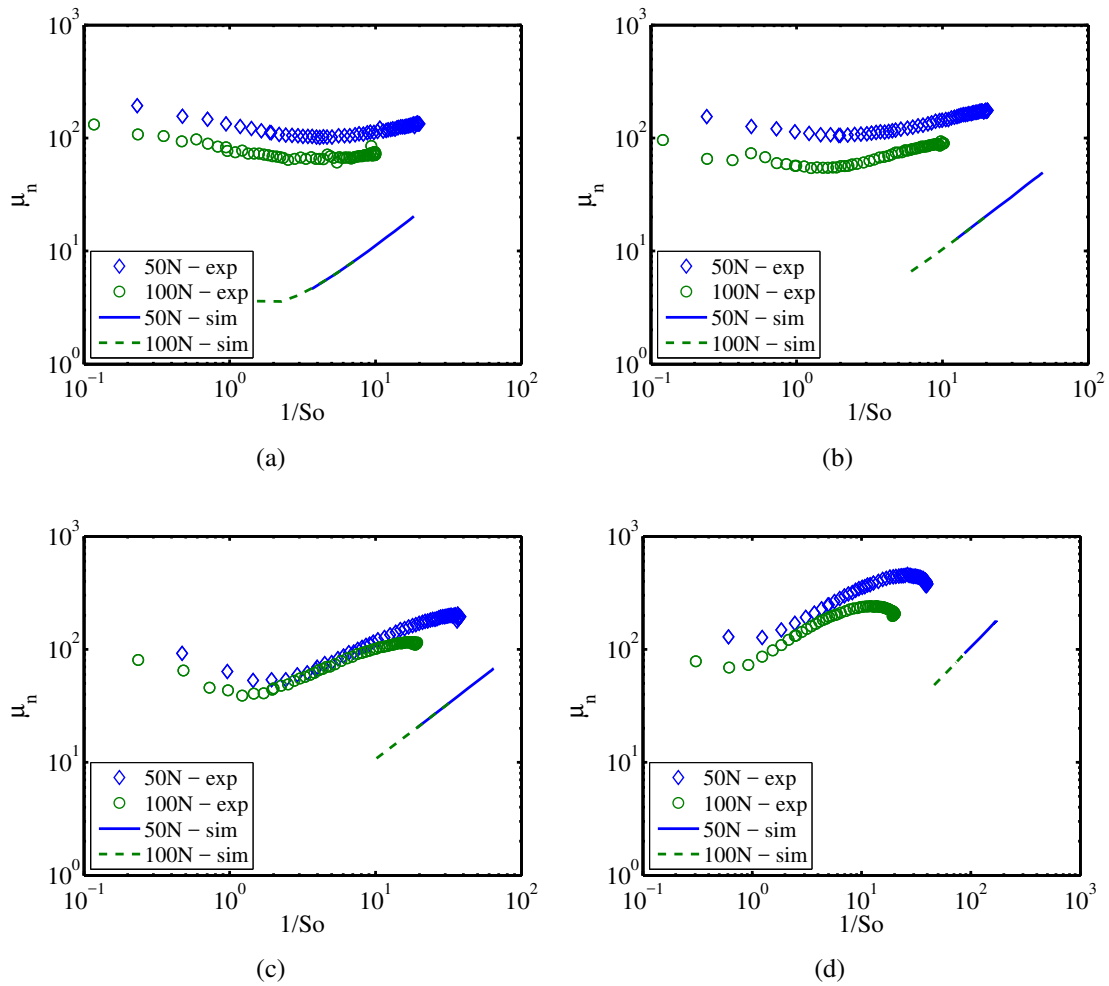


Figure 5.5: Normalized friction coefficients vs. the reciprocal Sommerfeld number for the lubricants (a) PAO 18, (b) PAO 46, (c) PAO 100 and (d) PAO 460. Markers represent experimentally obtained values, while lines depict numerical results

Let us first look at the curves representing the experimental data for increasing rotational shaft speed. In the case of PAO 18, the rather mild increase of the friction coefficient starting at the beginning of the test phase (500 min^{-1}) corresponds to a regime where mixed friction still prevails, although classically one already expects developed hydrodynamic lubrication here. This reflects partial and unsteady contact between the shaft and the bearing, in agreement with our conclusions drawn from the surface measurements and affecting the description of lubrication on the scales given by the nominal geometry. For more viscous lubricants (PAO 46, PAO 100), it appears that the points in the same region are characterized by better separation of the surfaces, even from the beginning of the test run on, so that the effect of mixed lubrication is drastically reduced. Finally, the viscosity of PAO 460 is sufficiently high to support the applied load by increasing the friction coefficient according to a pronounced hydrodynamic regime. These observations are valid at both loads for all the lubricants.

Higher loads result in lower friction coefficients, meaning a better performance of the selected bearings. The minimum/maximum values for all μ -data sets in Fig. 5.4 appear to correspond to 500 and 3000 min^{-1} , respectively, except in the case of PAO 460. There the maximum of μ is located around 1500 min^{-1} and is followed by a slight decrease with increasing $\tilde{\omega}$. This is explained as follows: after 1500 min^{-1} , the temperature in the oil continues to increase, which corresponds to a decrease in viscosity. Thus the lubricant in the pores is thinned, promoting its exchange between the gap and the bush and subsequently lubrication, ultimately lowering the friction coefficient. Along with the other trends found experimentally, this particular one is reproduced well by the calculated data. However, since the model (currently) does not include (possible) non-Newtonian thinning, this specific reduction of μ_n is less pronounced.

Even if we expected that the simulated results produce lower friction coefficients as they rely on the assumption of perfect hydrodynamic lubrication, they are considerably lower than the experimentally obtained ones. This offset between the two sets of data is present throughout, and it does not appear to change with viscosity or the applied load. The same offset is visible even when we plot the Stribeck curves for the same data in the classical non-dimensional manner with the Stribeck number $1/S_o$ as the abscissa: see Fig. 5.5. The curves obtained numerically collapse onto one line, which only states that μ_n is a function of S_o solely for a fixed bearing geometry and a given oil. Its validity assesses the conditions under which the Stribeck curve can be viewed as universal and other effects discarded so far are insignificant. Consequently, the discrepancy as quantified by the offsets (having a pronounced constant contribution) is due to physical effects apparently not taken into account in the simulations and the dimensional analysis rather than only due to uncertainties in the input data. The aforementioned kind of persistent “background” mixed lubrication is definitely a candidate phenomenon for explaining the offsets.

We draw the following conclusions: perfect hydrodynamic lubrication is never fully established; the associated regime in the Stribeck curves matches that of typical mixed lubrication for sufficiently small Stribeck numbers; the regime of elastohydrodynamic lubrication is shifted to even much smaller ones. However, our concern in this study is with the first regime only.

We are now interested in determining which type of correlation exists between experimental friction coefficients μ_{exp} and the simulated ones μ_{sim} . For this reason, for each set of data we extract five values of μ taken at distinct rotational speeds $\tilde{\omega} = 1000, 1500, 2000, 2500, \text{ and } 3000 \text{ min}^{-1}$ for all the bearing samples and both loads (50 N, 100 N). In this way we obtain 90 points, which are represented in Fig. 5.6. The majority of points rests on a band-type cluster that marks a definite correlation between the two data sets. The large experimental values of PAO 460 at 50 N are isolated from all the other points. Using Pearson's product-moment correlation coefficient [74], we find that the correlation coefficient is 0.9239. Even if the data points are strongly correlated, the discrepancy between the two data sets cannot be neglected. Below we present the possible reasons for these deviations.

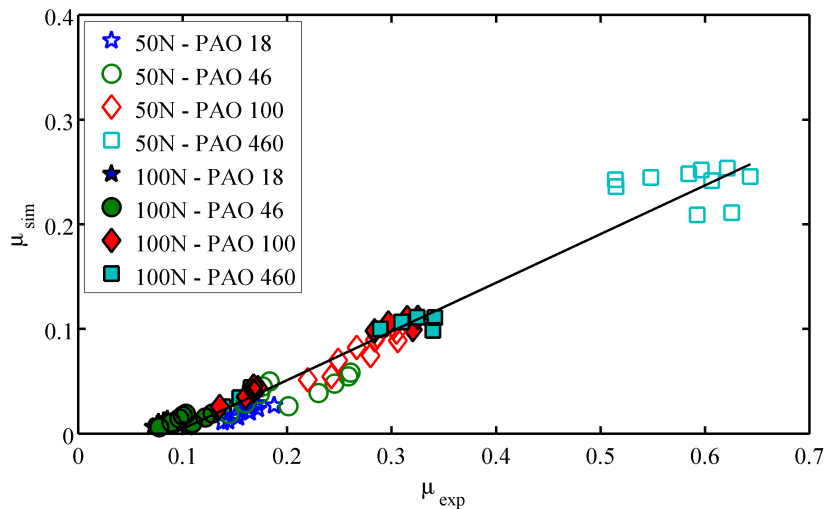


Figure 5.6: Correlations between measured μ_{exp} - and calculated μ_{sim} -values for the friction coefficients. Temperature: 25°C.

Perfect agreement between simulation and experimental data is usually very difficult to achieve. There are many influences that can affect the course of an experimental test. First, the accuracy of the geometrical properties of the samples cannot be guaranteed: the value of the sinter permeability is measured under standard conditions for air, yet the oil may exhibit a different behaviour mostly due to capillary effects for a partially

\tilde{r}_b	\tilde{l}	$\tilde{\lambda}$	\tilde{c}	$\tilde{\Phi}$	$\tilde{\eta}$ (40°C)	$P \times V$
[m]	[m]	[m]	[μm]	[m^2]	[Pa s]	[$\text{N}/\text{mm}^2 \times \text{m}/\text{s}$]
0.0095	0.0254	0.003	20.3	6.24×10^{-14}	0.12	0.08

Table 5.5: Input parameters for the measurements performed by Cameron et al. [36]

saturated matrix when considered under real-life conditions. Also, a non-homogeneous permeability distribution in the sinter (much larger circumferential or axial components than the radial one) can affect the friction behaviour. Any manufacturing imperfection of the sample has a more pronounced effect during measurements in small bearings, such as the ones used here, rather than in larger ones. Secondly, thermal effects have not been considered. After a 16-hour running-in of the samples, where the temperature increased and decreased successively, the value of the clearance measured before the test may have changed. The final point, but possibly the one with the highest impact, is the question whether the bearing and the shaft are not perfectly aligned. In this case, the lubrication film does not extend along the whole length of the bearing, and at one side of the bearing the clearance is much smaller than on the other. This produces an additional torque in the system. Nevertheless, misalignment does not necessarily mean direct contact of the surfaces. If that were the case, an uneven wear mark would be seen on the bearing surface.

5.4 Comparison with established theoretical/empirical results

An extension of the validation is performed by comparing simulated data with experimental results available in literature. For this purpose we have selected the data obtained by Cameron and co-workers [19,36]: they tested sintered iron bearings exhibiting a controlled porosity. There the experimental technique was to maintain the product between the applied load per unit area ($P = \tilde{w}/(\tilde{r}_b\tilde{l})$) and speed ($V = \tilde{\omega}\tilde{r}_b$) at a constant level ($PV = \text{const}$). The starting speed $\tilde{\omega} = 720 \text{ min}^{-1}$ was decreased to $\tilde{\omega} = 50 \text{ min}^{-1}$ while the load was progressively increased from $\approx 30 \text{ N}$ to $\approx 420 \text{ N}$. The authors mention that this procedure led to a steady temperature increase of 15°C above room temperature, which we can assume would lead to a constant lubricant viscosity. Moreover, in order to ensure that the lubrication gap remains filled with enough oil, the bearing was supplied with oil from an external source. The experimental parameters are given in Tab. 5.5.

Figure 5.7 shows the results of this comparison where μ_n from Eq. 2.19 is plotted over the inverse of the Sommerfeld duty parameter Δ , see Eq. (2.19). One can clearly

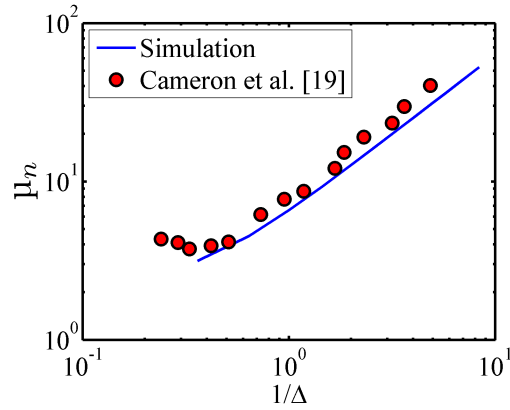


Figure 5.7: Friction curve obtained experimentally by Cameron et al. [36] vs. numerical calculations for the same configuration

see that the two sets of data agree well. The lower part of the graph corresponds to high loads and low rotational speeds, a more sensitive configuration for the numerical calculations, and therefore the true minimum of $1/\Delta$ cannot be achieved.

Cameron et al. [36] obtained excellent agreement between *their* experimental results and a theoretical approach they obtained by applying a certain correction factor (see results in Sect. 4.5), yet this value was found by examining solid bearings, a procedure which apparently must be seriously questioned here. On the other hand, our full, i.e., finite-width, calculations do not imply any additional approximations, yet they predict distinct trends with likewise good agreement when compared to the two sets of experimental data (in-house measurements by Cameron et al., cf. Fig. 5.7). Here one must first take into account that *their* experimental technique was different from the one taken up in the present study. As a result, a steady temperature increase was obtained, unlike the observed increase in our measurements. Secondly, even in the case of bearing similarity (i.e., similar aspect ratios), the samples considered in literature are large, whereas our in-house measurements are performed on small industrial/real-life bearings. Such small geometries are more sensitive to relative geometrical errors and uncertainties concerning the test rig. During operation, any misalignment between the shaft and the bearing will accentuate the deviation from the ideal full hydrodynamic regime. However, this cannot be checked beforehand in our experiments. Finally, the continuous supply of oil in Cameron and co-workers' experiments ensures a well-lubricated gap but definitely does not correspond to the majority of real-life operating conditions of porous bearings.

CHAPTER 6

Conclusions

A new mass-conservative model for predicting vaporous cavitation in sintered bearings was presented. The governing equations were solved numerically, and the results were ultimately compared with experimental data. Since measurements of the phenomenon of cavitation are scarce in literature, we resorted to validating our model by comparing simulated friction coefficients with measured ones. Altogether, we believe that our contributions to the subject can be distinguished as follows:

Theoretical contribution: The adopted description of the cavitation development is consistent with the particular way of operation of porous journal bearings, where vaporization appears to be the mechanism which triggers the film discontinuity. The two-phase mixture describing the cavitation region is governed by the lubricant saturation. All relevant physical processes are taken into account by an appropriate coupling between the steady state Reynolds equation and Darcy flow, with the specification that both the onset of cavitation and film reformation are to be described by the Jakobsson-Floberg-Olsson condition. We believe that this approach was sufficient for capturing the essential phenomena occurring in a sintered bearing, without oversimplifying the process and considering the length scales involved in such a system. Furthermore, the resulting non-dimensional parameters characterizing the lubrication problem proved to be very useful not only to the numerical analysis but also to the experimental validation.

Numerical contribution: In contrast with other approaches, the proposed numerical scheme required relative little computational effort and time, yet was able to overcome the sudden change in pressure at the point of cavitation inception. By using an artificial pressure-density relation controlled by an *annealing* parameter we could reduce the compressibility to a desired level while by parametrizing the relation we were able to obtain a stable and fast converging numerical scheme. The results gathered from the numerical calculations are, among others, the lubrication pressure and saturation, friction coefficient and load bearing capacity. The parameter range that could be studied

via the proposed numerical scheme was rather large, hence an effective approach was to build a structured database which could be analysed in a more systematic manner. The lack of points in the database indicated the specific conditions, or the combinations of parameters which could not be calculated, or for which a converged solution was not obtained.

Plotting the friction coefficient versus the eccentricity ratio showed the effect of cavitation, namely of a reduction in friction coefficient due to the reduced pressure in the cavitation region. Also, plots of the Sommerfeld number versus the eccentricity ratio indicated, from the design point of view, which geometrical aspect ratios give the best results. A very thick/thin bearing seat does not show any visible impact of the frictional behaviour, possibly due to the very simple model of percolation through porous media of the Darcy law. On the other hand, very long bearings have a much higher load bearing capacity than the shorter ones. By numerical simulations we were able to predict the threshold in the eccentricity ratio below which cavitation does not occur. Furthermore, an interesting behaviour was observed in the cases of high loads and high values of the coupling parameter: an apparent increase in the friction number, unlike the decreasing trend observed previously. Without a doubt the most notable finding of the numerical simulation is the fact that at the point of recondensation, a saturation jump occurs. A more detailed look into the behaviour of the saturation under various combinations of parameters revealed that the observed jump is greatly attenuated for very high coupling parameters.

Varying the permeability of the porous seat yielded promising results insofar as controlling the spatial distribution of the grains (and thus the permeability) alters the frictional behavior, even if only for certain configurations. The studied profiles show that a non-homogeneous permeability is of greater importance in cases where the bearing operates under lower loads.

Experimental contribution: We performed tests in order to assess the Stribeck curves of porous journal bearings, originally obtained by numerical simulations, through varying the key parameters that characterize the steady-state performance of the bearings.

To this end, a previously unappreciated systematic evaluation of the Stribeck relationship by dimensional analysis was carried out. It results that the sought quantities characterizing the lubrication problem can be expressed in terms of five independent non-dimensional quantities. This procedure eased the construction of a vast database of calculated points from which a targeted eccentricity ratio could be extracted by interpolation.

The qualitative comparison between the experimental data and the numerical ones showed strong correlations between the data points, though an observed offset seems to be present in all configurations, which interestingly is almost independent of the applied load, operating speed, or lubricant used. On the other hand, highly encouraging results were obtained when calculations are compared with results found in literature.

Finally, a database that was initially small, yet appropriate for moderate loads and corresponding eccentricities, could be dynamically increased via the terminal simulation runs required by the interpolation technique to provide an efficient way for refining the latter in terms of accuracy. This is definitely useful for future efforts. The following issues are identified as the potential main sources for the observed discrepancy between calculated and measured friction coefficients for a given bearing, lubricant, and load. They should therefore deserve primary attention in a revised simulation model (numbers indicate priority):

- (1) mixed lubrication, corroborated by the measurements of the surface topography;
- (2) the possible shaft/seal misalignment should be accounted for in terms of a genuine three-dimensional rather than axially aligned gap geometry;
- (3) non-Newtonian effects such as shear-thinning (for sufficiently high rotational speeds) and piezo-viscosity (less likely here than for very high loads);
- (4) a possibly underestimated degree of anisotropy of the porosity and hence the permeability, due to the manufacturing process, could provide an additional cause.

Notational conventions

Dimensionless quantities are used throughout the thesis, as they conveniently parametrise the employed equations and simplify the analysis. To differentiate between non-dimensional and dimensional, the latter are marked by the use of tilde ($\tilde{}$). Non-dimensional groups (and quantities) are predominantly, written in upper-case characters. The symbols and notations used in this work are given below in the Nomenclature section.

Nomenclature

\tilde{c}	Radial clearance between shaft and bearing	(m)
\tilde{d}	Bearing diameter	(m)
\tilde{e}	Bearing eccentricity	(m)
\tilde{f}_f	Friction force in the lubrication gap	(N)
g	Cavitation index	
\tilde{h}	Fluid film thickness	(m)
H	Non-dimensional film thickness	
\tilde{h}_{min}	Minimum film thickness	(m)
i	Iteration step	
\tilde{l}	Bearing width	(m)
\tilde{m}_f	Bearing frictional torque	($N \cdot m$)
\tilde{p}	Pressure in the fluid film	(Pa)
p	Number of possible independent non-dimensional groups in an equation	
\tilde{p}_{cav}	Cavitation pressure	(Pa)
\tilde{p}_d	Darcy pressure through the sinter matrix	(Pa)
P_D	Non-dimensional Darcy sinter pressure	
\tilde{p}_r	Reynolds lubricant pressure in the gap	(Pa)
P_R	Non-dimensional Reynolds lubrication pressure	

\tilde{p}_{ref}	Lubricant reference pressure	(Pa)
\hat{P}	Non-dimensional gap pressure for the case $K \gg 1$	
\tilde{r}_b	Bearing inner radius	(m)
\hat{r}	Re-scaled coordinate for the case $K \gg 1$	
\tilde{r}_s	Shaft radius	(m)
r, θ, z	Cylindrical coordinates	
S	Lubricant saturation	
S_a	Specific area of porous medium	(m ²)
\tilde{t}	Surface tension of liquid	(N/m)
\tilde{T}	Temperature	(K)
$\tilde{u}, \tilde{v}, \tilde{w}$	Fluid velocity in $\tilde{x}, \tilde{y}, \tilde{z}$ coordinates, respectively	(m/s)
$v_{D,r}$	Inflow of lubricant from the sintered seat	
V	Sliding speed of shaft	(m/s)
\tilde{w}	Applied load	(N/m ²)
\tilde{w}_x, \tilde{w}_y	Force per unit width	(N/m ²)
x_l	Mass fraction of the liquid phase	
$\tilde{x}, \tilde{y}, \tilde{z}$	Cartesian coordinates	(m)
α_l	Volumetric fraction of the liquid phase	
β	Artificial compressibility	
β_l	Bulk modulus of the lubricant	(Pa)
$\Delta\theta, \Delta z$	Mesh spacing in θ and z directions, respectively	
$\tilde{\eta}$	Dynamic viscosity of the fluid	(Pa · s)
ε	Bearing eccentricity ratio	
$\tilde{\lambda}$	Bearing wall thickness	(m)
μ	Bearing friction coefficient	

μ_{exp}	Experimental (measured) friction coefficient	
μ_n	Normalized friction coefficient	
μ_{sim}	Calculated (simulated) friction coefficient	
$\tilde{\nu}$	Kinematic viscosity of the fluid	(m^2/s)
$\tilde{\omega}$	Shaft rotational speed	(min^{-1})
Φ	Permeability tensor	
ϕ	Characteristic porosity	
ψ	Bearing attitude angle	
$\tilde{\varphi}$	Permeability of porous medium	(m^2)
$\Pi_{1,2,\dots,p}$	Independent non-dimensional groups, <i>Pi-groups</i>	
$\tilde{\Phi}_{ref}$	Reference permeability	(m^2)
$\Phi_{r,\theta,z}$	Non-dimensional permeability directional components	
$\tilde{\rho}$	Fluid density	(kg/m^3)
ϱ	Under-relaxation factor	
$\tilde{\rho}_l$	Density of liquid phase	(kg/m^3)
$\tilde{\rho}_m$	Mixture density	(kg/m^3)
$\tilde{\rho}_v$	Density of the vapour state	(kg/m^3)
θ^*	Fractional film content	
φ	Fraction of the gap carrying the liquid lubricant	
u	Machine precision ($= 2.2 \cdot 10^{-16}$ in MATLAB)	
u_c	Numerical tolerance of the calculation	

Dimensionless groups

\hat{K}	Governing parameter for the case $K \gg 1$, $= K \cdot \Lambda$
B	Bearing diameter-to-length ratio $\frac{2\tilde{r}_b}{\tilde{l}}$

Δ	Sommerfeld number $\frac{\tilde{w}}{\tilde{\eta}\tilde{u}\tilde{l}} \frac{\tilde{c}}{\tilde{r}_b^2}$
ϵ	Aspect ratio of the gap \tilde{c}/\tilde{r}_b
ε	Eccentricity ratio $\frac{\tilde{e}}{\tilde{c}}$
Γ	Bearing aspect ratio $\left(\frac{2\tilde{r}_s}{\tilde{l}}\right)^2$
K	Permeability parameter $12\tilde{\Phi}_{ref} \frac{\tilde{r}_s}{\tilde{c}^3}$
Λ	Bearing thickness ratio $\frac{\tilde{\lambda}}{\tilde{r}_s}$
P_C	Cavitation pressure $\frac{\tilde{p}_c}{\tilde{p}_{ref}}$
Ψ	Bearing design parameter $\frac{\tilde{\Phi}\tilde{\lambda}}{\tilde{c}^3}$
Re	Reynolds number $\frac{\tilde{u}\tilde{l}}{\tilde{\nu}}$
So	Sommerfeld number $\frac{\tilde{w}}{\tilde{p}_{ref}\tilde{r}_s\tilde{l}}$
St	Stribeck number $\frac{\tilde{u}\tilde{\eta}}{\tilde{w}}$

Bibliography

- [1] S. A. Tsuckermann, *Powder Metallurgy*. Oxford: Pergamon Press, 1965.
- [2] V. Kumar, "Porous metal bearings — A critical review," *Wear*, vol. 63, pp. 271–287, Sept. 1980.
- [3] M. J. Braun and W. M. Hannon, "Cavitation formation and modelling for fluid film bearings: a review," *Proceedings of the Institution of Mechanical Engineers, Part J: Journal of Engineering Tribology*, vol. 224, pp. 839–863, Jan. 2010.
- [4] B. Jakobson and L. Floberg, "The finite journal bearing considering vaporization," *Transactions of Chalmers University Technology, Göteborg, Sweden*, vol. 190, pp. 1–119, 1957.
- [5] K. Olsson, *Cavitation in dynamically loaded bearings*, vol. 308. Göteborg: Tech., Trans. Chalmers Univ., 1965.
- [6] H. G. Elrod, "A Cavitation Algorithm," *Journal of Lubrication Technology*, vol. 103, p. 350, July 1981.
- [7] D. E. Brewe, "Theoretical modeling of the vapor cavitation in dynamically loaded journal bearings," *J. Tribol.*, Jan. 1986.
- [8] D. Vijayaraghavan and T. G. Keith, "Development and Evaluation of a Cavitation Algorithm," *Tribology Transactions*, vol. 32, pp. 225–233, Jan. 1989.
- [9] M.-H. Meurisse and B. Giudicelli, "A 3D Conservative Model for Self-Lubricated Porous Journal Bearings in a Hydrodynamic Steady State," *Journal of Tribology*, vol. 121, pp. 529–537, July 1999.
- [10] J. Field, "David Tabor. 23 October 1913 – 26 November 2005," *Biographical Memoirs of Fellows of the Royal Society*, vol. 54, pp. 425–459, Dec. 2008.
- [11] R. S. Porter and J. F. Johnson, "Viscosity performance of lubricating base oils at shears developed in machine elements," *Wear*, vol. 4, pp. 32–40, Jan. 1961.

- [12] A. Crouch, R. F. , Cameron, “Viscosity-temperature equations for lubricants,” *Journal of the Institute of Petroleum*, vol. 47, pp. 307–313, 1961.
- [13] R. Stribeck, “Kugellager für beliebige Belastungen,” *Zeitschrift des Vereins Deutscher Ingenieure*, vol. 45, 1901.
- [14] R. Stribeck, “Die wesentlichen Eigenschaften der Gleit- und Rollenlager,” *Zeitschrift des Vereins Deutscher Ingenieure*, vol. 46, 1902.
- [15] O. Reynolds, “On the Theory of Lubrication and Its Application to Mr. Beauchamp Tower’s Experiments, Including an Experimental Determination of the Viscosity of Olive Oil,” *Philosophical Transactions of the Royal Society of London*, vol. 177, pp. pp. 157–234, 1886.
- [16] A. Sommerfeld, “Zur hydrodynamische Theorie der Schmiermittelreibung,” *Zeit. Math. Phys.*, vol. 50, pp. 97—155, 1904.
- [17] N. Petroff, “Theoretical and experimental study of mediate friction,” *The Engineer*, 1883.
- [18] W. L. Cameron, A., Wood, “The full journal bearing,” *Proceedings of the Institute of Mechanical Engineers*, vol. 161, pp. 59–64, 1949.
- [19] V. T. Morgan and A. Cameron, “Mechanism of lubrication in porous metal bearings,” *Proc. Conference on Lubrication and Wear*, pp. 151–157, 1957.
- [20] V. T. Morgan, “Hydrodynamic porous metal bearings,” *Lubrication Engineering*, pp. 448–455, 1964.
- [21] H. Darcy, *Les fontaines publiques de la ville de Dijon : exposition et application des principes à suivre et des formules à employer dans les questions de distribution d’eau*. V. Dalmont (Paris), 1856.
- [22] A. Scheidegger, “The physics of flow through porous media,” 1974.
- [23] T. Vibert, “Les gisements de bauxite de l’Indochine,” *Genie Civil*, vol. 115, no. 84, 1939.
- [24] A. L. LeRosen, “A Method for Standardization of Chromatographic Analysis 1,” *Journal of the American Chemical Society*, vol. 64, pp. 1905–1907, Aug. 1942.
- [25] S. Whitaker, “Flow in porous media I: A theoretical derivation of Darcy’s law,” *Transport in Porous Media*, vol. 1, no. 1, pp. 3–25, 1986.
- [26] J. Kozeny, “Über kapillare Leitung des Wassers im Boden,” *Sitzungsbericht der Akademie der Wissenschaften, Wien*, vol. 136(2a), pp. 271–306, 1927.

- [27] E. C. Childs and N. Collis-George, "The Permeability of Porous Materials," *Proceedings of the Royal Society A: Mathematical, Physical and Engineering Sciences*, vol. 201, pp. 392–405, Apr. 1950.
- [28] C. Cusano, "Lubrication of Porous Journal Bearings," *Journal of Lubrication Technology*, vol. 94, p. 69, Jan. 1972.
- [29] S. Kaneko, Y. Hashimoto, and H. I., "Analysis of Oil-Film Pressure Distribution in Porous Journal Bearings Under Hydrodynamic Lubrication Conditions Using an Improved Boundary Condition," *Journal of Tribology*, vol. 119, p. 171, Jan. 1997.
- [30] H. C. Brinkman, "A calculation of the viscous force exerted by a flowing fluid on a dense swarm of particles," *Applied Scientific Research*, vol. 1, pp. 27–34, Dec. 1949.
- [31] A. Bejan, *Convection Heat Transfer*. Hoboken, NJ, USA: John Wiley & Sons, Inc., Apr. 2013.
- [32] C. Cusano and R. M. Phelan, "Experimental Investigation of Porous Bronze Bearings," *Journal of Lubrication Technology*, vol. 95, p. 173, Apr. 1973.
- [33] M. Mokhtar, M. Rafaat, and G. Shawki, "Experimental Investigations into the Performance of Porous Journal Bearings," tech. rep., Feb. 1984.
- [34] E. Durak, "Experimental investigation of porous bearings under different lubricant and lubricating conditions," *KSME International Journal*, vol. 17, no. 9, pp. 1276–1286, 2003.
- [35] A. A. Elsharkawy and L. H. Guedouar, "Hydrodynamic lubrication of porous journal bearings using a modified Brinkman-extended Darcy model," *Tribology International*, vol. 34, pp. 767–777, Nov. 2001.
- [36] A. Cameron, V. T. Morgan, and A. E. Stainsby, "Critical conditions for hydrodynamic lubrication of porous metal bearings," *Proceedings of the Institution of Mechanical Engineers*, vol. 176, pp. 761–770, June 1962.
- [37] W. T. Rouleau, "Hydrodynamic Lubrication of Narrow Press-Fitted Porous Metal Bearings," *Journal of Basic Engineering*, vol. 85, p. 123, Mar. 1963.
- [38] P. R. K. Murti, "Lubrication of Narrow Porous Bearings With Arbitrary Wall Thickness," *Journal of Lubrication Technology*, vol. 95, p. 511, Oct. 1973.
- [39] M. Kane and B. Bou-Said, "Comparison of Homogenization and Direct Techniques for the Treatment of Roughness in Incompressible Lubrication," *Journal of Tribology*, vol. 126, p. 733, Oct. 2004.

- [40] P. Swales, "A review of cavitation phenomena in engineering situations," *Cavitation and related phenomena in lubrication, Proceedings of the 1st Leeds-Lyon Symposium on Tribology*, pp. 3–9, 1974.
- [41] D. Dowson and C. M. Taylor, "Cavitation in Bearings," *Annual Review of Fluid Mechanics*, vol. 11, pp. 35–65, Nov. 1979.
- [42] M. J. Braun and R. C. Hendricks, "An Experimental Investigation of the Vaporous/Gaseous Cavity Characteristics of an Eccentric Journal Bearing," in *ASLE Transactions*, vol. 27(1), pp. 1–14, Taylor & Francis Group, Mar. 1982.
- [43] D. E. Brewe, J. H. Ball, and M. M. Khonsari, "Current research in cavitating fluid films. Part 1 – Fundamental and experimental observation," in *Proceedings of the Cavitation Symposium, STLE Annual Meeting,, NASA Technical memorandum*, Aug. 1988.
- [44] D. C. Sun and D. E. Brewe, "A High Speed Photography Study of Cavitation in a Dynamically Loaded Journal Bearing," *Journal of Tribology*, vol. 113, p. 287, Apr. 1991.
- [45] L. Gumbel, "Das Problem der Lagerreibung," *Monatsblatter, Berliner Bezirksverein Deutscher Ingenieure*, vol. 5, pp. 97—104 and 109—120, 1914.
- [46] B. Scheichl, I. A. Neacșu, and A. Kluwick, "A novel view on lubricant flow undergoing cavitation in sintered journal bearings," *Tribology International*, vol. 88, pp. 189–208, Aug. 2015.
- [47] H. W. Swift, "THE STABILITY OF LUBRICATING FILMS IN JOURNAL BEARINGS," *Minutes of the Proceedings*, vol. 233, pp. 267–288, Jan. 1932.
- [48] W. Stieber, *Das Schwimmmlager : Hydrodynamische Theorie des Gleitlagers*. Berlin: VDI-Verlag GmbH, 1933.
- [49] L. Floberg, "On journal bearing lubrication considering the tensile strength of the liquid lubricant," *Transactions of the Machine Elements Division, Lund Technical University, Lund, Sweden*, pp. 1–26, 1973.
- [50] D. E. Brewe, J. H. Ball, and M. M. Khonsari, "Current research in cavitating Films. Part 2 – Theoretical modeling and performance," in *Proceedings of the Cavitation Symposium, STLE Annual Meeting,, NASA Technical memorandum*, 1988.
- [51] G. I. Taylor, "Cavitation of a viscous fluid in narrow passages," *Journal of Fluid Mechanics*, vol. 16, pp. 595–619, Mar. 1963.

- [52] L. Floberg, "On hydrodynamic lubrication with special reference to sub-cavity pressures and number of streamers in cavitation regions," *Acta Polytechnica Scandinavica, Mechanical Engineering Series*, vol. 19, 1965.
- [53] L. Floberg, "Sub-cavity pressures and number of oil streamers in cavitation regions with special reference to the infinite journal bearing.," *Acta polytechnica Scandinavica. Mechanical engineering series*, vol. 37, 1968.
- [54] J. C. Coyne and H. G. Elrod, "Conditions for the Rupture of a Lubricating Film. Part I: Theoretical Model," *Journal of Lubrication Technology*, vol. 92, p. 451, July 1970.
- [55] J. C. Coyne and H. G. Elrod, "Conditions for the Rupture of a Lubricating Film—Part II: New Boundary Conditions for Reynolds Equation," *Journal of Lubrication Technology*, vol. 93, p. 156, Jan. 1971.
- [56] J. A. Cole and C. J. Hughes, "Oil flow and film extent in complete journal bearings," *Proceedings of the Institution of Mechanical Engineers*, vol. 170, pp. 499–510, June 1956.
- [57] H. Elrod and M. Adams, "A computer program for cavitation and starvation problems," *Cavitation and related phenomena in lubrication, Proceedings of the 1st Leeds–Lyon Symposium on Tribology, University of Leeds, Leeds, UK*, 1974.
- [58] B. Jakobsson and L. Floberg, "The finite journal bearing considering vaporization," vol. 190, Jan. 1957.
- [59] B. O. Jacobson and B. J. Hamrock, "Vapor Cavitation in Dynamically Loaded Journal Bearings," *NASA TN-83366*, 1983.
- [60] M. Fesanghary and M. M. Khonsari, "A Modification of the Switch Function in the Elrod Cavitation Algorithm," *Journal of Tribology*, vol. 133, p. 024501, Apr. 2011.
- [61] M. J. Braun, "Cavitation formation and modelling for fluid film bearings: a review," *Proc. Institution of Mechanical Engineers, Part J: Journal of Engineering Tribology*, vol. 224, no. 9, pp. 839–863, 2010.
- [62] G. E. Bart, J.C.J., Cavallaro S., *Biolubricants: Science and Technology*. Woodhead Publishing, 2013.
- [63] N. Doerr, E. Kenesey, C. Oetsch, A. Ecker, A. Pauschitz, and F. Franek, *Evaluation of Ionic Liquids for the Application as Lubricants*, vol. 48 of *Tribology and Interface Engineering Series*. Elsevier, 2005.

- [64] I. Minami, "Ionic liquids in tribology.," *Molecules (Basel, Switzerland)*, vol. 14, pp. 2286–2305, Jan. 2009.
- [65] D. H. Zaitsau, G. J. Kabo, A. A. Strechan, Y. U. Paulechka, A. Tschersich, S. P. Verevkin, and A. Heintz, "Experimental vapor pressures of 1-alkyl-3-methylimidazolium bis(trifluoromethylsulfonyl)imides and a correlation scheme for estimation of vaporization enthalpies of ionic liquids.," *The journal of physical chemistry. A*, vol. 110, pp. 7303–6, June 2006.
- [66] D. A. Nield, "The Beavers–Joseph Boundary Condition and Related Matters: A Historical and Critical Note," *Transport in Porous Media*, vol. 78, pp. 537–540, Feb. 2009.
- [67] E. Buckingham, "On Physically Similar Systems; Illustrations of the Use of Dimensional Equations," *Physical Review*, vol. 4, pp. 345–376, Oct. 1914.
- [68] M. P. Kirkpatrick, S., Gelatt, C. D., Vecchi, "Optimization by Simulated Annealing on JSTOR," *Science*, vol. 220, no. 4598, pp. 671–680, 1983.
- [69] C. Cusano, "The effect of variable permeability on the performance characteristics of porous bearing," *Wear*, vol. 23, pp. 55–62, Jan. 1973.
- [70] V. T. Morgan, "The effect of porosity on some of the physical properties of powder metallurgy components," *Powder metallurgy*, no. 12, p. 72, 1963.
- [71] V. D'Agostino and A. Senatore, "Analytical solution for two-dimensional Reynolds equation for porous journal bearings," *Industrial Lubrication and Tribology*, vol. 58, no. 2, pp. 110–117, 2006.
- [72] P. J. Blau, "On the nature of running-in," *Tribology International*, vol. 38, pp. 1007–1012, 2005.
- [73] S. Krenn, *Charakterisierung von Sintergleitlagern auf Basis der Luftpermeabilität*. Ms thesis, Fachhochschule Wiener Neustadt, 2009.
- [74] K. Pearson, "Notes on regression and inheritance in the case of two parents," *Proceedings of the Royal Society of London*, vol. 58, pp. 240–242, 1895.

Curriculum Vitae

Ioana-Adina Neacșu

BORN : 27.11.1985, Bucharest, Romania
ADDRESS : Scheugasse 6/13+14, 1100 Vienna, Austria
PHONE : +4369915061481
E-MAIL : adina.neacsu@gmail.com

Education

2009 Universidade do Porto
 Erasmus Exchange Program (1 semester)
2004–2009 University Politehnica of Bucharest, Faculty of Engineering Taught in Foreign Languages
 M.Sc. degree in Mechanical Engineering. Thesis title:
 ”Design of a lifting device mechanism for people with locomotive disabilities
 to be used on a campus bus”

Work Experience

SEPT. 2012 TO PRESENT Austrian Competence Center for Tribology- AC2T research GmbH
 Junior Scientist, Simulation Pool
MAY. 2010 - AUG. 2012 Marie Curie Project *MINILUBES*
 Early Stage Researcher

Languages

Romanian: Mother-tongue
English: Fluent
German: Intermediate
Spanish: Intermediate